THE UNIVERSITY OF QUEENSLAND

AUSTRALIA

Hydrodynamic forces in optical tweezers

Lachlan Gibson

B.Sc. (Hons), B.A.

A thesis submitted for the degree of Doctor of Philosophy at

The University of Queensland in 2019

School of Mathematics and Physics

Abstract

Optical tweezers uses light to control and trap microscopic entities including spherical particles, cells or even three dimensionally (3D) printed structures. In most cases the trapped microscopic object is surrounded by a fluid, such as water, and the effects of hydrodynamic forces are significant. This dissertation investigates three aspects of these hydrodynamic forces relevant to optical tweezers systems.

The first aspect is about how hydrodynamic forces in optical tweezers could be used to measure the medium's viscosity and elasticity (viscoelasticity). Previous methods of measuring viscoelasticity using optical tweezers have been limited by their several-minute measurement duration, making them unreliable in biological systems that are slowly changing. To solve this problem new theory and analysis is introduced, experimentally verified by Shu Zhang *et al.* [1, 2] , that enables optical tweezers to perform highly localised measurements of viscoelasticity in sub-minute times.

The second part of the project investigates the hydrodynamic interactions between trapped particles and nearby boundaries. Both numerical and analytical techniques, including novel solutions to the Stokes equations, are presented and used to model the fluid dynamics. The effects of spherical and cylindrical boundaries on an internal sphere are quantified theoretically and compared to experimentally measured (by Shu Zhang *et al.* [3, 4]) wall effects of a 3D printed cylinder based on 2 photon photopolymerisation and round artificial liposomes on the rotation of an optically trapped sphere. An artificial feed-forward neural network is also trained to efficiently reproduce some of these results.

The third part of the project relates to hydrodynamic forces acting on non-spherical star-shaped particles. Calculating drag tensors describing this geometry using existing methods is relatively slow ($\sim 10^0$s). Using these slower numerical methods, the drag tensors of many randomly generated particles are computed and then train an artificial feed-forward neural network to improve the speed ($\sim 10^{-4}$s) at which these drag tensors could be evaluated, making them practical for simulations or real time calculations.

By improving existing techniques and quantifying these kinds of hydrodynamic forces, this work allows optical tweezers to be better applied in microfluidic or biological systems, such as inside a cell, and allows more accurate or more efficient optical tweezers simulations.

Declaration by author

This thesis is composed of my original work, and contains no material previously published or written by another person except where due reference has been made in the text. I have clearly stated the contribution by others to jointly-authored works that I have included in my thesis.

I have clearly stated the contribution of others to my thesis as a whole, including statistical assistance, survey design, data analysis, significant technical procedures, professional editorial advice, financial support and any other original research work used or reported in my thesis. The content of my thesis is the result of work I have carried out since the commencement of my higher degree by research candidature and does not include a substantial part of work that has been submitted to qualify for the award of any other degree or diploma in any university or other tertiary institution. I have clearly stated which parts of my thesis, if any, have been submitted to qualify for another award.

I acknowledge that an electronic copy of my thesis must be lodged with the University Library and, subject to the policy and procedures of The University of Queensland, the thesis be made available for research and study in accordance with the Copyright Act 1968 unless a period of embargo has been approved by the Dean of the Graduate School.

I acknowledge that copyright of all material contained in my thesis resides with the copyright holder(s) of that material. Where appropriate I have obtained copyright permission from the copyright holder to reproduce material in this thesis and have sought permission from co-authors for any jointly authored works included in the thesis.

Publications included in this thesis

1. [1] **L. J. Gibson**, S. Zhang, A. B. Stilgoe, T. A. Nieminen, and H. Rubinsztein-Dunlop. Active rotational and translational microrheology beyond the linear spring regime. *Physical Review E*, 95:042608, April 2017.

2. [3] S. Zhang, **L. J. Gibson**, A. B. Stilgoe, T. A. Nieminen, and H. Rubinsztein-Dunlop. Impact of complex surfaces on biomicrorheological measurements using optical tweezers. *Lab on a Chip*, 18:315–322, January 2018.

3. [5] **L. J. Gibson**, S. Zhang, A. B. Stilgoe, T. A. Nieminen, and H. Rubinsztein-Dunlop. Machine learning wall effects of eccentric spheres for convenient computation. *Physical Review E*, 99:043304, April 2019.

Other publications during candidature

Peer-reviewed articles

1. [2] S. Zhang, **L. J. Gibson**, A. B. Stilgoe, I. A. Favre-Bulle, T. A. Nieminen, and H. Rubinsztein-Dunlop. Ultrasensitive rotating photonic probes for complex biological systems. *Optica*, 4(9):1103–1108, September 2017.

2. [6] A. A. Bui, A. B. Stilgoe, I. C. Lenton, **L. J. Gibson**, A. V. Kashchuk, S. Zhang, and H. Rubinsztein-Dunlop. Theory and practice of simulation of optical tweezers. *Journal of Quantitative Spectroscopy and Radiative Transfer*, 195:66–75, July 2017.

3. [4] S. Zhang, **L. J. Gibson**, A. B. Stilgoe, T. A. Nieminen, and H. Rubinsztein-Dunlop. Measuring local properties inside a cell-mimicking structure using rotating optical tweezers. *Journal of Biophotonics*, 12(7)e201900022, February 2019.

News articles

1. [7] I. A. Favre-Bulle, S. Zhang, A. V. Kashchuk, I. C. D. Lenton, **L. J. Gibson**, A. B. Stilgoe, T. A. Nieminen, and H. Rubinsztein-Dunlop. Optical tweezers bring micromachines to biology. *Optics & Photonics News*, 29(4):40–47, April 2018.

Contributions by others to the thesis

My supervisors Dr. Timo A. Nieminen, Prof. Halina Rubinsztein-Dunlop, and Dr. Alexander B. Stilgoe made significant contributions to the conception and design of the project. Dr. Shu Zhang contributed a strong majority of the experimental work including conducting the measurements presented in chapters 3, 4, and 5. She also made significant contributions to the written work of chapter 5, as well as to interpretation of results. Nieminen, Rubinsztein-Dunlop, Stilgoe and Zhang all contributed to the revision of written material. Nieminen provided technical theoretical support for both analytical and numerical calculations.

Statement of parts of the thesis submitted to qualify for the award of another degree

No works submitted towards another degree have been included in this thesis.

Research involving human or animal subjects

No animal or human subjects were involved in this research.

Acknowledgments

I would like to thank these people for their knowledge, guidance and support shared freely with me throughout the duration of my candidature:

- Timo Nieminen, Halina Rubinsztein-Dunlop, and Alexander Stilgoe for their supervision, ideas, continual encouragement and constructive feedback on my work
- Shu Zhang for collaborating with me as an experimenter
- Isaac Lenton, Itia Favre-Bulle, Anatolii Kashchuk, Declan Armstrong, and all the other people who were members of the Optical Micro-manipulation group during my candidature for being great team workers, attending conferences with me, and providing useful discussions
- Rory Kelly, Jace Cruddas, David Cavanagh, Haroon Aman, Oliver Bellwood and Gian Carlo Ruzzi Villacres for being excellent office buddies and useful (and not-so-useful) stimulating discussions
- James Bennett for developing this dissertation template
- and my family, particularly my wonderful parents, for believing in me and providing emotional support.

Financial support

This research was supported by an Australian Government Research Training Program Scholarship and by the Australian Research Council's Discovery Projects funding scheme (project numbers DP140100753 & DP180101002).

Keywords

optical tweezers, stokes flow, microrheology, hydrodynamics, wall effects, machine learning, drag tensor, viscoelasticity

Australian and New Zealand Standard Research Classifications (ANZSRC)

ANZSRC code: 020303, Fluid Physics, 50%
ANZSRC code: 020501, Classical and Physical Optics, 30%
ANZSRC code: 080205, Numerical Computation, 20%

Fields of Research (FoR) Classification

FoR code: 0203, Classical Physics, 40%
FoR code: 0205, Optical Physics, 30%
FoR code: 0802, Computation Theory and Mathematics, 30%

Contents

Abstract ii

Contents **viii**

List of figures **xi**

List of tables **xiii**

List of abbreviations and symbols **xiv**

1 Introduction to Optical Tweezers Hydrodynamics **1**

1.1 Optical Tweezers 1

1.1.1 How they Work 2

1.1.2 Microrheology 4

1.2 Hydrodynamic Forces 6

1.2.1 Micro-Scale Fluid Dynamics 7

1.2.2 Wall Effects 10

2 General Series Solutions to the Stokes Equations **15**

2.1 Homogeneous Equations 15

2.1.1 Helmholtz Decomposition 15

2.1.2 Solving the Laplace Equation by Separation of Variables 17

2.2 Particular Solutions 18

2.2.1 Particular Solution Equations 19

2.2.2 Finding f and $\mathbf{q}$ 20

2.3 Cartesian, Cylindrical and Spherical Expressions 21

2.3.1 Cartesian Coordinates 21

2.3.2 Cylindrical Coordinates 22

2.3.3 Spherical Coordinates 22

2.4 Force and Torque 23

2.4.1 Spherical coordinates 23

2.4.2 Concentric Spheres 24

2.5 Point Matching . . . 26
2.5.1 Uniform Point Cloud . . . 26

3 Optical Tweezers Microrheology 31
3.1 Introduction . . . 31
3.2 Theory . . . 33
3.2.1 Equation of Motion . . . 33
3.2.2 Linear Case . . . 34
3.2.3 Non-linear Case . . . 36
3.3 Error Analysis . . . 39
3.3.1 Linear Case . . . 39
3.3.2 Non-linear Case . . . 41
3.4 Experimental Results . . . 41
3.4.1 Verification of analysis methodology . . . 42
3.4.2 Measurements of tear film . . . 44
3.5 Conclusion . . . 45

4 Wall Effects of Eccentric Spheres 47
4.1 Introduction . . . 47
4.2 Theory . . . 48
4.2.1 Problem Construction . . . 48
4.2.2 Axisymmetric Rotational Wall Effect . . . 52
4.2.3 Axisymmetric Translational Wall Effect . . . 55
4.2.4 Asymmetric Rotational Wall Effect . . . 58
4.2.5 Asymmetric Translational Wall Effect . . . 61
4.3 Machine Learning . . . 62
4.3.1 Multilayer Perceptron . . . 62
4.3.2 Model . . . 62
4.3.3 Data Evaluation and Network Training . . . 64
4.3.4 Model Error . . . 65
4.4 Comparison With Experiment . . . 67
4.5 Conclusion . . . 69

5 Wall Effects of Cylinders 71
5.1 Introduction . . . 71
5.2 Material and Methods . . . 72
5.2.1 3D-Printed Wall Design . . . 72
5.2.2 Measurement of Wall Effect . . . 72
5.3 Modelling . . . 74
5.3.1 Infinite Cylinder . . . 74

5.3.2 Finite Cylinder . . . 76
5.4 Results . . . 78
5.5 Conclusions . . . 79

6 Machine Learning Drag Tensors of Non-Spherical Shapes 81
6.1 Generating Shapes . . . 82
6.1.1 Spherical Harmonics . . . 82
6.1.2 Generating Coefficients . . . 82
6.2 Evaluation of Drag Tensors . . . 83
6.2.1 Applying the Point Matching Method . . . 83
6.2.2 Quantifying Point Matching Error . . . 84
6.2.3 Training an Intermediate Network to Choose Series Order . . . 84
6.3 Training and Evaluation of Neural Network . . . 86
6.3.1 Network Structure . . . 86
6.3.2 Network Performance . . . 88
6.3.3 Performance on Specific Geometries . . . 89
6.4 Conclusion . . . 91

7 Conclusion 93

Bibliography 95

A Stress Tensors and Stokes Equations 103
A.1 Stress Tensor . . . 103
A.2 Equations of Motion . . . 104

B Tables 105
B.1 Chapter 3 List of Variable Transformations . . . 105
B.2 Chapter 4 Network Biases and Weights . . . 106

List of figures

1.1 Ray optic and electromagnetic wave diagrams of optical tweezers. 3
1.2 The relaxation modulus $G_r(t)$. 5
1.3 The stress tensor σ. 7
1.4 Examples of drag forces and torques. 9
1.5 A comparison between fluid velocity gradients between boundaries. 10
1.6 Rotating concentric spheres. 11
1.7 Wall effects of a plane on a sphere. 14

2.1 The relative error of the total spiral length. 27
2.2 An example of evenly spreading 60 points over a sphere. 28

3.1 The experimental apparatus. 42
3.2 A comparison between analysis methods in water and dilutions of Celluvisc. 43
3.3 The relationship between precision of $G^*(\omega)$ and the number of averaged flips. 44
3.4 Measurenents of complex shear modulii in human tear films. 45

4.1 Eccentric spheres geometry. 49
4.2 The four distinct motions of the inner sphere. 50
4.3 Approximations for the axisymmetric rotational wall effect in the zero clearance limit. . 55
4.4 Limiting behaviour of axisymmetric translational wall effects. 58
4.5 An example of an MLP. 63
4.6 Histograms of the relative error of model outputs. 65
4.7 The ratio of the asymmetric coupling force and the asymmetric translation force. 66
4.8 A Q–Q plot comparing the performance of the model on the testing data when using the network and when using interpolation. The blue lines represent distributions of errors from linear interpolations over 11×10 grids of $\frac{d}{b-a} \times \lambda$. The red lines are corresponding results from cubic interpolations. The network outperforms the interpolation methods in all cases. 67
4.9 The relative error of the model when calculating infinite plane wall effects ($\lambda = 0$). . . . 67
4.10 Experimental measurements of asymmetric rotational wall effects. 68

5.1 Structure of 3D printed finite cylinder. 73
5.2 Experimental apparatus for measuring wall effects. 74
5.3 Wall effects of an infinite cylinder on an axisymmetrically rotating sphere. 77
5.4 Numerical evaluation of wall effects of the finite cylinder when the sphere is centred. . . 77
5.5 Comparison between numerical and measured axisymmetric rotational wall effects. . . . 78
5.6 Experimental measurements of wall effects of cylindrical walls on rotating eccentric spheres. 79

6.1 Three examples of randomly generated particles. 83
6.2 Intermediate MLP performance. 86
6.3 Comparison between drag tensor error metrics for different point matching series orders. 87
6.4 Histograms of error metrics of the 300 validation shapes. 87
6.5 Network structure. 88
6.6 Histograms of error between the network and point matching of 1000 test shapes. 89
6.7 Comparison between network drag tensors and theoretical values of particular shapes. . . 90
6.8 Relative errors of the network output when calculating the drag tensor of a pill shape. . . 91

List of tables

2.1 Values of q_i and f in Cartesian, cylindrical and spherical coordinates. 21

B.1 List of Variable Transformations. 105
B.2 Network biases and weights given to 8 significant figures. 106

List of abbreviations and symbols

Abbreviations	
3D	Three Dimensions
AOM	Acousto-Optic Modulator
CAM	Camera
D	Photodiode Detector
DM	Dichroic Mirror
DNA	Deoxyribonucleic Acid
FDTD	Finite Difference Time Domain
FEM	Finite Element Method
HeNe	Helium-Neon
MLP	Multilayer Perceptron
μm	micrometre
ODE	Ordinary Differential Equation
PBS	Polarising Beam Splitter
PDE	Partial Differential Equation
PM	Point Matching
RMSE	Root Mean Square Error
s	second
SSE	Sum of Squared Errors
UFT	Unilateral Fourier Transform

Chapter 1

Introduction to Optical Tweezers Hydrodynamics

1.1 Optical Tweezers

Optical tweezers use light to manipulate and control very small objects. They have proven to be so useful in many research areas that, Arthur Ashkin, was recently awarded a Nobel Prize in Physics [8] in October 2018 for his work [9–12] introducing and developing this tool. The ability to manipulate and control objects within microscopic systems using light has accelerated the research and opened new avenues of investigation in microbiology [13–23], microfluidics [24–27], microrheology [1, 2, 28–40] and many more fields. Optical tweezers usually work better in systems containing fluids because they add buoyancy and mitigate effects of reflective and diffusive forces. So understanding fluid dynamics on small scales is essential to explain many phenomena and conduct quantitative measurements. Therefore, this dissertation aims to characterise hydrodynamic forces and interactions in systems which utilise optical tweezers.

Hydrodynamic forces in optical tweezers systems are sometimes the main focus of the experiment, such as when optical tweezers are used to measure fluid properties, and other times they simply need to be well understood so that other factors, such as cellular forces, can be isolated. In most optical tweezers systems, there seem to be three primary factors that influence the hydrodynamic forces: the geometry of the trapped particle, interactions with nearby boundaries, and properties of the fluid medium such as viscosity. In a system where the goal is to observe other forces, like optical forces or cellular forces, the hydrodynamic forces need to be fully understood so that they can be distinguished. In these cases, the effects of all three factors of particle geometry, boundary interactions and fluid properties need to be known. In other cases, some of these factors themselves might be the point of interest of the experiment. In these cases, the effects of two factors need to be understood, so that the third could be measured. For example, in an optical tweezers particle tracking microrheometer, the goal is to measure properties of the medium fluid such as viscosity. In this example, the effects of particle geometry and boundary interactions need to be known so that the effects of the fluid itself can

be isolated and the viscosity can be deduced.

Particles are frequently trapped in systems containing boundaries, complex fluids or with non-spherical objects. This is especially common in the more interesting experiments, like in biological systems. In such cases, it is common practice to assume or approximate the three factors as more ideal than they really are. However, to perform these experiments rigorously, it is critical to characterise the hydrodynamic forces more accurately. Therefore, this project examines sub-problems in each of the three factors relating to particle geometry, boundary interactions and fluid properties. This includes how viscosity and elasticity of fluids can be measured via optical tweezers (chapter 3), how boundaries affect the dynamics of trapped spheres (chapters 4 and 5) and calculations of how viscous forces and torques depend on the translational and rotational motion of different probe particles (chapter 6).

1.1.1 How they Work

The mechanical effects of light are rarely considered in daily life because the optical forces and torques acting on macroscopic objects are imperceptible. However, optical tweezers manage to utilise light's linear or angular momentum or both to trap and manipulate microscopic objects. The intensity near the focal point of a highly focused laser beam can be strong enough to exert appreciable forces and torques on objects such as cells, DNA or other tiny particles. This allows light to become a tool that can mechanically manipulate or power objects in microscopic systems.

Trapping Optical Tweezers

One of the primary functions of optical tweezers is the ability to trap and hold particles in three dimensions (3D) using a highly focussed laser beam. This works primarily through refraction whereby a trapped particle deflects light *away* from the focal point, thereby experiencing an optical force *towards* the focal point. This phenomenon can be qualitatively explained by both ray and wave optics, although accurate quantitative descriptions of forces on objects sized similar to the light wavelength require the latter. Lenton *et al.* [41] in their paper titled *Visual guide to optical tweezers* have produced insightful ray optics and electromagnetic wave diagrams (figure 1.1). By simulating a focused propagating Gaussian beam, they illustrate how the deflection of the light and radial forces acting on a trapped sphere depend on the position within the beam. Figure 1.1 clearly shows how light is refracted away from the focal point and that the force is grater when this deflection is greater.

Rotational Optical Tweezers

Some particles trapped or moved in 3D by exchanging linear momentum with the light can also, analogously, be angularly trapped or rotated by the exchange of angular momentum between the particle and the trapping light. Birefringent particles can achieve this by acting like waveplates and changing the polarisation, and hence spin angular momentum of the trapping laser [42]. Therefore, trapping a birefringent particle with a linearly polarised beam would apply a torque pushing its optic axis to align with the incident polarisation angle. Trapping with a circularly polarised beam could

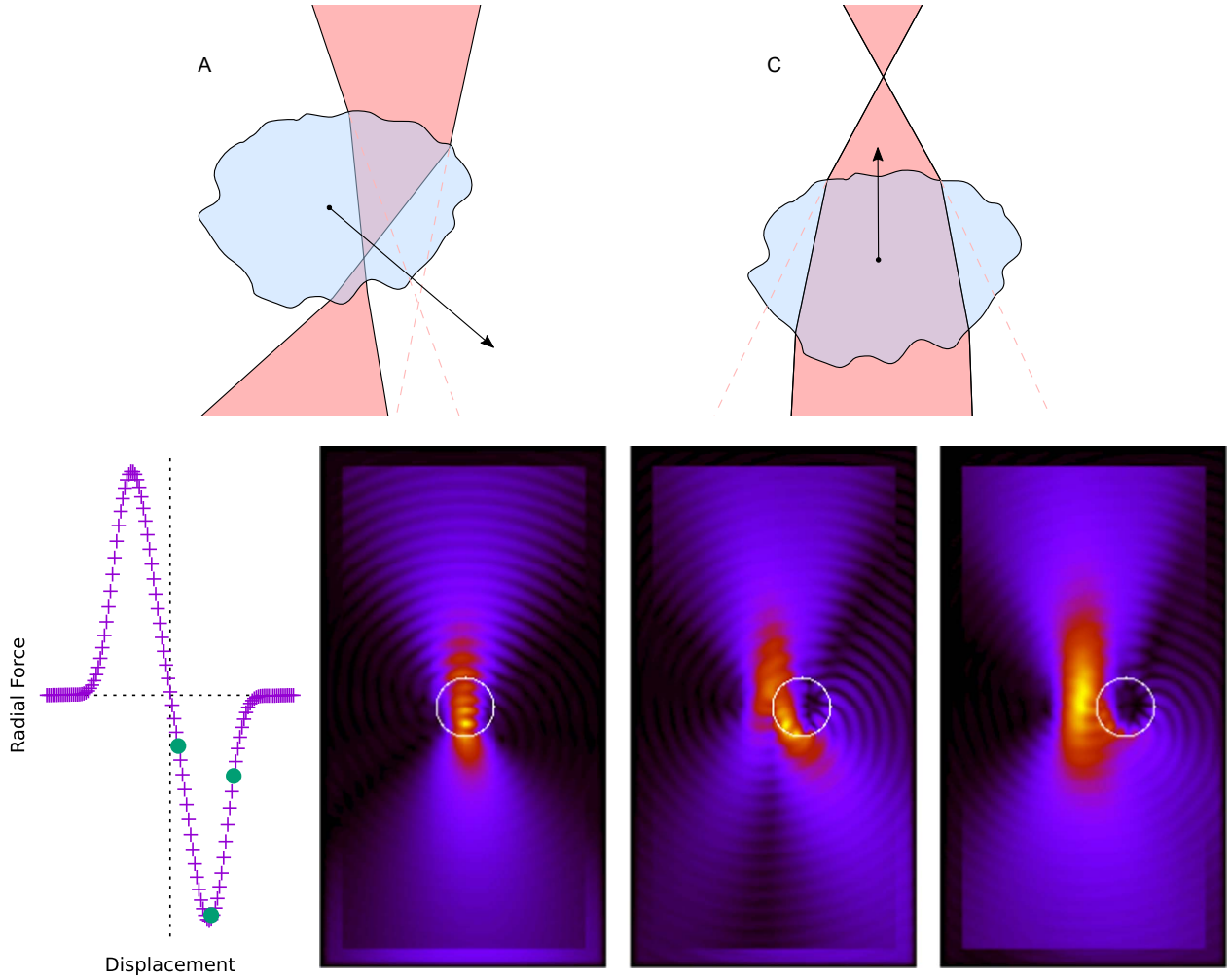

Figure 1.1: Ray optic and electromagnetic wave diagrams of optical tweezers. Averaging accross the whole beam, generic particles often behave approximately as smooth objects. When the refractive index of the particle is greater than that of the surounding medium then the rays are refracted towards the centre of the particle on average, generating an opposing force towards the trap focal point (top). Simulations (bottom) of a propagating Gaussian beam interacting with a dialectric particle using a finite difference time domain (FDTD) method can allow the relationship between position and force to be quantified. Figure by Lenton *et al.* [41]

alternatively apply a continuous torque to the particle, while an elliptically polarised beam could apply the effects of both beams. It is also possible to apply torques through orbital angular momentum such as by using vortex beams [43, 44] or multiple beams [45, 46]. A benefit of using spin angular momentum to rotate, however, is that the optical torque and particle angular velocity can be measured quickly and accurately through the measurement of change in the polarisation of the outgoing beam [40, 47, 48].

Biological Applications

The ability of optical tweezers to exert and measure minute forces and torques enables it to be a powerful tool for studying biological systems including sorting cells [25], investigating chromosome movement on mitotic spindles [49], trapping and manipulating cells [12], stretching cells in microfluidics [50], measuring viscoelasticity with a trapped probe particle [38, 40], performing intracellular

measurements of viscoelasticity [19–22] and much more. Although biological applications do not comprise all applications of optical tweezers, they do demonstrate how quantifying hydrodynamic forces is important, given the presence of fluids in almost every example.

1.1.2 Microrheology

The presence of hydrodynamic forces in optical tweezers systems actually enables one of their primary applications, microrheology. Rheology is the study of deformation and flow of materials [51]. Therefore, optical tweezers can serve as a rheometer by exploiting the interaction between optically trapped microscopic particles and the surrounding medium to quantify local properties of the fluid. A device that performs these measurements on the microscopic scale is called a microrheometer. More specifically, the goal of a microrheometer is to quantify the relationship between stress (σ) and strain (γ) in the material: the so called rheological equation of state.

Viscoelasticity

Two ideal rheological equations of state are those for viscous fluids and elastic solids. The viscous fluid relates the shear stress linearly to the *rate* of shear strain ($\dot{\gamma}$) via a constant of proportionality called the viscosity (η),

$$\sigma = \eta \dot{\gamma}. \tag{1.1}$$

In viscous fluids, stress only exists while the material deformation is changing. This stress acts like friction, dissipating the energy. On the other hand, the elastic solid relates the shear stress linearly to the shear strain directly via a constant of proportionality called the shear modulus (G),

$$\sigma = G\gamma. \tag{1.2}$$

Elastic solids store energy when strained and the material will experience forces countering any deformations.

Despite their simplicity, these rheological equations of state are surprisingly accurate in modelling many materials, such as water and ethanol. More generally, many materials exhibit both viscous and elastic properties. Consider a so-called viscoelastic fluid experiencing a sudden change in strain, such as a unit step. A time-dependent stress results from the strain which, after some time, decays to zero in a fluid. The resulting time dependent stress from a unit step in strain is called the relaxation modulus $G_r(t)$ and an example is plotted in figure 1.2. If the material is linear[1] then $G_r(t)$ fully characterises the rheological equation of state via a convolution with the rate of shear strain,

$$\sigma(t) = \int_{-\infty}^{t} G_r(t-t')\dot{\gamma}(t')\,dt' = \int_{0}^{\infty} G_r(t')\dot{\gamma}(t-t')\,dt'. \tag{1.3}$$

Conceptually, the changing stress is treated like a series of small steps over time, and so the resulting strain is the summation (integral) of the corresponding relaxation moduli responses to each successive

[1] A linear material here is one in which stresses resulting from a linear combination of strains can be calculated by the same linear combination of corresponding stresses. $\gamma_1 \to \sigma_1$ and $\gamma_2 \to \sigma_2$ implies that $(a\gamma_1 + b\gamma_2) \to (a\sigma_1 + b\sigma_2)$

step. In the cases of viscous fluids and elastic solids, the relaxation modulus is given by $G_r(t) = \eta\delta(t)$ and $G_r(t) = G$ respectively, where $\delta(t)$ is the Dirac delta function.

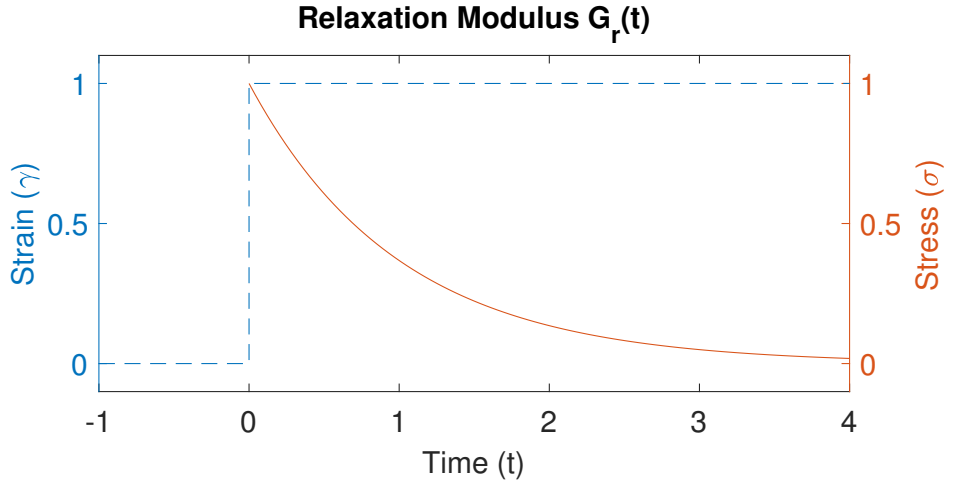

Figure 1.2: The relaxation modulus $G_r(t)$ is the stress response (solid orange) to a unit step strain (dashed blue) in a linear viscoelastic material. In this example it is a decaying exponential $G_r(t) = e^{-t}$.

The Complex Shear Modulus

It is often expedient to represent dynamics and viscoelasticity in the frequency domain. From equation (1.3) it is possible to show that a sinusoidal strain $\gamma(t) = \gamma(0)e^{i\omega t}$ results in a sinusoidal stress,

$$\sigma(t) = \int_0^\infty G_r(t')i\omega\gamma(0)e^{i\omega(t-t')}\,dt', \tag{1.4}$$

$$\sigma(t) = i\omega\gamma(0)e^{i\omega t}\int_0^\infty G_r(t')e^{-i\omega t'}\,dt' \tag{1.5}$$

$$\sigma(t) = \gamma(t)G^*(\omega), \tag{1.6}$$

where the ratio of the stress and strain complex sinusoids is called the *complex shear modulus* defined by

$$G^*(\omega) = i\omega\int_0^\infty G_r(t')e^{-i\omega t'}\,dt'. \tag{1.7}$$

More generally, the complex shear modulus represents the relationship between corresponding components of the stress ($\hat{\sigma}(\omega)$) and strain ($\hat{\gamma}(\omega)$) in the frequency domain. Consider stress and strain represented by

$$\sigma(t) = \int_{-\infty}^\infty \hat{\sigma}(\omega)e^{i\omega t}\,d\omega, \qquad \gamma(t) = \int_{-\infty}^\infty \hat{\gamma}(\omega)e^{i\omega t}\,d\omega. \tag{1.8}$$

Based on the definition of $G^*(\omega)$ and equation (1.3) it is possible to show that

$$G^*(\omega) = \frac{\hat{\sigma}(\omega)}{\hat{\gamma}(\omega)}. \tag{1.9}$$

One of the strengths of this representation of viscoelasticity is that it allows the viscous and elastic components at different time scales to be clearly distinguished. Considering that elastic stress should be in phase with the strain while viscous stress should be $\pi/2$ out of phase with the strain (that is in

phase with the *rate* of strain), then the real part of $G^*(\omega)$, called the storage modulus (G'), represents the elastic component, while the imaginary part, called the loss modulus (G''), represents the viscous component,

$$G^*(\omega) = G'(\omega) + iG''(\omega). \tag{1.10}$$

It is not too surprising then, that the complex shear modulus of elastic solids and viscous fluids are given by $G^*(\omega) = G$ and $G^*(\omega) = i\omega\eta$, respectively.

Particle Tracking Microrheology

Optical tweezers can be used to measure viscoelasticity through particle tracking microrheology. Particle tracking involves observing the motion of particles suspended in the medium being measured. The dynamics of these embedded particles are influenced by the medium's viscoelasticity, therefore allowing it to be deduced from their motion. In the case of optical tweezers particle tracking microrheology, the trapped particle's translational or rotational motion is tracked. In passive microrheology, where the Brownian motion is the primary driving force, statistical methods such as autocorrelation functions are usually used to, and excel at, extracting high frequency viscoelasticity. When the particle is driven by optical forces the motion is much slower than the Brownian motion which becomes a source of noise rather than signal. Therefore, these so called active methods can be combined with passive methods to more accurately obtain measurements over the full frequency spectrum. [2, 38]

One of the key strengths of optical tweezers microrheology over conventional macrorheology is the ability to make localised measurements of viscoelasticity. This becomes especially useful when the available sample volume is tiny, one wishes to measure inhomogenenieties, or the pertinent fluid is contained within a microscopic structure. An example of the latter would be performing measurements inside a living cell. Although attempts have been made already [15, 18–22], performing accurate and reliable measurements within a cell remains a challenge. Tassieri [52] points out one of the biggest problems, that the time scale of the measurement required to constrain thermal noise is longer than the time scales of many biological processes inside the cell. Therefore, one of the goals of this thesis is to optimise the methodology of optical tweezers microrheology to make it a viable option. This is explored further in chapter 3.

1.2 Hydrodynamic Forces

As previously mentioned, many optical tweezers systems manipulate micron or nanometre sized objects, suspended or surrounded by fluids. Therefore, it is important to be able to understand the hydrodynamic forces acting on these objects and the nature of hydrodynamic interactions between them and other objects and boundaries. Typically the drag forces in these optical tweezers measurements are modelled using either simplified geometries or crude models, often without adequate justification.

For example, Jünger *et al.* [53] used an exponential function to model the viscous drag on a sphere as it approached a cell membrane. Their experimental approach was validated via their viscous drag

measurements as the probe particle approached a plane (the glass slide) which agreed with known theoretical values (which are not exponential). However, the plane wall theory inadequately modelled the viscous drag induced by the cellular membrane which necessitated the use of the exponential model.

Another example involves the work of Mas *et al.* [22] who performed intracellular viscoelastic measurements by observing the dynamics of an optically trapped lipid granule. In this work the particle shape was assumed to be spherical and wall effects were ignored without justification. Provided the geometry of the probe particle and surrounding organelles can be measured, it should be possible to quantify their effects on the measurement more accurately. This is the kind of problem for which this dissertation aims to resolve by making calculations more tailored to the actual geometry of experiments to produce predictions based on theory. This section describes the theory used to model the fluid dynamics and hydrodynamic forces within viscous fluids on the microscopic scale.

1.2.1 Micro-Scale Fluid Dynamics

Stress Tensor and Equations of Motion

It is assumed throughout this dissertation that, even at the microscopic scale, the fluid can be regarded as a continuous medium, that is, a continuum. Therefore, dynamical equations of the fluid can be derived from conservation laws and related to the stress tensor (σ), which describes the state of stress in all directions throughout the material. [54] Figure 1.3 illustrates Cartesian components of the stress tensor.

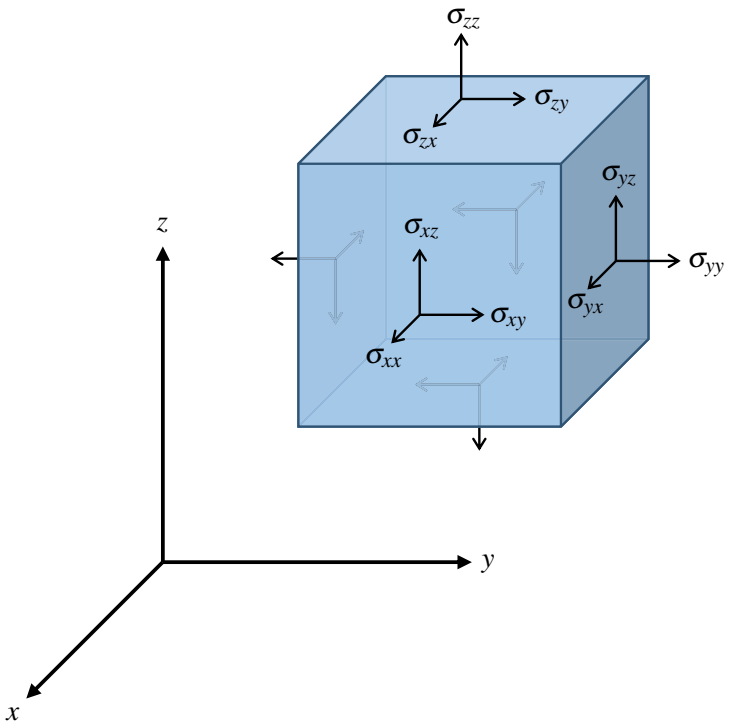

Figure 1.3: The stress tensor σ in Cartesian coordinates describes the stresses in each direction of each face on an infinitesimal cubic volume.

Conservation of mass in an incompressible fluid dictates that the divergence of the fluid velocity $\mathbf{v}$ is zero, $\nabla \cdot \mathbf{v} = 0$. This is known as the continuity equation. Conservation of momentum gives the Cauchy momentum equation which relates the total force acting on an infinitesimal volume element to the sum of external forces $\mathbf{f_{ext}}$ and the fluid's stress tensor σ,

$$\rho \frac{D\mathbf{v}}{Dt} = \mathbf{f_{ext}} + \nabla \cdot \sigma \tag{1.11}$$

where ρ is the fluid density and $\frac{D\mathbf{v}}{Dt}$ is the material derivative.[2]

As would be expected in microscopic systems, external forces acting on the fluid are assumed to be negligible. Similarly, in the low Reynolds number limit[3] the inertial terms are neglected. So equation (1.11) is reduced to $\nabla \cdot \sigma = \mathbf{0}$. Modelling the fluid as an isotropic Newtonian incompressible viscous fluid results in a symmetric stress tensor that depends on the pressure (p) and dynamic viscosity (η),

$$\sigma = -p\mathbf{I} + \eta \left(\nabla \mathbf{v} + \nabla \mathbf{v}^T \right), \tag{1.12}$$

where $\mathbf{I}$ is the identity tensor and the T superscript denotes transposition. Setting the divergences of this stress tensor and the fluid velocity to zero results in the Stokes equations,

$$\eta \nabla^2 \mathbf{v} = \nabla p, \qquad \nabla \cdot \mathbf{v} = 0. \tag{1.13}$$

Throughout this dissertation, stick (no-slip) boundary conditions are assumed whereby the velocity of the fluid at the particle and any other boundary surface matches the velocity of the corresponding surface. The Stokes equations, together with stick boundary conditions fully model the fluid dynamics. Equations for the stress tensor and Stokes equations in Cartesian, cylindrical and spherical coordinates are included in Appendix A.

Force and Torque on a Surface

Once the velocity and pressure fields are known, calculating the total drag force and torque acting on a particle or surface involves evaluating the force and torque acting on surface elements and then integrating over the whole surface. The stress ($\mathbf{P}$) acting on a surface element of the particle is the negative[4] dot product of the unit normal vector ($\hat{n}$) of the *fluid* surface and the stress tensor,

$$\mathbf{P} = -\hat{n} \cdot \sigma. \tag{1.14}$$

Therefore, the surface torque density ($\mathbf{T}$) acting on the particle is

$$\mathbf{T} = \mathbf{r} \times \mathbf{P}, \tag{1.15}$$

where $\mathbf{r}$ is the position vector at the surface. Evaluating the total force ($\mathbf{F}$) and torque ($\mathbf{G}$) acting on the particle involves integrating the force and torque densities over the whole surface (S),

$$\mathbf{F} = \iint_S \mathbf{P}\, dS, \qquad \mathbf{G} = \iint_S \mathbf{T}\, dS. \tag{1.16}$$

[2] The material derivative, also called by other names such as the advective derivative, is defined by $\frac{D}{Dt} = \frac{\partial}{\partial t} + \mathbf{v} \cdot \nabla$.

[3] A 10μm sized particle moving at 100μm/s in water would induce flows with Reynolds numbers of about 10^{-3}. Reynolds numbers for smaller particles at slower speeds would be even smaller.

[4] The stress on the surface of the particle acts in the opposite direction to the stress acting on the surface of the fluid.

Drag Tensor

As illustrated in figure 1.4, a particle moving in a viscous fluid generally experiences a drag force or torque that opposes its motion. The relationship between geometry, motion and drag experienced by particles in a free fluid undergoing Stokes flow has been thoroughly investigated by Brenner [55–60]. Thanks to the linearity of the Stokes equations, he found that the hydrodynamic forces (**F**) and torques (**G**) acting on a particle can be linearly related to the particles translational (**v**) and angular velocity (**Ω**), viscosity and a drag tensor ($\mathscr{D}$) determined by the particle's geometry,

$$\begin{bmatrix} \mathbf{F} \\ \mathbf{G} \end{bmatrix} = -\eta \mathscr{D} \begin{bmatrix} \mathbf{v} \\ \mathbf{\Omega} \end{bmatrix}, \qquad \text{where } \mathscr{D} = \begin{bmatrix} K & C^T \\ C & O \end{bmatrix}. \tag{1.17}$$

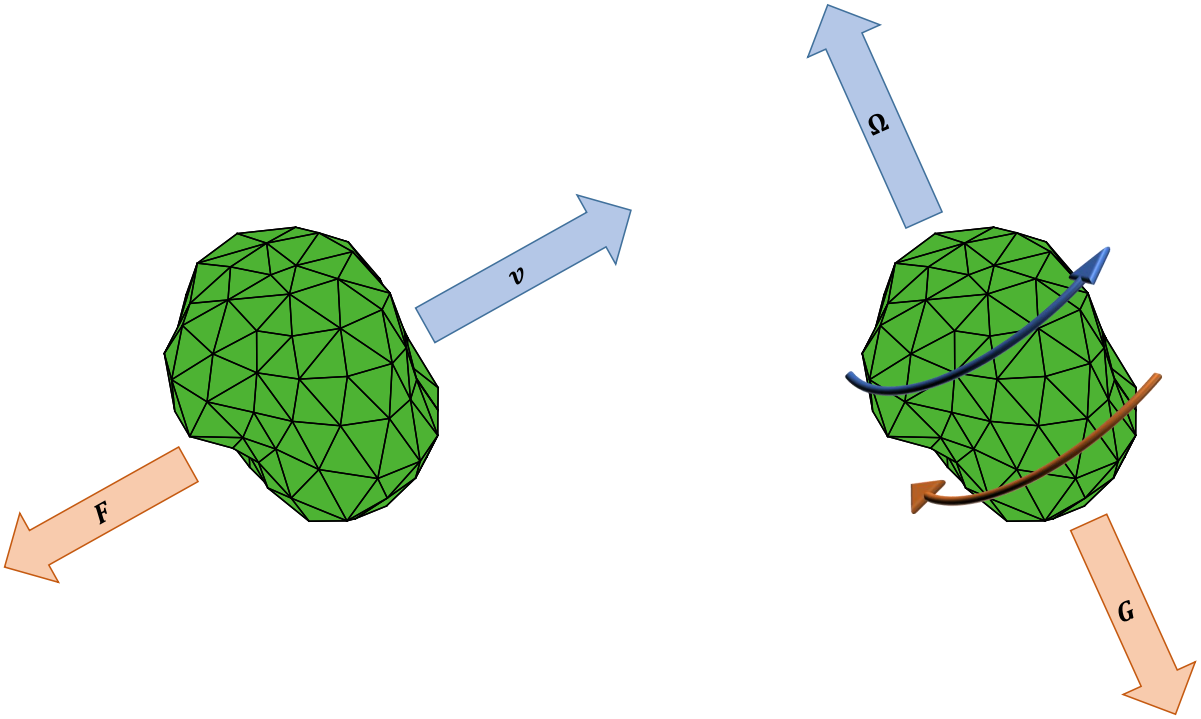

Figure 1.4: Examples of drag forces (left) and torques (right). Generally the dominant components of these drag forces and torques (downward red arrows) acting on round particles (green mesh) oppose the motion (upward blue arrows). However, it is also possible, depending on the geometry, that different directions as well as differnt types of motion are coupled.

The drag tensor is a symmetric[5] 6×6 matrix which can be expressed as the combination of three other 3×3 matrices K, C and O. K and O are the translation and rotation tensors. They are symmetric matrices which relate the translational motion to the translation force and the angular motion to the angular force (torque) respectively. O is the coupling tensor which describes how the translational and rotational motions and forces are coupled, and is not symmetric in general.

The drag tensor is determined entirely by the shape of the particle and the origin of the coordinate system. Happel and Brenner [60] provide the transformation rules of the drag tensor when the origin is

[5]The symmetry of the drag tensor is a consequence of the Lorentz reciprocal theorem, the details of which are outlined by Happel and Brenner. [60]

translated by a vector $\mathbf{r}_{12}$ from point 1 to 2,

$$K_2 = K_1, \qquad C_2 = C_1 - \mathbf{r}_{12} \times K_1, \qquad O_2 = O_1 - \mathbf{r}_{12} \times K_1 \times \mathbf{r}_{12} + C_1 \times \mathbf{r}_{12} - \mathbf{r}_{12} \times C_1^T. \tag{1.18}$$

The columns of the drag tensor of a particle can be evaluated by calculating the force and torque experienced for six independent boundary conditions: translation in x, y and z, and rotation about the x, y and z axes. Each boundary condition corresponds to a row in the $[\mathbf{v}\ \ \boldsymbol{\Omega}]^T$ vector and hence a column of $\mathscr{D}$.

1.2.2 Wall Effects

The dynamics of objects situated near boundaries or other particles are often different than if they were isolated. The effects of boundaries hydrodynamically interacting with optically trapped (or otherwise) objects are called wall effects. The presence of walls (or other particles) change the flow field because of their boundary conditions. Under stick (no-slip) boundary conditions, particles moving near boundaries that are stationary experience larger drag forces for the same motion than when isolated. This is because the flow velocity must reach zero at the boundary, a finite distance away. So between the particle surface and the boundary the flow velocity changes faster than it otherwise would and the viscous drag is larger. As illustrated in figure 1.5, the magnitude of wall effects are typically larger when the distance between boundaries is shorter. Given the ubiquity of boundaries in microscopic optical tweezers systems, it is necessary to have a firm understanding of wall effects and how to quantify them.

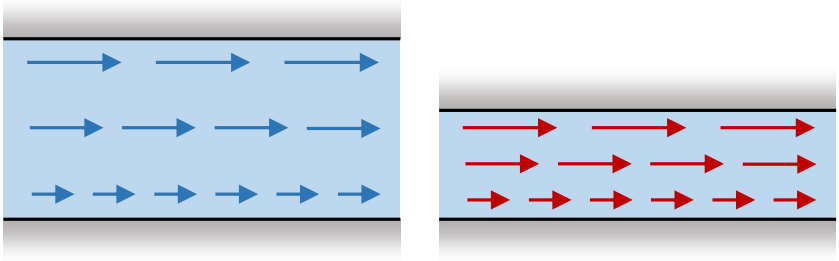

Figure 1.5: A comparison between fluid velocity gradients between boundaries. On the left, the upper boundary moves with a constant velocity while the lower is stationary. The gradient in flow field of the fluid between them generates a viscous drag. On the right the boundaries move at the same speed but the distance between them is less. Therefore, the fluid velocity experiences a steeper gradient and exerts a larger viscous force.

Concentric Spheres

It is worth providing an example of how to calculate flow fields from the equations of motion (1.13) as well as the drag and wall effects of boundaries using the theoretical process previously outlined. A sphere rotating inside another stationary sphere is a well understood problem which can serve as a relatively straightforward example.

Consider a spherical particle of radius a, rotating with angular velocity Ω, inside an outer stationary spherical boundary of radius b. If the spheres are concentric then we can define the origin to be at their centres and the z axis to be parallel to the axis of rotation of the internal sphere. This configuration is illustrated in figure 1.6.

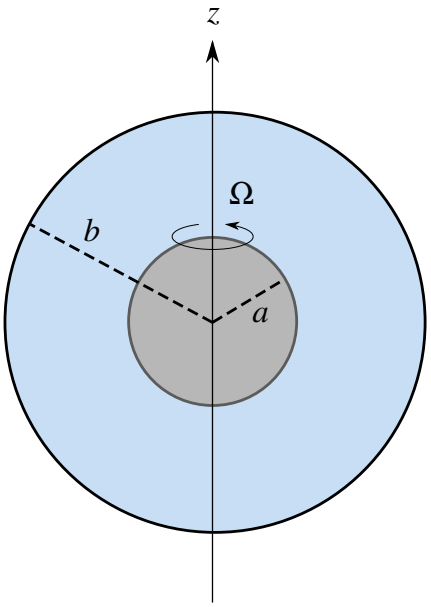

Figure 1.6: Rotating concentric spheres. A spherical particle of radius a, rotating with angular velocity Ω about the z axis, is centred inside an outer stationary spherical boundary of radius b. The fluid (blue) exists between the concentric spherical boundaries. This particular configuration is axisymmetric about the z axis.

If the internal sphere were free to rotate in a free fluid without the presence of the boundary then the fluid would extend to infinity and any fluid motion would decay with the distance from the particle. However, in this case, the presence of the stationary outer sphere with stick boundary conditions requires that the flow field reach zero at a finite distance to the particle. Since the flow at the surface of the rotating particle is the same in each case, it follows that it decays to zero in a shorter distance when the boundary is present. This results in a higher drag force since the shear rates within the fluid are higher. This is the rotational wall effect of concentric spheres.

Quantifying the wall effect requires the Stokes equations of motion (1.13) to be solved for these boundary conditions. This requires a choice of coordinate system to represent the vector components of $\mathbf{v}$, as well as a coordinate system to represent the spatial dependence of those components and pressure. Aligning the axis of symmetry of the problem with the z axis removes any ϕ dependence from the spherical vector components (v_r, v_θ, v_ϕ) of $\mathbf{v}$. Choosing spherical coordinates (r, θ, ϕ) also allows the boundaries to be represented using the coordinate surfaces $r = a$ and $r = b$. Therefore, spherical vector components[6] and spherical coordinates are convenient to use in this particular problem.

[6] Actually, both Cartesian and cylindrical vector components work well too, as long as spherical coordinates are used to represent their spatial dependence.

In this case, the stick boundary conditions can be represented by

$$\begin{aligned} &v_r = 0, \quad v_\theta = 0, \quad v_\phi = \Omega a \sin\theta, \quad \text{at } r = a, \\ &v_r = 0, \quad v_\theta = 0, \quad v_\phi = 0, \qquad\quad \text{at } r = b. \end{aligned} \tag{1.19}$$

The Stokes equations of motion in spherical coordinates are provided in Appendix A. Evidently, choosing $v_r = v_\theta = p = 0$ satisfies the axisymmetric Stokes equations[7], continuity equation, as well as the boundary conditions. This leaves just a single partial differential equation (PDE) for v_ϕ,

$$\frac{1}{r^2}\frac{\partial}{\partial r}\left(r^2\frac{\partial v_\phi}{\partial r}\right) + \frac{1}{r^2\sin\theta}\frac{\partial}{\partial\theta}\left(\sin\theta\frac{\partial v_\phi}{\partial\theta}\right) - \frac{v_\phi}{r^2\sin^2\theta} = 0 \tag{1.20}$$

which, through separation of variables[8], has a general series solution,

$$v_\phi = \sum_{n=1}^{\infty} P_n^1(\cos\theta)\left(A_n r^n + B_n r^{-n-1}\right), \tag{1.21}$$

where P_n^1 are the associated Legendre functions of order 1, and A_n and B_n are real numbered constants. These constants can be uniquely determined by the boundary conditions in equation (1.19). The orthogonality of the associated Legendre functions makes them easy to calculate,

$$A_1 = \frac{a^3}{b^3 - a^3}\Omega, \qquad B_1 = -\frac{a^3 b^3}{b^3 - a^3}\Omega, \qquad A_n = B_n = 0, \quad \forall n > 1. \tag{1.22}$$

Therefore, the flow field of rotating concentric spheres ($\mathbf{v}_{cs}$) has been solved and is given by

$$\mathbf{v}_{cs} = \left[0 \quad 0 \quad \Omega\sin\theta\frac{a^3b^3}{b^3-a^3}r\left(\frac{1}{r^3} - \frac{1}{b^3}\right)\right]^T. \tag{1.23}$$

It is worth noting that the sphere rotating in a free fluid is a special case of the concentric spheres problem where the limit of the outer boundary radius is extended to infinity. The flow field in the free case ($\mathbf{v}_{fs}$) is

$$\mathbf{v}_{fs} = \lim_{b\to\infty}\mathbf{v}_{cs} = \left[0 \quad 0 \quad \Omega\sin\theta a^3\frac{1}{r^2}\right]^T. \tag{1.24}$$

Now we wish to calculate the drag torque acting on the sphere. Comparing this drag to the drag experienced in a free fluid gives the wall effect. The position vector at the inner sphere surface is given by

$$\mathbf{r} = \left[a \quad 0 \quad 0\right]^T. \tag{1.25}$$

Therefore, the surface normal vector $\hat{n}$ (inward with respect to the particle but outward with respect to the fluid) is given by

$$\hat{n} = -\frac{\mathbf{r}}{a} = \left[-1 \quad 0 \quad 0\right]^T. \tag{1.26}$$

Therefore the stress ($\mathbf{P}$) and surface torque density ($\mathbf{T}$) acting on a surface element of the sphere is

$$\mathbf{P} = -\hat{n}\cdot\sigma = \left[\sigma_{rr} \quad \sigma_{r\theta} \quad \sigma_{\phi r}\right]^T, \tag{1.27}$$

$$\mathbf{T} = \mathbf{r}\times\mathbf{P} = a\left[0 \quad -\sigma_{\phi r} \quad \sigma_{r\theta}\right]^T. \tag{1.28}$$

[7] Axisymmetry about the z axis means that v_r, v_θ, v_ϕ and p are all independent of ϕ, so all their derivatives with respect to ϕ are zero.

[8] Separation of variables is a method discussed further, in the context of the Laplace equation, in section 2.1.2.

where expressions for the the stress tensor elements in spherical coordinates σ_{rr}, $\sigma_{r\theta}$ and $\sigma_{\phi r}$ can be found in Appendix A. In this case: $\sigma_{rr} = \sigma_{r\theta} = 0$, and

$$\sigma_{\phi r} = \eta \left(\frac{\partial v_\phi}{\partial r} - \frac{v_\phi}{r} \right) = -\eta \Omega \sin\theta \frac{a^3 b^3}{b^3 - a^3} \frac{3}{r^3}. \tag{1.29}$$

Now the total torque can be found by integrating around the whole sphere. At this point it is helpful to express $\mathbf{T}$ in Cartesian vector components since they do not change direction over the surface. The symmetry indicates that only the torque about the z axis (G_z) can be non-zero. So we only need the z component of $\mathbf{T}$ at $r = a$,

$$T_z = a\sigma_{r\phi} \sin\theta = -3\eta\Omega a \sin^2\theta \frac{b^3}{b^3 - a^3}. \tag{1.30}$$

Therefore, the total torque is

$$G_z = \int_0^{2\pi} \int_0^{\pi} T_z a^2 \sin\theta \, d\theta d\phi = -8\pi\eta\Omega a^3 \frac{b^3}{b^3 - a^3}. \tag{1.31}$$

Indicated by the negative sign, this drag torque is in the opposite direction to the sphere's rotation.

Calculating the torque acting on a sphere in a free fluid involves repeating this calculation for $\mathbf{v}_{fs}$ or taking the $b \to \infty$ limit of this final result, both give the same result of $-8\pi\eta\Omega a^3$. Therefore, the wall effect can be quantified by taking the ratio of the torque in the presence of the wall with this free fluid torque,

$$W_{cs} = \frac{G_z}{-8\pi\eta\Omega a^3} = \frac{b^3}{b^3 - a^3} = \frac{(b/a)^3}{1 - (b/a)^3} > 1. \tag{1.32}$$

Interestingly, the rotational wall effect of concentric spheres is independent on the viscosity or angular velocity, depending only on the ratio of the radii of both spheres. This is a consequence of the linearity of the equations of motion and also a common result in Stokes flow.

Sphere and Infinite Plane

Another well understood example is the effects of an infinite plane on the motion of a sphere. In the context of optical tweezers this can occur when trapping a spherical particle near the microscope slide, coverslip or near a flat microfluidic wall. These wall effects can be calculated exactly by solving the Stokes equations in bispherical coordinates [61–63]. The derivation of the exact solutions will not be included here (see chapter 4 for more details) but rather this section will serve as an illustration of how wall effects affect the dynamics of optically trapped particles.

Leach *et al.* [64] in their paper titled *Comparison of Faxén's correction for a microsphere translating or rotating near a surface* explored the wall effects of flat surfaces in a microfluidic device on the translation and rotation of an optically trapped spherical particle. In particular, the magnitudes of rotational wall effects as a function of distance between the particle centre and microfluidic wall (s) were measured by spinning the particle using circularly polarised light. The rotational wall effects are inversely related to the angular velocity of the particle when rotated with the same optical torque. Analogously, the translational wall effects were measured by analysing the changes in linear Brownian motion as a function of distance.

Leach *et al.*'s results, shown in figure 1.7, not only demonstrate that the wall effects are significant and measurable using optical tweezers, but also that the theory, at least in this case, could accurately quantify them. In other cases where the boundaries are deformable, such as a cell membrane [53], or when they are covered in surfactants [65, 66], the wall effects are not necessarily consistent with predictions assuming stationary boundary conditions. Therefore, it is worth quantifying the wall effects of other curved surfaces, and investigating how applicable they are in real optical tweezers systems. This is the goal of chapters 4 and 5.

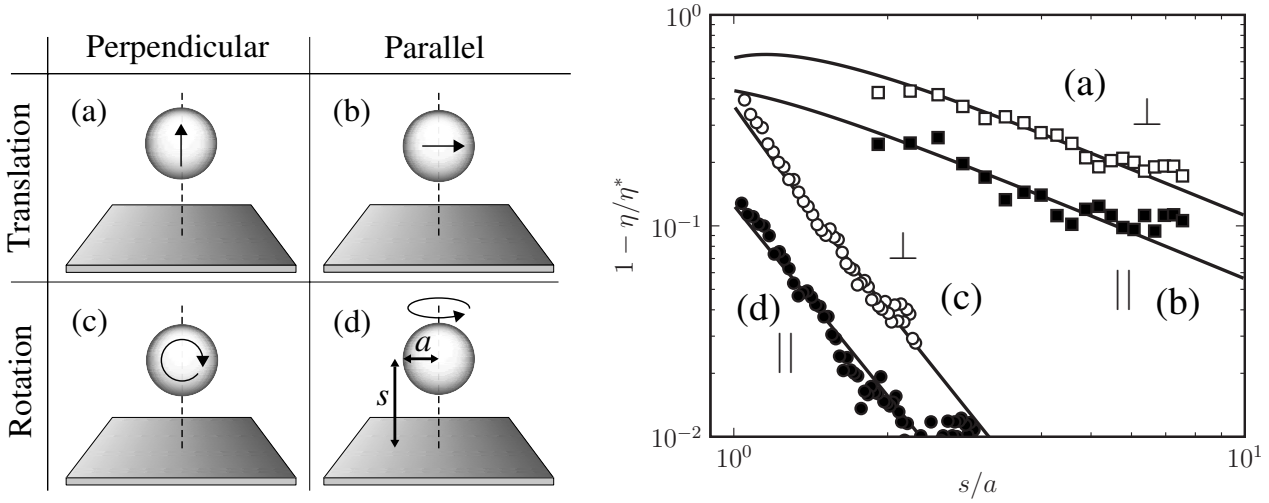

Figure 1.7: Wall effects of a plane on a sphere. Shown on the left are the four distinct ways the sphere can move with respect to the plane. In all four cases, the measured wall effects (markers), shown on the right, agree well with theoretical predictions (lines). η^* is the 'perceived' higher viscosity due to the wall effects (the viscosity is not actually higher, but the wall has the same effect on the particle's motion as if it were higher). Figure by Leach *et al.* [64]

Chapter 2

General Series Solutions to the Stokes Equations

If the flow dynamics of fluids present in optical tweezers systems can be modelled by the Stokes equations, then finding general solutions can be very useful for understanding the dynamics and viscous drag forces. This is especially true when the coordinates representing the geometry of the system is the same used to express the Stokes solutions. Lamb [67] in his book *Hydrodynamics* outlines a general series solution to the Stokes equations. His solution is most useful when using spherical coordinates since it relies on spherical harmonics. I present an alternative derivation of the general solution using vector calculus notation in this chapter, which is further extended to find new general series solutions in other orthogonal coordinate systems.

2.1 Homogeneous Equations

The linearity of the Stokes equations (1.13) allows the flow field to be split into the sum of two parts which can be solved separately,

$$\mathbf{v} = \mathbf{v}_h + \frac{1}{\eta}\mathbf{v}_p, \tag{2.1}$$

where $\mathbf{v}_h$ is the homogeneous part and the *general* solution to

$$\nabla \cdot \mathbf{v}_h = 0, \qquad \nabla^2 \mathbf{v}_h = \mathbf{0}, \tag{2.2}$$

and $\mathbf{v}_p$ is *any* particular solution that satisfies

$$\nabla \cdot \mathbf{v}_p = 0, \qquad \nabla^2 \mathbf{v}_p = \nabla p. \tag{2.3}$$

2.1.1 Helmholtz Decomposition

Therefore, provided a particular solution $\mathbf{v}_p$ can be found, the problem reduces to finding the general solution for $\mathbf{v}_h$. To do so, we use Helmholtz decomposition (the fundamental theorem of vector

calculus) to decompose the flow field into $\mathbf{v}_h = \nabla\Phi + \nabla \times \mathbf{A}$, where Φ is some smooth scalar field and $\mathbf{A}$ is some smooth vector field. The decomposition is almost unique except that Φ can differ by a harmonic function and $\mathbf{A}$ can differ by a gradient field plus a divergence free vector harmonic function. That means that we are free to constrain the divergence of $\mathbf{A}$ without losing generality.

Next we use the homogenised Stokes equations (2.2) to obtain expressions for Φ and $\mathbf{A}$. The utility of this decomposition is that it decouples the Stokes equations into an equation for Φ and an equation for $\mathbf{A}$.

Solving for Φ

The zero divergence requirement necessitates that Φ be harmonic,

$$\begin{aligned} \nabla \cdot \mathbf{v}_h &= 0, \\ \nabla \cdot (\nabla\Phi + \nabla \times \mathbf{A}) &= 0, \\ \nabla^2\Phi + \cancel{\nabla \cdot \nabla \times \mathbf{A}} &= 0, \\ \nabla^2\Phi &= 0. \end{aligned} \tag{2.4}$$

Therefore, Φ is the general solution to the Laplace equation.

Equation for A

An expression for $\mathbf{A}$ can be established by applying the vector Laplacian,

$$\begin{aligned} \nabla^2\mathbf{v}_h &= \mathbf{0}, \\ \nabla^2(\nabla\Phi + \nabla \times \mathbf{A}) &= \mathbf{0}, \\ \cancel{\nabla(\nabla^2\Phi)} + \nabla \times \nabla^2\mathbf{A} &= \mathbf{0}, \\ \nabla \times \nabla^2\mathbf{A} &= \mathbf{0}. \end{aligned} \tag{2.5}$$

Again, by the fundamental theorem of vector calculus, we know $\nabla^2\mathbf{A}$ can be represented as a gradient of a scalar field (2χ) since its curl is zero,

$$\therefore \nabla^2\mathbf{A} = 2\nabla\chi. \tag{2.6}$$

This is a very similar problem to the original Stokes equations but without the zero divergence condition. Similarly, it can be solved by splitting $\mathbf{A}$ into a particular solution and a general homogeneous solution. In this case $\mathbf{A} = \mathbf{A}_h + \mathbf{r}\chi$, where $\mathbf{r}$ is the position vector, $\nabla^2\mathbf{A}_h = \mathbf{0}$ and

$$\begin{aligned} \nabla^2(\mathbf{r}\chi) &= \mathbf{r}\nabla^2\chi + \chi\cancel{\nabla^2\mathbf{r}} + 2(\nabla\chi \cdot \nabla)\mathbf{r} \\ &= \mathbf{r}\nabla^2\chi + 2\nabla\chi \\ &= 2\nabla\chi, \quad \text{if } \nabla^2\chi = 0. \end{aligned} \tag{2.7}$$

Choosing $\mathbf{A}_h = \mathbf{0}$

It is possible to choose $\mathbf{A}_h = \mathbf{0}$ without losing generality. If the divergence of $\mathbf{A}$ is constrained to $\nabla \cdot \mathbf{r}\chi$ so that $\nabla \cdot \mathbf{A}_h = 0$ then we can show that any contribution $\mathbf{A}_h$ makes to $\mathbf{v}_h$ can be accounted for in the choice of Φ. This is because $\nabla \times \mathbf{A}_h$ can be represented as the gradient of a harmonic function. To show this, we can use similar working to the preceding sections, and decompose $\mathbf{A}_h = \nabla\alpha + \nabla \times \boldsymbol{\beta}$, where $\nabla^2\alpha = 0$ since $\mathbf{A}_h$ is divergence free. Similar to before, the vector Laplace equation constrains $\boldsymbol{\beta}$ by

$$\begin{aligned} \nabla^2 \mathbf{A}_h &= \mathbf{0}, \\ \nabla^2(\nabla\alpha + \nabla \times \boldsymbol{\beta}) &= \mathbf{0}, \\ \cancel{\nabla\nabla^2\alpha} + \nabla \times \nabla^2\boldsymbol{\beta} &= \mathbf{0}, \\ \therefore \nabla^2\boldsymbol{\beta} &= \nabla\gamma, \end{aligned} \tag{2.8}$$

where γ is some smooth scalar field. Now we can show that the curl of $\mathbf{A}_h$ is equal to the gradient of a scalar function,

$$\begin{aligned} \nabla \times \mathbf{A}_h &= \nabla \times (\nabla\alpha + \nabla \times \boldsymbol{\beta}), \\ &= \nabla \times \nabla \times \boldsymbol{\beta}, \\ &= \nabla(\nabla \cdot \boldsymbol{\beta}) - \nabla^2\boldsymbol{\beta}, \\ &= \nabla(\nabla \cdot \boldsymbol{\beta} - \gamma), \end{aligned} \tag{2.9}$$

but this function is harmonic,

$$\begin{aligned} \nabla^2(\nabla \cdot \boldsymbol{\beta} - \gamma) &= \nabla \cdot \nabla^2\boldsymbol{\beta} - \nabla^2\gamma, \\ &= \nabla \cdot \nabla\gamma - \nabla^2\gamma, \\ &= 0. \end{aligned} \tag{2.10}$$

As a result, $\mathbf{A}_h$ can be eliminated by subtracting the harmonic function $\nabla \cdot \boldsymbol{\beta} - \gamma$ from Φ. But, since Φ is an arbitrary harmonic function, $\mathbf{A}_h$ can be set to zero without losing generality. Therefore, after choosing $\mathbf{A}_h = \mathbf{0}$, the general homogeneous solution is given by

$$\mathbf{v}_h = \nabla\Phi + \nabla \times (\mathbf{r}\chi), \tag{2.11}$$

where Φ and χ are general solutions to $\nabla^2\Phi = \nabla^2\chi = 0$. This final expression for the homogeneous solution agrees with the vector calculus notation version presented (without derivation) by Happel and Brenner [60] and Pak [68].

2.1.2 Solving the Laplace Equation by Separation of Variables

Solving the homogeneous flow $\mathbf{v}_h$ and the pressure p both involve finding general solutions to the Laplace equation,

$$\nabla^2 p = \nabla^2\Phi = \nabla^2\chi = 0. \tag{2.12}$$

General series solutions for p (as well as Φ and χ) in 3D can be obtained in at least 11 coordinate systems via the method of separation of variables [69, 70]. Separation of variables finds individual separable solutions of the form $p = p_{x_1}(x_1)p_{x_2}(x_2)p_{x_3}(x_3)$, where x_1, x_2 and x_3 symbolise the three dimensional coordinates. Since the Laplace equation is linear, the general solution can be found by linear combination of these separable solutions. This can involve either summations or integrals or both.

Separation of variables works by splitting the single partial differential equation (PDE) into three ordinary differential equations (ODEs). The Laplace equation in orthogonal curvilinear coordinates is given by

$$\nabla^2 p = \frac{1}{h_1 h_2 h_3} \sum_{i=1}^{3} \frac{\partial}{\partial x_i} \left(\frac{h_1 h_2 h_3}{h_i^2} \frac{\partial p}{\partial x_i} \right) = 0, \tag{2.13}$$

where the scale factors, h_1, h_2 and h_3, are determined by the coordinate system and can be functions of the coordinates. To separate the variables the Robertson condition must be met requiring that the scale factors satisfy

$$\frac{h_2 h_3}{h_1} = s_1(x_2, x_3)t_1(x_1), \qquad \frac{h_1 h_3}{h_2} = s_2(x_1, x_3)t_2(x_2), \qquad \frac{h_1 h_2}{h_3} = s_3(x_1, x_2)t_3(x_3). \tag{2.14}$$

Separating the variables gives three equations, indexed by j,

$$\frac{1}{t_j} \frac{\partial}{\partial x_j} \left(t_j \frac{\partial p_{x_j}}{\partial x_j} \right) + (k\psi_{j,1} + l\psi_{j,2}) p_{x_j} = 0, \qquad \forall j \in \{1, 2, 3\} \tag{2.15}$$

where $\psi_{j,i}$ are functions of x_j determined by the scale factors and k and l are separation constants. Different values of the separation constants give different solutions ($p_{k,l}$), so the general solution to the Laplace equation involves the sum (for discrete values) or integral (for continuous values) of $p_{k,l}$ together with their relative contributions ($A(k,l)$) over each of these constants,

$$p = \sum_k \sum_l A(k,l) p_{k,l}, \qquad p = \sum_k \int A(k,l) p_{k,l} dl, \tag{2.16}$$

$$p = \iint A(k,l) p_{k,l} dk\, dl, \qquad \text{or} \qquad p = \int \sum_l A(k,l) p_{k,l} dk. \tag{2.17}$$

2.2 Particular Solutions

In addition to the general homogeneous solution, completing the general solution to the Stokes equations requires *any* particular solution that satisfies equation (2.3). Since the equations are linear, for every $p_{k,l}$ there is a corresponding contribution $\mathbf{v}_{k,l}$ to the particular solution that we can find independently. In Lamb's original derivation he provides a particular solution for each corresponding spherical harmonic. I wish to generalise this approach to find particular solutions in other coordinate systems as well.

2.2.1 Particular Solution Equations

Therefore, we can seek particular solutions of the partially decomposed form,

$$\begin{aligned}\mathbf{v}_{k,l} &= \nabla(pf) + p\mathbf{q}, \\ &= f\nabla p + p\nabla f + p\mathbf{q},\end{aligned} \tag{2.18}$$

where f and $\mathbf{q}$ are respectively some scalar and vector fields yet to be determined. Here p, f, and $\mathbf{q}$ can all depend on the separation constants k and l but for notational conciseness the indices are omitted for the remainder of the chapter.

The divergence of the particular solution must be zero so this condition is also enforced on its constituents

$$\begin{aligned}\nabla\cdot\mathbf{v}_{k,l} &= 0, \\ \nabla\cdot(f\nabla p + p\nabla f + p\mathbf{q}) &= 0, \\ \cancel{f\nabla^2 p} + 2\nabla f\cdot\nabla p + p\nabla^2 f + \nabla p\cdot\mathbf{q} + p\nabla\cdot\mathbf{q} &= 0.\end{aligned} \tag{2.19}$$

Similarly, the vector Laplacian condition gives

$$\begin{aligned}\nabla^2\mathbf{v}_{k,l} &= \nabla p, \\ \cancel{\nabla(\nabla\cdot\mathbf{v}_{k,l})} - \nabla\times\nabla\times\mathbf{v}_{k,l} &= \nabla p, \\ -\nabla\times\nabla\times(\nabla(pf) + p\mathbf{q}) &= \nabla p, \\ \cancel{-\nabla\times\nabla\times\nabla(pf)} - \nabla\times\nabla\times(p\mathbf{q}) &= \nabla p.\end{aligned} \tag{2.20}$$

Therefore, $\mathbf{q}$ can firstly be obtained from

$$-\nabla\times\nabla\times(p\mathbf{q}) = \nabla p, \tag{2.21}$$

and then f from

$$2\nabla f\cdot\nabla p + p\nabla^2 f + \nabla p\cdot\mathbf{q} + p\nabla\cdot\mathbf{q} = 0. \tag{2.22}$$

To solve these equations, let us represent them in arbitrary orthogonal coordinates. Equation (2.21) becomes the three equations indexed by j as

$$\begin{aligned}\frac{h_1h_2h_3}{h_j^2}\frac{\partial p}{\partial x_j} =& + \frac{\partial}{\partial x_{j+1}}\left(\frac{h_{j+2}^2}{h_1h_2h_3}\frac{\partial}{\partial x_{j+1}}(pq_jh_j)\right) + \frac{\partial}{\partial x_{j+2}}\left(\frac{h_{j+1}^2}{h_1h_2h_3}\frac{\partial}{\partial x_{j+2}}(pq_jh_j)\right) \\ & - \frac{\partial}{\partial x_{j+1}}\left(\frac{h_{j+2}^2}{h_1h_2h_3}\frac{\partial}{\partial x_j}(pq_{j+1}h_{j+1})\right) - \frac{\partial}{\partial x_{j+2}}\left(\frac{h_{j+1}^2}{h_1h_2h_3}\frac{\partial}{\partial x_j}(pq_{j+2}h_{j+2})\right),\end{aligned} \tag{2.23}$$

and equation (2.22) becomes

$$0 = \sum_{i=1}^{3}\left(\frac{q_i}{h_i}\frac{\partial p}{\partial x_i} + \frac{p}{h_1h_2h_3}\frac{\partial}{\partial x_i}\left(\frac{h_1h_2h_3}{h_i}q_i\right) + \frac{2}{h_i^2}\frac{\partial f}{\partial x_i}\frac{\partial p}{\partial x_i} + \frac{p}{h_1h_2h_3}\frac{\partial}{\partial x_i}\left(\frac{h_1h_2h_3}{h_i^2}\frac{\partial f}{\partial x_i}\right)\right). \tag{2.24}$$

2.2.2 Finding f and q

Solving for q

To solve for **q** we assume it depends only on its first component q_1, and the other components are zero. Once f is determined then linear combinations of **q** have would require the same linear combinations of f. This means individual components can be found independently and then combined later to form other solutions[1]. When **q** only depends on q_1 then it must satisfy the three equations,

$$\frac{h_2h_3}{h_1}\frac{\partial p}{\partial x_1} = +\frac{\partial}{\partial x_2}\left(\frac{h_3}{h_1h_2}\frac{\partial}{\partial x_2}(pq_1h_1)\right) + \frac{\partial}{\partial x_3}\left(\frac{h_2}{h_1h_3}\frac{\partial}{\partial x_3}(pq_1h_1)\right), \tag{2.25}$$

$$\frac{h_1h_3}{h_2}\frac{\partial p}{\partial x_2} = -\frac{\partial}{\partial x_1}\left(\frac{h_3}{h_1h_2}\frac{\partial}{\partial x_2}(pq_1h_1)\right), \tag{2.26}$$

$$\frac{h_1h_2}{h_3}\frac{\partial p}{\partial x_3} = -\frac{\partial}{\partial x_1}\left(\frac{h_2}{h_1h_3}\frac{\partial}{\partial x_3}(pq_1h_1)\right). \tag{2.27}$$

The first of the three is automatically satisfied by the other two up to an addition to pq_1h_1 of a harmonic function independent of x_1.

Now to further simplify the equations we let p be a separable solution so that $p = p_{x_1}p_{x_2}p_{x_3}$ and assume that q_1 and h_1 only depend on x_1 so that p_{x_2} and p_{x_3} cancel. Therefore, the latter two equations reduce to

$$\frac{h_1h_3}{h_2}p_{x_1} = -\frac{\partial}{\partial x_1}\left(\frac{h_3}{h_2}p_{x_1}q_1\right), \qquad \frac{h_1h_2}{h_3}p_{x_1} = -\frac{\partial}{\partial x_1}\left(\frac{h_2}{h_3}p_{x_1}q_1\right). \tag{2.28}$$

This requires that

$$\frac{\partial}{\partial x_1}\left(\frac{h_2}{h_3}\right) = \frac{\partial}{\partial x_1}\left(\frac{h_3}{h_2}\right) = 0, \tag{2.29}$$

giving

$$h_1p_{x_1} = -\frac{\partial(p_{x_1}q_1)}{\partial x_1}, \tag{2.30}$$

$$q_1(x_1) = -\frac{1}{p_{x_1}}\int h_1p_{x_1}\,dx_1. \tag{2.31}$$

Solving for f

If p is separable, **q** depends only on first component q_1 and f depends only on x_1 then equation (2.24) simplifies to

$$0 = \frac{q_1}{h_1}p'_{x_1} + \frac{p_{x_1}}{h_1h_2h_3}\frac{\partial}{\partial x_1}(h_2h_3q_1) + \frac{2}{h_1^2}f'p'_{x_1} + \frac{p_{x_1}}{h_1h_2h_3}\frac{\partial}{\partial x_1}\left(\frac{h_2h_3}{h_1}f'\right), \tag{2.32}$$

where the prime denotes $\frac{\partial}{\partial x_1}$. Multiplying by $h_1h_2h_3p_{x_1}/s_1$ and then grouping some derivatives gives

$$0 = p_{x_1}\frac{\partial}{\partial x_1}(t_1h_1q_1p_{x_1}) + \frac{\partial}{\partial x_1}\left(p_{x_1}^2t_1f'\right). \tag{2.33}$$

giving

$$f = -\int\frac{1}{t_1p_{x_1}^2}\int p_{x_1}\frac{\partial}{\partial x_1}(t_1h_1q_1p_{x_1})\,dx\,dx \tag{2.34}$$

[1]Combining the individual components of **q** can give other solutions but not necessarily all solutions that exist.

2.3 Cartesian, Cylindrical and Spherical Expressions

Now that both the general homogeneous solution $\mathbf{v}_h$ and particular solutions corresponding to separable solutions $p_{k,l}$ are established, we can finally find expressions in particular coordinate systems. Lamb's solution in spherical coordinates can be reproduced as well as solutions in Cartesian and cylindrical coordinates. Table 2.1 contains summary expressions for q_i and f in these coordinate systems, which will be further explained in this section.

	p_{x_i}	$q_i(x_i)$	$f(x_i)$	
Cylindrical $x_i = z$	$\cos nx_i$	$\frac{c_1-\sin nx_i}{n\cos nx_i}$	$c_2+\frac{1}{2n}(c_3+x_i)\tan nx_i$	Cartesian $x_i \in \{x,y,z\}$
	$\sin nx_i$	$\frac{c_1+\cos nx_i}{n\sin nx_i}$	$c_2-\frac{1}{2n}(c_3+x_i)\cot nx_i$	
	$\cosh nx_i$	$\frac{c_1-\sinh nx_i}{n\cosh nx_i}$	$c_2+\frac{1}{2n}(c_3+x_i)\tanh nx_i$	
	$\sinh nx_i$	$\frac{c_1-\cosh nx_i}{n\sinh nx_i}$	$c_2+\frac{1}{2n}(c_3+x_i)\coth nx_i$	
Spherical $x_i = r$	x_i^n	$\frac{c_1}{x_i^n}-\frac{x_i}{n+1}$	$c_2+\frac{c_3}{x_i^{2n+1}}+\frac{2c_1}{(n-1)(n+2)x_i^{n-1}}+\frac{(n+3)x_i^2}{2(n+1)(2n+3)}$	

Table 2.1: Values of q_i and f for various separable solutions in Cartesian, cylindrical and spherical coordinates. c_1, c_2 and c_3 are arbitrary constants independent of the coordinates. The symmetry of Cartesian coordinates means that x_i could be any x, y or z, but in cylindrical coordinates we only have solutions for $x_i = z$. In spherical coordinates we only have solutions for $x_i = r$.

2.3.1 Cartesian Coordinates

In Cartesian coordinates the scale factors are simply $h_x = h_y = h_z = 1$. Therefore, the separated equations from equation (2.15) become

$$\frac{\partial^2 p_x}{\partial x^2} + k p_x = 0, \qquad \frac{\partial^2 p_y}{\partial y^2} + l p_y = 0, \qquad \frac{\partial^2 p_z}{\partial z^2} + (-k-l) p_z = 0. \tag{2.35}$$

If the separation constants are $k = n^2$ and $l = m^2$ so that they are both positive, then the separable solutions are of the form

$$\cos nx \cos my \cosh \sqrt{n^2+m^2}\, z \tag{2.36}$$

or any combination of replacements of cos $\to$ sin and cosh $\to$ sinh. By symmetry of the Cartesian coordinates, the other separable solutions include

$$\cos nx \cosh my \cos \sqrt{n^2+m^2}\, z \qquad \text{and} \qquad \cosh nx \cos my \cos \sqrt{n^2+m^2}\, z \tag{2.37}$$

where the same replacements of cos $\rightarrow$ sin and/or cosh $\rightarrow$ sinh are also separable solutions. These also account for solutions when k or l are negative. Since the scale factors are all 1 we are able to find particular solutions using any of $q_x(x)$, $q_y(y)$ or $q_z(z)$. The expressions for $q_i(x_i)$ and $f(x_i)$ are included in table 2.1.

2.3.2 Cylindrical Coordinates

In cylindrical coordinates we can only find particular solutions using q_z because the scale factors are $h_r = 1$, $h_\theta = r$ and $h_z = 1$. $q_r(r)$ does not exist because h_θ/h_z depends on r and $q_\theta(\theta)$ breaks the assumption that h_θ does not depend on r. In cylindrical coordinates the separated equations from equation (2.15) become

$$r\frac{\partial}{\partial r}\left(r\frac{\partial p_r}{\partial r}\right)+(-r^2k-l)p_r=0, \qquad \frac{\partial^2 p_\theta}{\partial\theta^2}+lp_\theta=0, \qquad \frac{\partial^2 p_z}{\partial z^2}+kp_z=0. \tag{2.38}$$

p_θ must be periodic with period 2π so $l=m^2$ where $m\in\mathbb{Z}$. If $k=-n^2$ for $n\in\mathbb{R}$ so that it is negative then p_r is given by the Bessel functions of the first and second kind J_m and Y_m, but if $k=n^2$ so that it is positive then p_r is given by the modified Bessel functions of the first and second kind I_m and K_m. Therefore, the separable solutions are of the form

$$J_m(nr)\cos m\theta\cosh nz, \qquad I_m(nr)\cos m\theta\cos nz, \tag{2.39}$$

where replacing any $J_m\rightarrow Y_m$, $I_m\rightarrow K_m$, cos $\rightarrow$ sin and/or cosh $\rightarrow$ sinh gives the other separable solutions. Expressions for $q_z(z)$ and $f(z)$ are the same as the Cartesian expressions previously tabulated since the scale factors are all independent of z and the z dependent part of each separable solution is the same as in the Cartesian case.

2.3.3 Spherical Coordinates

In spherical coordinates the scale factors are $h_r = 1$, $h_\theta = r$ and $h_\phi = r\sin\theta$. So only particular solutions using $q_r(r)$ can be found since both h_θ and h_ϕ depend on r. The separated equations from equation (2.15) become

$$\frac{\partial}{\partial r}\left(r^2\frac{\partial p_r}{\partial r}\right)+kp_r=0, \quad \frac{1}{\sin\theta}\frac{\partial}{\partial\theta}\left(\sin\theta\frac{\partial p_\theta}{\partial\theta}\right)+(-k-\frac{l}{\sin^2\theta})p_\theta=0, \quad \frac{\partial^2 p_\phi}{\partial\phi^2}+lp_\phi=0. \tag{2.40}$$

Similar to cylindrical coordinates, p_ϕ is periodic with period 2π so $l=m^2$ where $m\in\mathbb{Z}$. $k=-n(n+1)$ where $n\in\mathbb{Z}$ because p_θ is non-singular at the poles $\theta=0$ and $\theta=\pi$. So the separable solutions are of the form

$$r^nP_m^n(\cos\theta)\cos m\phi, \tag{2.41}$$

where P_m^n are the associated Legendre functions and the replacements $r^n\rightarrow r^{-n-1}$ and/or $\cos m\phi\rightarrow\sin m\phi$ are also separable solutions. Table 2.1 includes expressions for $q_r(r)$ and $f(r)$. Choosing

$c_1 = c_2 = c_3 = 0$ gives

$$f = \frac{(n+3)r^2}{2(n+1)(2n+3)}, \qquad \mathbf{q} = [q_r, q_\theta, q_\phi]^T = \left[-\frac{r}{n+1}, 0, 0\right]^T, \tag{2.42}$$

which recovers Lamb's general series solution

$$\mathbf{v} = \sum_{n=-\infty}^{\infty} \left[\frac{(n+3)r^2\nabla p_n - 2n\mathbf{r}p_n}{2\eta(n+1)(2n+3)} + \nabla\Phi_n + \nabla\times(\mathbf{r}\chi_n) \right], \tag{2.43}$$

where p_n, Φ_n and χ_n are general solutions to the Laplace equation,

$$p_n = r^n \sum_{m=0}^{n} P_n^m(\cos\theta)(a_{mn}\cos m\phi + \tilde{a}_{mn}\sin m\phi), \tag{2.44}$$

$$\Phi_n = r^n \sum_{m=0}^{n} P_n^m(\cos\theta)(b_{mn}\cos m\phi + \tilde{b}_{mn}\sin m\phi), \tag{2.45}$$

$$\chi_n = r^n \sum_{m=0}^{n} P_n^m(\cos\theta)(c_{mn}\cos m\phi + \tilde{c}_{mn}\sin m\phi). \tag{2.46}$$

2.4 Force and Torque

Given the series representation of the flow field and pressure, the force and torques acting on surfaces can be evaluated in terms of the series coefficients. This means that once the series coefficients have been established from the boundary conditions then the force and torque acting on a surface are also realised.

2.4.1 Spherical coordinates

Lamb's series solution in spherical coordinates are especially useful when integrating the force and torque about a sphere because of two reasons. The first is that the orthogonality properties of the spherical harmonics mean that all except $n = -2$ terms vanish when integrating. This means that the Cartesian components of force and torque acting on a sphere can each be related to exactly one of these low order coefficients. The second is that the flux of angular and linear momentum through any closed surface must be invariant of the surface shape. This requires that the force and torque acting on any closed surface be the same. This means that the expressions of the force and torque acting on a sphere generalise to any closed surface containing the origin.

From section 1.2.2 we know that the force density acting on the surface of a sphere with radius r centred at the origin is given by

$$\mathbf{P} = \frac{1}{r}\begin{bmatrix}\sigma_{rr} & \sigma_{r\theta} & \sigma_{\phi r}\end{bmatrix}^T. \tag{2.47}$$

where σ_{rr}, $\sigma_{r\theta}$ and $\sigma_{\phi r}$ are elements of the stress tensor in spherical coordinates (expressions available in appendix A). This force density in terms of Lamb's series solution shown in equation (2.43) is given by Happel and Brenner [60],

$$\mathbf{P} = \frac{\eta}{r}\sum_{n=-\infty}^{\infty}\left[\frac{n(n+2)r^2\nabla p_n - (2n^2+4n+3)\mathbf{r}p_n}{\eta(n+1)(2n+3)} + 2(n-1)\nabla\Phi_n + (n-1)\nabla\times(\mathbf{r}\chi_n)\right]. \tag{2.48}$$

The surface torque density $\mathbf{T} = \mathbf{r} \times \mathbf{P}$ is

$$\mathbf{T} = \frac{\eta}{r} \sum_{n=-\infty}^{\infty} \left[-\frac{n(n+2)r^2 \nabla \times (\mathbf{r} p_n)}{\eta(n+1)(2n+3)} - 2(n-1)\nabla \times (\mathbf{r}\Phi_n) + (n-1)r^2 \nabla \chi_n - n(n-1)\mathbf{r}\chi_n \right]. \quad (2.49)$$

The total force and torque are evaluated by integrating over the whole spherical surface. However, most terms vanish because of the following properties of spherical harmonics

$$\iint_S \nabla \times (\mathbf{r} p_n)\, dS = \mathbf{0}, \qquad \iint_S \nabla p_n\, dS = \begin{cases} 4\pi r^2 \nabla p_1, & n = 1 \\ \mathbf{0}, & n \neq 1 \end{cases} \quad (2.50)$$

$$\iint_S \mathbf{r} p_n\, dS = \begin{cases} \frac{4\pi r^4}{3} \nabla p_1, & n = 1 \\ \frac{4\pi r}{3} \nabla (r^3 p_{-2}), & n = -2 \\ \mathbf{0}, & n \notin \{1, -2\} \end{cases} \quad (2.51)$$

as well as similar expressions for Φ_n and χ_n. Therefore, the force and torque acting on the sphere in Cartesian vector components are

$$\mathbf{F} = \iint_S \mathbf{P}\, dS = -4\pi \ \ \nabla (r^3 p_{-2}) = -4\pi \ \ \begin{bmatrix} -a_{1,-2} & -\tilde{a}_{1,-2} & a_{0,-2} \end{bmatrix}^T, \quad (2.52)$$

$$\mathbf{G} = \iint_S \mathbf{T}\, dS = -8\pi\eta \nabla (r^3 \chi_{-2}) = -8\pi\eta \begin{bmatrix} -c_{1,-2} & -\tilde{c}_{1,-2} & c_{0,-2} \end{bmatrix}^T. \quad (2.53)$$

Evidently, the force and torque acting on the sphere are independent of the sphere's radius. However, as stated before, this result also applies to any closed surface, regardless of shape.

2.4.2 Concentric Spheres

It is useful to have a concrete example of how the series solutions can be used to find flow fields and wall effects in practice. To do so, let us again use the example of concentric spheres. In addition to the rotational wall effects previously outlined in section 1.2.2, we can also use Lamb's series solution to find flow fields and wall effects when the internal sphere translates.

Rotational Wall Effects

In the rotational case we have a sphere of radius a rotating with angular velocity Ω inside a larger fluid-filled sphere of radius b (figure 1.6). All the spherical vector components of the flow field are zero at the boundaries except $v_\phi = \Omega a \sin\theta$ at $r = a$. These boundary conditions are sufficient to constrain the series coefficients to give a unique solution. Having $v_r = v_\theta = 0$ at both boundaries requires that for all n, $p_n = \Phi_n = 0$. Next we can use the orthogonality of the spherical harmonics. Noticing that $P_1^0(\cos\theta) = P_{-2}^0(\cos\theta) = \cos\theta$, we can eliminate all except the $n = 1$ and $n = -2$ terms where $m = 0$. Therefore the flow field satisfies

$$\mathbf{v} = \nabla \times (\mathbf{r}(\chi_{-2} + \chi_1)), \quad (2.54)$$

$$= \begin{bmatrix} 0 & 0 & \sin\theta r \left(\frac{c_{0,-2}}{r^3} + c_{0,1} \right) \end{bmatrix}^T. \quad (2.55)$$

To satisfy the boundary conditions

$$c_{0,1} = -\Omega \frac{a^3}{b^3 - a^3}, \qquad c_{0,-2} = \Omega \frac{a^3 b^3}{b^3 - a^3}. \tag{2.56}$$

This corresponds to the flow field in spherical vector components

$$\mathbf{v} = \begin{bmatrix} 0 & 0 & \Omega \sin\theta \frac{a^3 b^3}{b^3 - a^3} r \left(\frac{1}{r^3} - \frac{1}{b^3} \right) \end{bmatrix}^T, \tag{2.57}$$

which agrees with the result previously found in section 1.2.2. Similarly, the forces and torques in section 1.2.2 agree with those found using equations (2.52) and (2.53),

$$\mathbf{F} = -4\pi \begin{bmatrix} -a_{1,-2} & -\tilde{a}_{1,-2} & a_{0,-2} \end{bmatrix}^T = \mathbf{0}, \tag{2.58}$$

$$\mathbf{G} = -8\pi\eta \begin{bmatrix} -c_{1,-2} & -\tilde{c}_{1,-2} & c_{0,-2} \end{bmatrix}^T = \begin{bmatrix} 0 & 0 & -8\pi\eta\Omega \frac{a^3 b^3}{b^3 - a^3} \end{bmatrix}^T, \tag{2.59}$$

where these are given in Cartesian vector components.

Translational Wall Effects

We can also use Lamb's solution to find the flow field, force and wall effects when the inner sphere translates rather than rotates. If it translates along the positive z axis with velocity v then the boundary conditions at $r = a$ become

$$v_r = v\cos\theta, \qquad v_\theta = -v\sin\theta, \qquad v_\phi = 0, \tag{2.60}$$

while v_r, v_θ and v_ϕ are still zero at $r = b$. Similar to the rotational case, the orthogonality of the spherical harmonics allows us to eliminate all except the $n = 1$ and $n = -2$ terms with $m = 0$. Having $v_\phi = 0$ at both boundaries requires that $\chi_n = 0$ for all n. Therefore the flow field must satisfy,

$$\mathbf{v} = \left[\cos\theta \left(\frac{a_{0,-2}}{r\eta} + \frac{r^2 a_{0,1}}{10\eta} - \frac{2b_{0,-2}}{r^3} + b_{0,1} \right), \quad -\sin\theta \left(\frac{a_{0,-2}}{2r\eta} + \frac{r^2 a_{0,1}}{5\eta} + \frac{b_{0,-2}}{r^3} + b_{0,1} \right), \quad 0 \right]^T. \tag{2.61}$$

Enforcing the boundary conditions provides four simultaneous equations for $a_{0,1}$, $a_{0,-2}$, $b_{0,1}$ and $b_{0,-2}$ giving,

$$a_{0,1} = \frac{30ab(b^2 - a^2)\eta v}{(b-a)^4(4a^2 + 7ab + 4b^2)}, \qquad a_{0,-2} = \frac{6ab(b^5 - a^5)\eta v}{(b-a)^4(4a^2 + 7ab + 4b^2)}, \tag{2.62}$$

$$b_{0,-2} = \frac{a^3 b^3 (b^3 - a^3) v}{(b-a)^4(4a^2 + 7ab + 4b^2)}, \qquad b_{0,1} = -\frac{a(9b^5 - 5a^2 b^3 - 4a^5) v}{(b-a)^4(4a^2 + 7ab + 4b^2)}. \tag{2.63}$$

From equations (2.52) and (2.53) we see that all the force and torque components acting on the inner sphere are zero except for a force in the z direction,

$$F_z = -4\pi a_{0,-2}. \tag{2.64}$$

To find the effect of the outer wall on this force, we consider the case where the inner sphere translates in a free fluid. Taking the limit as the outer radius b goes to infinity reproduces the well known result

$$\lim_{b\to\infty} F_z = -6\pi\eta v a. \tag{2.65}$$

The wall effect is therefore,

$$\frac{F_z}{-6\pi\eta v a} = \frac{4b(b^5 - a^5)}{(b-a)^4(4a^2 + 7ab + 4b^2)} = \frac{4(1 - (a/b)^5)}{(1 - a/b)^4(4(a/b)^2 + 7(a/b) + 4)}. \tag{2.66}$$

2.5 Point Matching

For most problems, finding the flow field and hydrodynamic forces using these series solutions involves choosing appropriate series coefficients so that the flow field satisfies the boundary conditions. Unlike the preceding example of concentric spheres, however, it is not feasible to determine these coefficients analytically for most geometries. Instead the series coefficients are obtained numerically using a point matching method similar to that used by Nieminen *et al.* [71].

To evaluate the coefficients, the velocity at sample points on the boundaries are substituted into the series to form a system of simultaneous linear equations. By terminating the series at a sufficiently high order and choosing many more points than coefficients, the system can be solved using least squares. If the goal is to find the force or torque acting on a surface using Lamb's series solution, such as required when evaluating the drag tensor of a particle, then the system needs only be large enough for these early terms to converge.

2.5.1 Uniform Point Cloud

Lamb's series relies on spherical harmonics which makes it effective in problems containing closed surfaces boundaries that encapsulate the origin. Therefore, angular points should be sampled to be approximately uniform over a sphere. However, choosing coordinates of N points on a sphere so that they are approximately uniform is a non-trivial problem. A simple linear grid over θ and ϕ would over-sample the poles while under-sampling the equator for the same number of points.

To generate points that more uniformly cover the domain we use points that lie along a spiral that wraps around a unit sphere from pole to pole. The position vector of this spiral in Cartesian vector components can be given in spherical coordinates,

$$\mathbf{r}(\theta) = \begin{bmatrix} \sin\theta\cos\alpha\theta & \sin\theta\sin\alpha\theta & \cos\theta \end{bmatrix}^T, \tag{2.67}$$

where the azimuth is parametrised by the polar angle, $\phi = \alpha\theta$. α is a positive constant which is yet to be determined by optimising the uniformity of the points over the sphere.

The length of the spiral ($L(\theta)$) as parametrised by the polar angle can be calculated by

$$\begin{aligned} L(\theta) &= \int_0^\theta \left| \frac{\partial \mathbf{r}}{\partial \theta'} \right| d\theta' \\ &= \int_0^\theta \sqrt{1+\alpha^2\sin^2\theta'}\; d\theta' \\ &\approx \int_0^\theta \alpha\sin\theta'\, d\theta' = \alpha(1-\cos\theta), \qquad \alpha \gg 1. \end{aligned} \tag{2.68}$$

The final expression is an approximation valid when α is large, and tells us that the total length of the spiral is approximately 2α. Figure 2.1 demonstrates the validity of the approximation, even for not very large values of α, by plotting the relative error of the total length.

The spiral ends when $\theta = \pi$ so the number of full rotations in the spiral is $\alpha/2$. Therefore, as shown in figure 2.2, a good way to maximise the uniformity of the points is to ensure that the distance

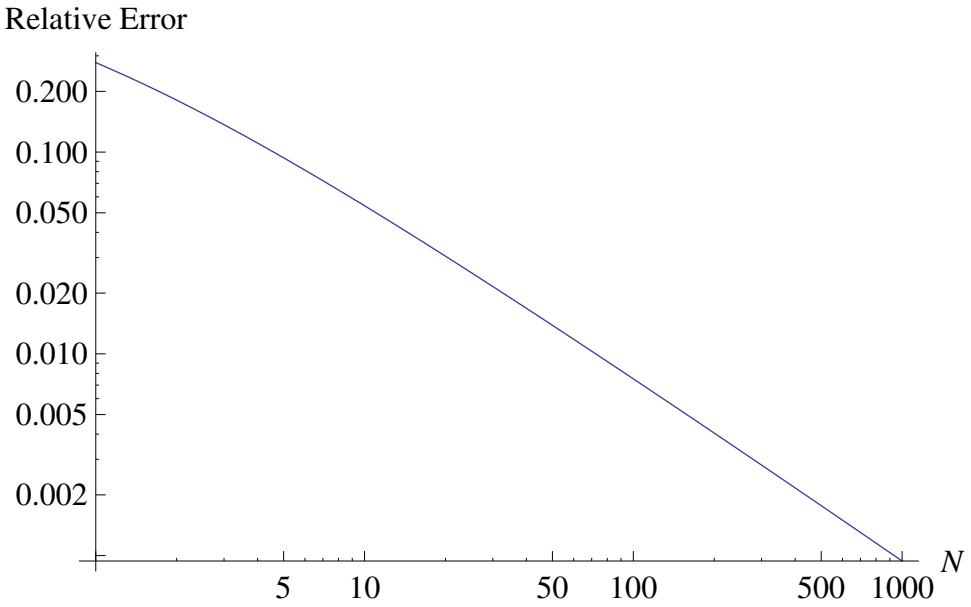

Figure 2.1: The relative error of the total spiral length when $\alpha = \sqrt{\pi N}$.

between consecutive points on the spiral[2] is equal to the distance between consecutive layers of the spiral,

$$\frac{2\alpha}{N} = \frac{\pi}{\alpha/2}, \qquad \Rightarrow \qquad \alpha = \sqrt{\pi N}\,. \tag{2.69}$$

The points on the spiral should be linearly spaced along the curve. Therefore, we need to parametrise θ in terms of a new parameter, t, such that the length of the spiral is linear with respect to t. Requiring $\theta(-1) = 0$ and $\theta(1) = \pi$ gives

$$L(\theta(t)) = \alpha(1-\cos\theta(t)) = \alpha(1+t), \qquad \Rightarrow \qquad \theta(t) = \arccos(-t). \tag{2.70}$$

Therefore, points can be approximately uniformly spaced on a sphere by the following:

$$\theta(t) = \arccos(-t), \quad \phi(t) = \sqrt{\pi N}\,\arccos(-t), \quad \text{where } t \in \left\{ \frac{2k-N-1}{N-1} | k \in \mathbb{Z} \cap [1,N] \right\}. \tag{2.71}$$

[2]If the first and last points lie on the poles, then the distance between consecutive points on the spiral is actually $L(\pi)/(N-1)$. The $L(\pi) \approx 2\alpha$ approximation already assumes $\alpha \gg 1$, therefore $N-1$ can also be simplified to just N since $N > \alpha$ over the relevant domain.

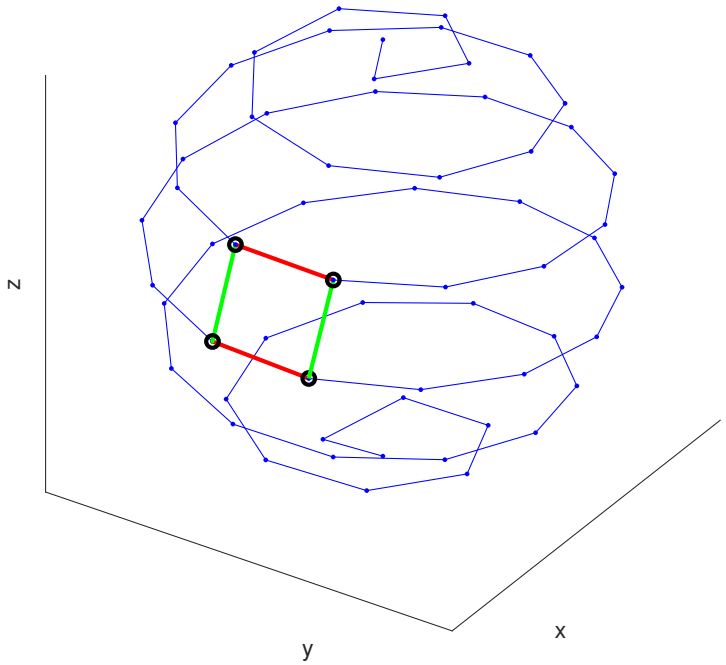

Figure 2.2: An example of evenly spreading 60 points over a sphere using a spiral by requiring the distance between consecutive points (shown in red) to be about equal to the distance between consecutive layers (shown in green).

The following peer reviewed journal article has been adapted for Chapter 3.

[1] **L. J. Gibson**, S. Zhang, A. B. Stilgoe, T. A. Nieminen, and H. Rubinsztein-Dunlop. Active rotational and translational microrheology beyond the linear spring regime. *Physical Review E*, 95:042608, April 2017.

Contributor	Statement of contribution	%
L. J. Gibson	Conceived the project	50
	Performed the experiments	10
	Results analysis and interpretation	70
	Wrote the paper	80
	Theoretical and numerical calculation	80
S. Zhang	Performed the experiments	90
	Results analysis and interpretation	30
	Wrote the paper	5
A. B. Stilgoe	Conceived the project	10
	Wrote the paper	5
T. A. Nieminen	Conceived the project	20
	Theoretical and numerical calculation	20
	Wrote the paper	5
H. Rubinsztein-Dunlop	Conceived the project	20
	Wrote the paper	5

I am the primary author of this paper, contributing the strong majority of both analysis of results and theoretical work. However, the actual experiments in the laboratory were predominantly conducted by Shu Zhang. The other authors also gave strong contributions to the original conception of the project as well as other minor contributions.

Chapter 3

Optical Tweezers Microrheology

The use of optical tweezers to measure viscoelasticiy via hydrodynamic forces acting on an optically trapped probe particle was introduced in section 1.1.2. Generally, the precision of these microrheometers is limited by Brownian motion and low frequency changes to the system. This chapter, based on published work by Gibson *et al.* [1], establishes a theoretical framework whereby error in measurements of the complex shear modulus can be significantly reduced by analysing the motion of a spherical particle driven by non-linear rather than linear forces. This method easily increases the signal strength enough to significantly reduce the measurement time for the same error making it more applicable in slowly changing microscopic systems, such as a living cell. Furthermore, in section 3.4.2 some key experimental results from Zhang *et al.* [2] are presented[1] as an example where the new theory was applied to measure viscoelasticity of real biological samples that are not accessible to macrorheometry.

3.1 Introduction

The strength of a microrheometer can be assessed by its ability to perform accurate broad-band measurements of viscoelasticity within microscopic systems. In particular, there is great interest in improving methods for conducting measurements within living biological systems, such as a cell [16–20].

Particle tracking microrheometers have proven to be a good candidate for accomplishing such a task [19–21]. They work by tracking the motion of one or more particles embedded in the pertinent medium. The complex shear modulus $G^*(\omega)$ (see section 1.1.2), a frequency (ω) dependent measure of linear viscoelasticity, can be inferred from the way the particles move [29, 38, 40].

Biological systems are often very small or highly inhomogeneous [72]. So, tracking individual particles can be more practical since the measurement is more localised than tracking multiple particles (such as in diffusing wave spectroscopy [73, 74]). The motion of a single tracked particle can either be driven passively, where Brownian motion is the primary driving force, or actively, where Brownian

[1] I am the second author of Zhang, *et al.* [2].

motion acts as a noise on top of another external driving force. For example, Bennett *et al*. [40] trapped a single spherical birefringent particle using optical tweezers. The particle's birefringence also allowed it to be angularly trapped when using a linearly polarised laser beam. In this particular example, the angular motion driven by thermal fluctuations allowed $G^*(\omega)$ to be calculated using statistical methods including autocorrelations of quickly sampled positions. Therefore, passive methods tend to be more successful at measuring higher frequency viscoelasticity. Conversely, passive methods require too much time to resolve lower frequency viscoelasticty precisely [37, 38] in slowly changing systems [52, 75].

Active methods, in which the particle is driven by some other force, often eliminate Brownian noise by averaging over a repeated motion. The average Brownian motion reduces towards zero leaving only the nonstochastic motion. For example, Preece *et al.* [38] used optical tweezers to trap a spherical particle within two alternating spatially offset traps. The particle switched between one stable equilibrium to another when one beam was turned off and the other turned on. The linear motion of the particle as it fell into each trap was measured and used to calculate $G^*(\omega)$.

Evidently, it is possible to measure viscoelasticity by examining either rotational or linear motion. Therefore, the aim of this chapter is to outline and test a generalised theory applicable to either kind of motion. This theory describes how to obtain $G^*(\omega)$ from repeated measurements of a particle falling into an equilibrium position under the influence of both Brownian noise and a position dependent force.

For the sake of simplicity, the previous theory (such as that used by Preece *et al.*) assumed a force that is linearly dependent on position. For small displacements this is often a valid assumption. However, as will be subsequently shown in section 3.3, the signal strength can be significantly increased by allowing the particle to fall into position from outside the linear regime. Increasing the signal strength of each individual measurement can appreciably reduce the total measurement time, thereby justifying application of this method in dynamic biological systems such as a living cell. Therefore, the theory outlined here accounts for non-linear driving forces (not to be confused with non-linear motion or non-linear viscoelasticity).

To confirm the validity of the theory in at least one example, experimental measurements in both viscous and viscoelastic fluids conducted by an optical tweezers microrheometer are also examined. The different analysis methods are applied to the same data to compare the accuracy as well as the frequency range in which the viscoelasticity can be resolved. Some additional key results from Zhang *et al.* [2] are also presented briefly as an example of real application of the method.

It should be stressed that although the theory is only experimentally verified in this chapter using optical tweezers measurements, the analysis is not predicated on that mode of particle manipulation. Provided the driving force is characterisable, this theory could also be applied to many other systems such as magnetic or acoustic tweezers.

3.2 Theory

For simplicity, the following theory is expressed in terms of rotational dynamics. However, obtaining the corresponding results for linear motion at any step can be achieved by a simple substitution. Angle, moment of inertia, torque and rotational drag can be replaced by their respective linear counterparts: linear position, mass, force and linear drag.

3.2.1 Equation of Motion

*j*th Flip Langevin Equation

Consider a microscopic spherical particle centred at the origin with a fixed centre of mass. The particle, embedded in a fluid with linear viscoelasticity, is free to rotate about the z-axis influenced by Brownian motion, viscoelastic drag and an angular dependent driving torque. The particle should have a stable equilibrium angle such that it becomes trapped at a root of the driving torque function. Repeatedly dropping the particle into the trap from an outside position allows the Brownian noise to be mitigated by averaging many drops.

With a moment of inertia I, the stochastic evolution of the azimuthal angle (ϕ_j) of the jth drop can be modelled by a generalised Langevin equation [29, 40]

$$I\ddot{\phi}_j = \tau_j(t) - \int_{-\infty}^{t} \zeta(t-t_l)\dot{\phi}_j(t_l)\,dt_l - \chi T(\phi_j). \tag{3.1}$$

The total torque ($I\ddot{\phi}_j$) on the sphere at time t is the sum of the driving torque ($-\chi T(\phi_j)$) that forms the trap, the viscoelastic torque ($-\int_{-\infty}^{t}\zeta(t-t_l)\dot{\phi}_j(t_l)dt_l$ with generalised memory function $\zeta(t)$) from the fluid and the thermal torque ($\tau_j(t)$) from Brownian motion.

Properties of the Driving Torque Function

Without loss of generality, the stable equilibrium angle is set to 0 with positive trap stiffness χ so that $T(0) = 0$ and $T'(0) = 1$. In contrast to the dot symbol in equation (3.1) which denoted a time derivative, here the prime symbol indicates a spatial derivative. The trap potential is assumed to be symmetric about the equilibrium whereby the so called driving torque function, $T(\phi)$, is a continuously differentiable odd function. Hence, for small deviations about the equilibrium, the Taylor series of $T(\phi)$ to fifth order is given by

$$T(\phi) = \phi + \frac{T_3}{3!}\phi^3 + \frac{T_5}{5!}\phi^5 + \dots \tag{3.2}$$

where $T_n = T^{(n)}(0)$. Note that all even terms in the series are zero since $T(\phi)$ is an odd function.

In order for the particle to be pulled into the $\phi = 0$ equilibrium the driving torque ($-\chi T(\phi)$) must have opposite sign to the position. Therefore, the torque function ($T(\phi)$) must have the same sign as the position, $\text{sign}(T(\phi)) = \text{sign}(\phi)$. This requirement can limit the allowed positions if the torque changes sign. Therefore, if there exists an angle $\phi = R > 0$ such that $T(R) = 0$, then the domain must be restricted to $|\phi| < R$. Similarly, if there exists a singularity at angle $\phi = R > 0$ such that

$\lim_{\phi \to R} T(\phi)^{-1} = 0$, then the domain is also restricted to $|\phi| < R$. Since this restriction applies to all roots/singularities (except for $\phi = 0$) R is chosen to be the smallest positive root/singularity. If $T(\phi)$ has no additional roots to $\phi = 0$ and is continuously differentiable over all $\mathbb{R}$, then the domain is unrestricted, $\phi \in \mathbb{R}$.

Stokes Flow

Particle tracking microrheometers typically operate with microscopic particles. Therefore, it is likely that the fluid state has a low Reynolds number ($\mathscr{R} \ll 1$) and hence undergoes Stokes flow [40]. The inertial term $I\ddot{\phi}_j$ in equation (3.1) is, consequently, negligible relative to the others and can be ignored, leaving

$$\tau_j(t) = \int_{-\infty}^{t} \zeta(t - t_l)\dot{\phi}_j(t_l)\, dt_l + \chi T(\phi_j). \tag{3.3}$$

Generalised Memory Function

The time dependent generalised memory function, $\zeta(t)$, describes the ratio of viscoelastic torque to an instantaneous step rotation of the particle. Hence, it is proportional to the fluid's relaxation modulus [29],

$$\zeta(t) = \alpha G_r(t), \tag{3.4}$$

where α depends on the geometry of the probe particle as well as the type of motion. Therefore, the Langevin equation relates the fluid viscoelastiticy to the angular position by

$$\tau(t) = \alpha \int_{-\infty}^{t} G_r(t - t_l)\dot{\phi}_j(t_l)\, dt_l + \chi T(\phi_j). \tag{3.5}$$

For a sphere of radius a undergoing rotational or linear motion

$$\alpha = 8\pi a^3, \text{ or } \alpha = 6\pi a, \tag{3.6}$$

respectively [76].

3.2.2 Linear Case

Normalisation

If $T(\phi)$ is a non-linear function, then the Langevin equation (3.5) is a non-linear differential equation. This poses a problem for any repeated measurements in which the initial position of each flip varies. If the Langevin equation were linear then the position could be normalised by dividing the equation by the initial angle.

Previously, to obtain a linear differential equation the flipping angle was assumed to be small such that the driving torque could be approximated by its Taylor series (equation (3.2)) to 1st order,

$$T(\phi) \approx \phi. \tag{3.7}$$

In this case, transforming to the normalised angle $\varphi_j = \frac{\phi_j}{\phi_j(0)}$ so that $\varphi_j(0) = 1$ gives

$$\frac{\tau_j(t)}{\phi_j(0)} = \alpha \int_{-\infty}^{t} G_r(t-t_l)\dot{\varphi}_j(t_l)\,dt_l + \chi\varphi_j. \tag{3.8}$$

Notice that, after normalisation the Brownian motion term is inversely proportional to the initial position $\phi_j(0)$. Therefore, to minimise the effect of Brownian motion the initial angle should be maximised, but only within the allowed domain that satisfies the Taylor series small angle approximation. Thus, there exists some optimal angle whereby the total error contributed by Brownian motion and the Taylor series is minimised. The value of this optimal angle and relative error is quantified later in section 3.3.1.

Average Flip

The Brownian noise can be reduced by averaging n repeated flips. Assuming each flip is independent of the others, the normalised linear Langevin equations ((3.8)) for each rotation can be averaged,

$$0 = \alpha \int_{0}^{t} G_r(t-t_l)\dot{\varphi}(t_l)\,dt_l + \chi\varphi. \tag{3.9}$$

φ represents the expected normalised angle and is estimated using a finite average of all n flips,

$$\varphi \approx \frac{1}{n}\sum_{j=1}^{n}\varphi_j. \tag{3.10}$$

Provided that the time between flips is much longer than the time it takes for the particle to reach equilibrium, each flip should 'forget' the previous one and finish with an average velocity of zero. Mathematically, this is expressed as $\dot{\varphi}(t) = 0$, for $t < 0$, which truncates the memory integral at $t = 0$. The average Brownian motion is also assumed to be zero, removing the corresponding term entirely.

Viscous Fluid

A purely viscous fluid without any elasticity does not 'remember' any past motion. Its relaxation modulus is proportional to a Dirac delta function, $G_r(t) = \eta\delta(t)$, where η is the dynamic viscosity. With this relaxation modulus, equation (3.9) simplifies to a simple first order ordinary differential equation,

$$0 = \alpha\eta\dot{\varphi} + \chi\varphi, \tag{3.11}$$

with a well known solution,

$$\varphi = e^{-kt}, \text{where } k = \frac{\chi}{\alpha\eta}. \tag{3.12}$$

Evidently, the viscosity is inversely related to the decay rate of the angle over time, k.

Unilateral Fourier Transform

More generally, obtaining linear viscoelasticity from the dynamics requires the use of a unilateral Fourier transform (UFT). Represented by a tilde, the UFT is defined by

$$\tilde{f}(\omega) = \int_0^\infty f(t)e^{-i\omega t}\,dt. \tag{3.13}$$

Applying the UFT to equation (3.9) transforms the convolution integral into a product that can be easily manipulated,

$$0 = \alpha\tilde{G}_r(\omega)\,(i\omega\tilde{\varphi} - 1) + \chi\tilde{\varphi}. \tag{3.14}$$

The relaxation modulus, $G_r(t)$, is related to the time domain conjugate of $G^*(\omega)$ by

$$G^*(\omega) = i\omega\tilde{G}_r(\omega). \tag{3.15}$$

Therefore, $G^*(\omega)$ can be expressed in terms of $\tilde{\varphi}$ by rearranging equation (3.14),

$$G^*(\omega) = \frac{\chi}{\alpha}\frac{i\omega\tilde{\varphi}}{1 - i\omega\tilde{\varphi}}. \tag{3.16}$$

Equation (3.16) relates the linear viscoelasticity to the average motion of the particle at different time scales.

3.2.3 Non-linear Case

The theory presented thus far acts mostly as a summary of already known methodology for the purpose of juxtaposition. This section will now adjust the theory to account for a non-linear driving torque function.

Viscous Case

Consider the average behaviour given by a non-linear driving torque function in a viscous fluid. The Langevin equation is similar to equation (3.11), but is a non-linear ordinary differential equation,

$$0 = \alpha\eta\dot{\phi} + \chi T(\phi). \tag{3.17}$$

Note the assumption that

$$T(\phi) \approx \frac{1}{n}\sum_{j=1}^{n} T(\phi_j), \tag{3.18}$$

which should be valid provided the deviations from the average of each individual flip are not too large.

Variable Transform

The non-linearity of equation (3.17) makes it non-normalisable in terms of ϕ. However, applying a variable transformation can make it normalisable in terms of a different variable,

$$\Psi(\phi) = \exp\left(\int \frac{d\phi}{T(\phi)}\right). \tag{3.19}$$

More specifically, the new position variable Ψ is defined as the solution to

$$\Psi = T\Psi', \text{ s.t. } \Psi'(0) = 1. \tag{3.20}$$

Applying this transformation linearises equation (3.17),

$$0 = \alpha\eta\dot{\Psi} + \chi\Psi, \tag{3.21}$$

which, like the viscous linear case, has an exponential solution,

$$\psi = e^{-kt}, \text{ where, } \psi = \frac{\Psi}{\Psi(\phi_0)}, \text{ and, } \phi_0 = \phi(0). \tag{3.22}$$

Properties of Ψ

The definition of Ψ in equation (3.20) ensures that it is a strictly increasing continuously differentiable odd function of ϕ over the whole domain.

Its Taylor series is given by

$$\Psi(\phi) = \phi + \frac{-T_3}{2\times 3!}\phi^3 + \frac{5T_3^2 - T_5}{4\times 5!}\phi^5 + \dots \tag{3.23}$$

where the derivatives of Ψ at $\phi = 0$ can be expressed in a recursive form as a discrete convolution,

$$\Psi_n = -n! \sum_{j=1}^{\frac{n-1}{2}} \frac{n-2j}{n-1} \frac{\Psi_{n-2j}}{(n-2j)!} \frac{T_{2j+1}}{(2j+1)!}, \tag{3.24}$$

where $\Psi_n = \Psi^{(n)}(0)$ and $\Psi_1 = 1$.

Finding the radius of convergence of this Taylor series in general has proven difficult. However, by dividing equation (3.24) by Ψ_n and taking the $n \to \infty$ limit, it can be shown that if $\Psi_i \geq 0$ for all derivatives, then the radius of convergence either covers the whole domain or is at least as large as the radius of convergence of the $T(\phi)$ Taylor series described in section 3.2.1.

Solution in Terms of ϕ by Inverting Ψ

Finding the solution to equation (3.17) in terms of the original position variable, ϕ, can be achieved by applying the inverse variable transformation to the solution in terms of Ψ given by equation (3.22),

$$\phi = \Psi^{-1}(\Psi) = \Psi^{-1}\left(\Psi(\phi_0)e^{-kt}\right). \tag{3.25}$$

The Taylor series of the inverse function $\Psi^{-1}(\Psi)$ can be found by series reversion [69] of equation (3.23),

$$\Psi^{-1}(\Psi) = \Psi + \frac{T_3}{2\times 3!}\Psi^3 + \frac{5T_3^2+T_5}{4\times 5!}\Psi^5 + \dots \tag{3.26}$$

Therefore, by applying the Taylor series of both Ψ and Ψ^{-1} to equation (3.25) the solution to equation (3.17) in terms of time and initial position can be found in a series form,

$$\phi = \phi_0 e^{-kt} - \phi_0^3\left(e^{-kt} - e^{-3kt}\right)\frac{T_3}{2\times 3!} + \dots \quad . \tag{3.27}$$

Note that the series is always exactly correct at the time bounds $t = 0$ and $t \to \infty$ irrespective of the truncation degree. The first term is the solution under the small angle approximation and each successive term adds corrections to the position between the time bounds.

Unnormalised Analysis Viscoelastic Fluid

Now consider the average dynamics of a particle in a viscoelastic fluid driven by a non-linear torque function. Without normalisation, equation (3.5) can be averaged. Similar to equation (3.9), the average thermal torque and angular velocity for $t < 0$ are zero,

$$0 = \alpha\int_0^t G_r(t-t_l)\dot{\phi}(t_l)\,dt_l + \chi T(\phi). \tag{3.28}$$

Following the steps outlined in section 3.2.2, applying the unilateral Fourier transform allows $G^*(\omega)$ to be evaluated,

$$G^*(\omega) = \frac{\chi}{\alpha}\frac{i\omega\tilde{T}}{\phi_0 - i\omega\tilde{\phi}}. \tag{3.29}$$

Note that the transform of the torque function is evaluated using its implicit time dependence via $T(\phi(t))$.

This expression has a similar form to equation (3.16). However, the non-linearity of $\tilde{T}$ means that it must depend on the initial position ϕ_0. Therefore, any variation in the initial position due to slow changes in the system or apparatus can introduce error into the calculated result.

Viscoelastic Fluid With Variable Transformation

Motivated by the successful linearisation in the viscous case, the same variable transform is applied to equation (3.3), which models the dynamics of the jth flip driven by a non-linear driving torque function in a viscoelastic fluid,

$$\frac{\tau_j(t)}{f(t)} = \alpha\int_{-\infty}^t G_r(t-t_l)\dot{\psi}_j(t_l)\frac{f(t_l)}{f(t)}\,dt_l + \chi\psi_j, \tag{3.30}$$

$$\text{where } f(t) = \frac{T(\phi(t))}{\psi(t)} = \frac{\Psi(\phi_0)}{\Psi'(\phi)}. \tag{3.31}$$

Now it is assumed that the fluid memory function decays much faster than the time of the flip, so that

$$\frac{f(t_l)}{f(t)} \approx 1. \tag{3.32}$$

Note that this condition is exactly met in a viscous fluid which has no 'memory'. Conversely, for an elastic solid the memory function never decays to zero, so this assumption would invariably fail. Making this approximation simplifies the Langevin equation to a normalisable form reminiscent of the linear case,

$$\frac{\tau_j(t)}{f(t)} = \alpha \int_{-\infty}^{t} G_r(t-t_l)\dot{\psi}_j(t_l)\,dt_l + \chi\psi_j. \tag{3.33}$$

Following the same steps of averaging and transforming outlined in section 3.2.2 allows the complex shear modulus to be calculated,

$$G^*(\omega) = \frac{\chi}{\alpha}\frac{i\omega\tilde{\psi}}{1-i\omega\tilde{\psi}}. \tag{3.34}$$

Evidently, this expression of $G^*(\omega)$ is very similar to equation (3.16) where the new normalised position variable ψ has taken over the role of φ. Note that in this case minimising the Brownian motion term involves maximising $f(t)$. Generally this also involves increasing ϕ_0 but the allowed domain is much larger without the Taylor series small angle approximation. Instead the maximum value is only limited by the slow flip time (relative to the fluid memory function) assumption.

3.3 Error Analysis

This section aims to quantify the theoretical relative error of both both the old and new methods of analysis. This can help compare both methods and also determine the optimal initial position which minimises these errors.

3.3.1 Linear Case

Error in Complex Shear Modulus

As outlined in section 3.2.2, maximising the signal to noise ratio involves increasing the initial position. However, since the driving torque function is only approximately linear for small angles, increasing ϕ_0 too much will introduce systematic errors larger than the random error caused by Brownian motion. To quantify these errors $G^*(\omega)$ is calculated directly from the multiple flip average of equation (3.5). To do this, the linear torque and zero mean thermal torque approximations are not imposed, so $T(\phi) \neq \phi$ and $\tau \neq 0$, where τ is the average thermal torque,

$$G^*(\omega) = \frac{\chi}{\alpha}\frac{i\omega}{\phi_0 - i\omega\tilde{\phi}}\left(\tilde{\phi} + \left(\tilde{T} - \tilde{\phi}\right) - \frac{\tilde{\tau}}{\chi}\right). \tag{3.35}$$

Therefore, the absolute relative error in $G^*(\omega)$ can be evaluated by

$$\delta G^*_{Lin} = \left| \frac{\tilde{T} - \tilde{\phi}}{\tilde{\phi}} - \frac{\tilde{\tau}}{\chi \tilde{\phi}} \right|. \tag{3.36}$$

Average Thermal Torque

The average thermal torque defined by

$$\tau(t) = \frac{1}{n} \sum_{j=1}^{n} \tau_j(t) \tag{3.37}$$

only approaches zero as $n \to \infty$. For a finite number of flips the average Brownian motion will still have a thermal torque with standard deviation decaying with $n^{-1/2}$.

Therefore, assuming the thermal torque is white noise, the unilateral Fourier transform of τ should have a constant magnitude that also decays with $n^{-1/2}$. The phase of $\tilde{\tau}$ at each frequency should be random meaning that the expected real and imaginary parts are both zero. Therefore, in calculating the following expected errors, terms proportional to $\tilde{\tau}$ or the real or imaginary parts of $\tilde{\tau}$ can be ignored. So, the expected relative error in the linear case should be

$$\delta G^*_{Lin} = \sqrt{\left| \frac{\tilde{T} - \tilde{\phi}}{\tilde{\phi}} \right|^2 + \left| \frac{\tilde{\tau}}{\chi \tilde{\phi}} \right|^2}. \tag{3.38}$$

High Frequency Error

An expression for the relative error at high frequencies can be found by employing the initial value theorem whereby the unilateral Fourier transform at high frequencies can be asymptotically related to the initial value of the function in the time domain,

$$\tilde{f}(\omega) \sim \frac{f(0)}{i\omega}. \tag{3.39}$$

Applying the initial value theorem as well as the Taylor series of $T(\phi)$ to third order yields

$$\delta G^*_{Lin} = \left| \frac{T_3}{6} \phi_0^2 - \frac{i\omega \tilde{\tau}}{\chi \phi_0} \right| = \sqrt{\left(\frac{T_3}{6} \phi_0^2 \right)^2 + \left(\frac{\omega |\tilde{\tau}|}{\chi \phi_0} \right)^2}. \tag{3.40}$$

Fixing the frequency to ω_0 allows the optimal initial angle for a particular frequency to be found via standard calculus optimisation,

$$\phi_0 = \left(\frac{3\sqrt{2}\, \omega_0 |\tilde{\tau}|}{|T_3| \chi} \right)^{\frac{1}{3}}. \tag{3.41}$$

This particular value of ϕ_0 gives a total relative error of

$$\delta G^*_{Lin} = \sqrt{2\omega^2 + \omega_0^2} \left(\frac{|T_3| |\tilde{\tau}|^2}{12 \chi^2 \omega_0} \right)^{\frac{1}{3}}. \tag{3.42}$$

Notice that this error is proportional to $|\tilde{\tau}|^{2/3}$ meaning that the error decays with the number of flips by $n^{-1/3}$. This means, at least for high frequencies, halving the relative error requires 8 times the number of flips!

3.3.2 Non-linear Case

Error in Complex Shear Modulus

Next we consider the relative error of $G^*(\omega)$ when accounting for a non-linear driving torque, as given by the analysis outlined in section 3.2.3. The error contribution from Brownian motion can be established by including the thermal noise term in equation (3.28). This yields an expression for $G^*(\omega)$,

$$G^*(\omega) = \frac{\chi}{\alpha} \frac{i\omega}{\phi_0 - i\omega\tilde{\phi}} \left(\tilde{T} - \frac{\tilde{\tau}}{\chi} \right), \tag{3.43}$$

with an absolute relative error of

$$\delta G^*_{NLin} = \left| \frac{\tilde{\tau}}{\chi \tilde{T}} \right|. \tag{3.44}$$

Unlike the linear case, Brownian motion is the primary source of error so here the relative error is proportional to $|\tilde{\tau}|$. Hence, the relative error reduces with the number of flips at a faster rate of $n^{-1/2}$.

High Frequency Error

Applying the initial value theorem shows that at high frequencies the minimum error is obtained by maximising the initial driving torque,

$$\delta G^*_{NLin} = \frac{\omega|\tilde{\tau}|}{\chi T(\phi_0)}. \tag{3.45}$$

Low Frequency Error in a Viscous Fluid

From equation (3.17), in a viscous fluid $\tilde{T} = \frac{\phi_0}{k}$ for $\omega = 0$. Therefore, the error is given by

$$\delta G^*_{NLin} = \frac{k|\tilde{\tau}|}{\chi\phi_0}, \tag{3.46}$$

which is minimised by maximising the initial position. These results suggest that an initial position larger than the position which maximises the driving torque should be chosen to reduce error.

3.4 Experimental Results

The accuracy and precision of the new analysis methods were experimentally verified by measuring $G^*(\omega)$ in both viscous and viscoelastic fluids. These measurements were conducted by applying the same methodology as outlined by Zhang *et al.* [2]. Optical tweezers were employed to rotationally trap a spherical vaterite probe particle. The particle rotates between two stable equilibrium angles

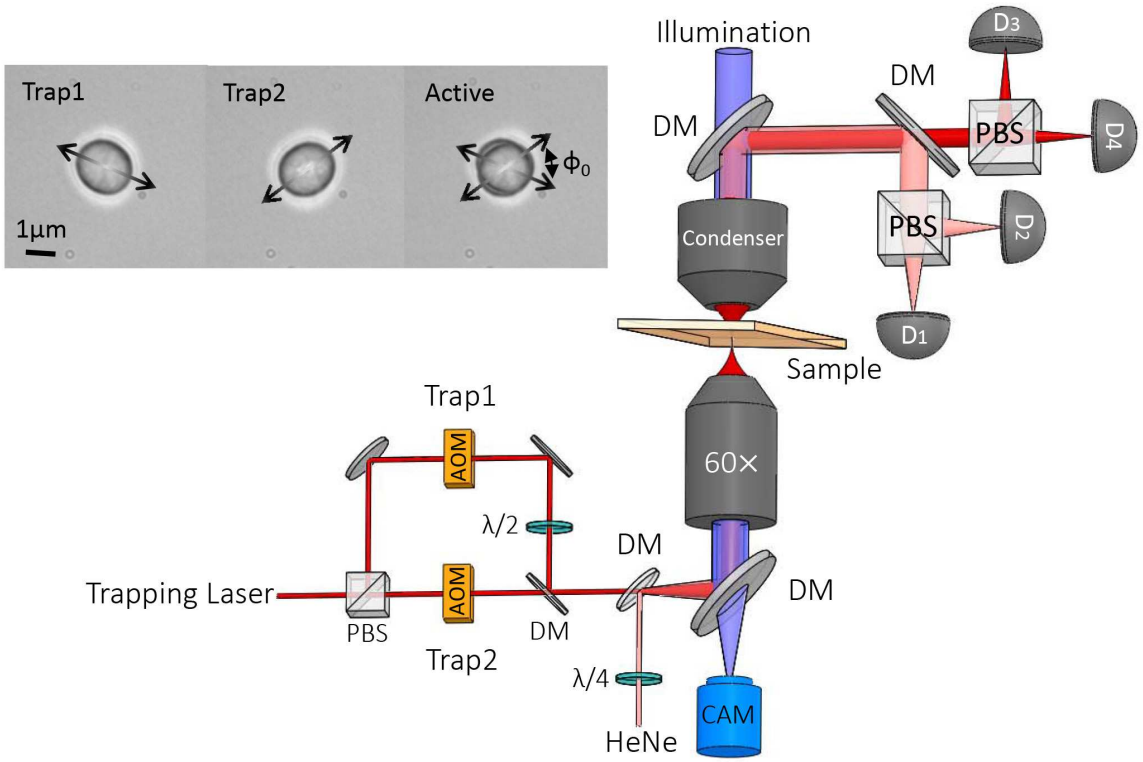

Figure 3.1: The experimental apparatus as illustrated by Zhang *et al.* [2]. The particle is alternately held in two different orientations by two linearly polarised traps. The transient angular displacement is created by means of two AOMs alternately switching on/off every few seconds. DM indicates a dichroic mirror. A camera (CAM) allows imaging of the optical trap.

by alternating between two angularly offset linearly polarised beams controlled electronically by AOMs. Measuring the polarisations of the trapping laser as well as a secondary circularly polarised low-powered HeNe laster gives information about the angular position of the trapped vaterite as well as the optical torque. Figure 3.1 outlines the experimental apparatus used by Zhang *et al.* [2].

In this case, the restoring torque function is sinusoidal $T(\phi) = 1/2\sin(2\phi)$ because of the waveplate nature of the vaterite probe particles. [47] Therefore, the variable transformation is $\Psi = \tan\phi$ and the optimal initial angle should be within $\pi/4 \leq \phi_0 < \pi/2$. For measurements presented here $\phi_0 \approx 70°$, well beyond the linear regime.

3.4.1 Verification of analysis methodology

Measurements were conducted in water, a viscous fluid as well as dilutions (50% and 100% by weight) of Celluvisc (Allergan) eyedrops, a strongly viscoelastic fluid. $G^*(\omega)$ of these Celluvisc dilutions has been previously measured using a macrorheometer and time-temperature superposition by Bennett *et al.* [40]. These values, together with theoretical values of $G^*(\omega) = i\eta\omega$ in a viscous fluid can help establish the accuracy of the three different analysis methods presented in the theory section: analysis assuming a linear torque (section 3.2.2), analysis that accounts for a non-linear torque but at the expense of normalisation (section 3.2.3) and finally analysis that uses a variable transformation to account for the non-linear torque and also allows normalisation (section 3.2.3).

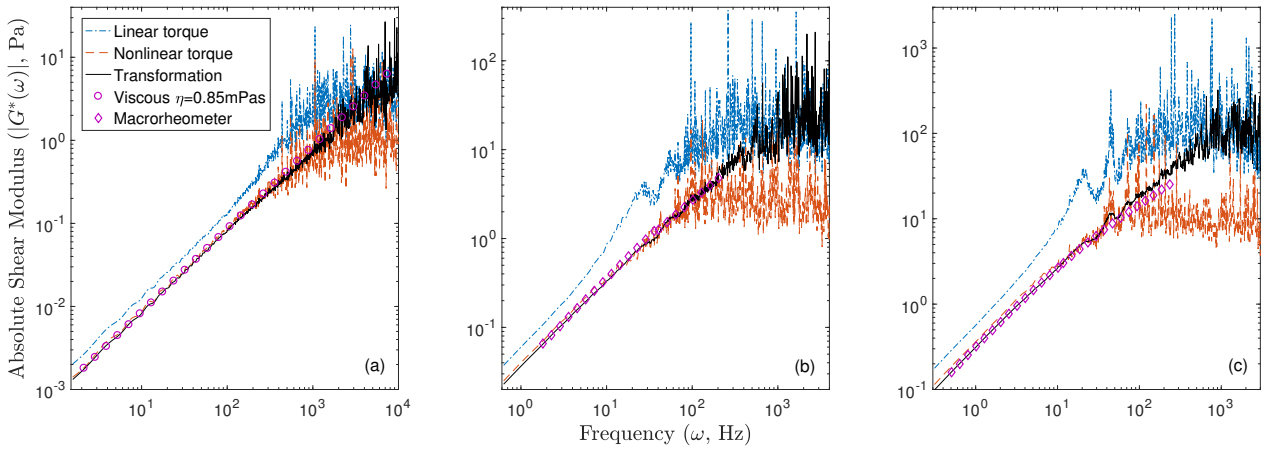

Figure 3.2: A comparison between analysis methods in both viscous water and viscoelastic dilutions of Celluvisc eye drops. (a) depicts results of averaging 222 2s flips in water, (b) 185 5s flips in 50% Celluvisc, and (c) 90 10s flips in 100% Celluvisc. In each graph the blue dashed line is the shear modulus calculated using the old theory which assumes a linear restoring torque. The orange dashed lines are evaluated using the new theory accounting for the non-linear restoring torque outlined in section 3.2.3. The solid black line represents values obtained via the variable transformation analysis described in section 3.2.3, which mitigates error introduced by variation in initial position. All these analysis techniques are compared to either theoretical values (circles) or macrorheological measurements [40] (diamonds).

The results, illustrated in figure 3.2, quite clearly demonstrate the differences in accuracy and precision of the three different analysis methods in all three fluids. The method that assumed a linear torque increased the apparent shear modulus by almost a factor of 2. This is likely because the actual torque at larger angles is much less than supposed when assuming a linear torque function. Hence, the apparent viscoelasticity is larger to compensate.

Both of the other two analysis methods which account for the non-linear torque function produce values of $|G^*(\omega)|$ that have very good agreement with each other and the previous macrorheological measurements. However, the transformation method is more precise and resolves an additional decade before high frequency noise dominates the signal. Interestingly, this good agreement suggests that the flips did decay slowly relative to the fluid memory function validating the the approximation in equation (3.32).

There are concerns about the applicability of particle tracking microrheometers inside slowly changing systems because of the long times required to obtain statistically significant averages [52]. As depicted in figure 3.3, our results demonstrate that this new theory improves the signal of each flip enough to enable precise measurements of $G^*(\omega)$ in sub-minute time scales.

The signal to noise ratio of only a single 5s flip is sufficient to characterise the viscoelasticity at lower frequencies. The presence of absolute random error does, however, affect the elastic measurements more greatly because of its larger relative size. 12 flips greatly reduces random noise allowing precise measurements of both viscosity and elasticity within 1 minute. Spending 10 minutes to average 120 flips does further improve the precision with diminished returns. Therefore, this new theory endows active particle tracking microrheometers with the speed necessary to explore slowly

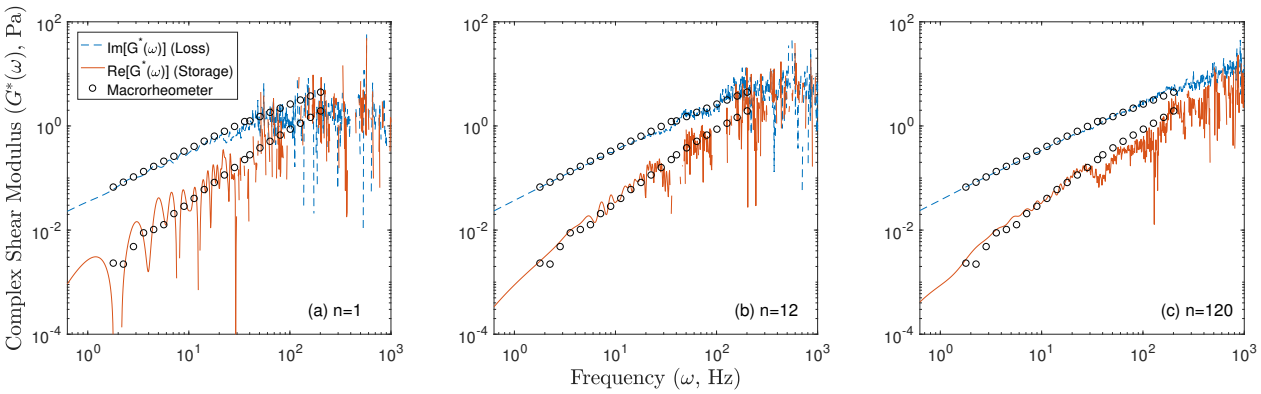

Figure 3.3: The relationship between precision of $G^*(\omega)$ and the number of averaged flips in 50% Celluvisc. (a) shows the viscoelasticity obtained by analysing a single 5s flip with the new method. (b) depicts results from 12 flips during a 1 minute measurement and (c) 120 flips during a 10 minute measurement. All three graphs show good agreement between the microrheological results (lines) and macrorheological data [40] (circles). Evidently, the precision increases with the number of averaged flips, however, because of the large amplitude of each flip, precise results can be obtained within 1 minute.

changing biological systems that were previously inaccessible.

3.4.2 Measurements of tear film

Although not in a slowly changing system, Zhang, *et al.* [2] have demonstrated that the technique is sensitive and accurate enough to provide useful measurements of biological fluids by measuring the viscoelastic properties of eye tear film coated on a contact lens. As the thickness of tear films is only a few microns and reduces over time [77, 78], there have not been any similar studies with conventional methods conducted on this eye fluid on contact lens. Their success in applying the theory is clear evidence of its usefulness and so it is worth presenting a few of their key results.

$G^*(\omega)$ of eye fluid film coated on contact lenses worn by two subjects of the same gender and age was measured at different times of the day (morning, mid-day and afternoon). Each individual set of data was obtained from contact lenses being worn for a few seconds before commencement of the experiment at room temperature. Figure 3.4a illustrates the mean value of the complex shear modulus for each subject at three different times of a day, and the results presented confirm the complex fluid structure of the tear film and show distinct rheological properties of this structure for each subject. Figure 3.4d plots the average of the measurements between the two subjects to show the change in the viscoelasticity of tear film over the day. It appears that values of viscosity in the afternoon were smaller than values measured in the morning across a wide frequency range, and that the elasticity measured in the morning was lower than the values obtained in the afternoon in the low frequency range. Although rigorous characterisation of the properties of tear film in general would require a much larger subject population, these results are sufficient to distinguish between individuals and times of day, demonstrating the applicability of the new analysis and the potential of rotational optical tweezers as an accurate rheological technique to access the properties of fluids in highly confined environments.

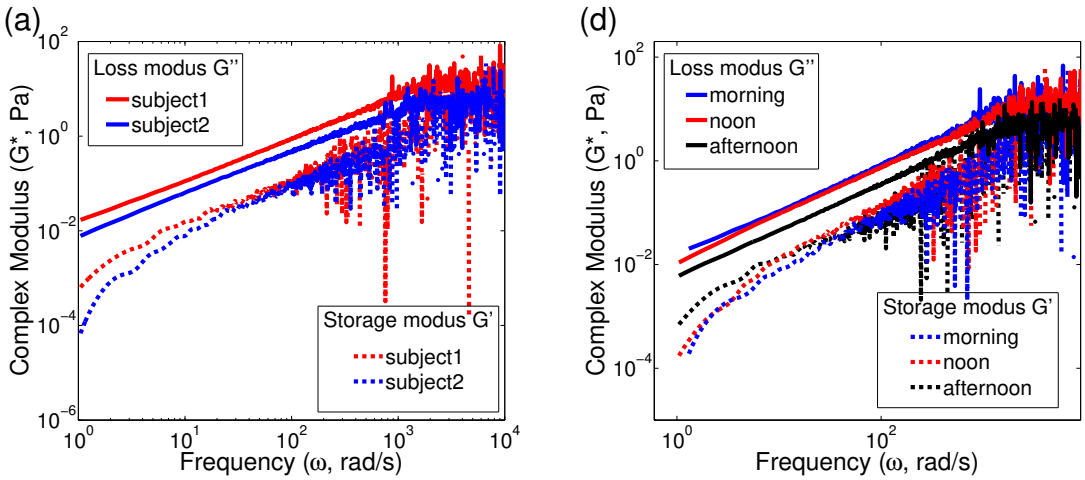

Figure 3.4: Measurenents of complex shear modulii in human tear films. (a) compares $G^*(\omega)$ of tear films of two subjects averaged over three measurements taken at three different times of a day. (d) compares $G^*(\omega)$ at different times of a day by averaging the two subjects' results. In both subfigures the solid lines represent the loss modulus and the dashed lines represent the storage modulus. [2]

3.5 Conclusion

Active microrheology where a probe is impulsively driven switching between two states (two positions for translational microrheology and two orientations for rotational microrheology) can be performed with greatly improved signal to noise ratios by having larger distances or angles between the two positions or orientations. In many cases, such as where optical forces or torques are used to drive the particle, this will be outside the regime where the force or torque can be accurately approximated as a linear spring. This necessitated the development of a more general theory, not assuming linear forces.

We have presented this theory here, and shown the improvements in signal to noise that can be achieved. In addition, for some classes of problems, it is possible to further reduce error by applying a variable transformation (see table B.1) which linearises the equation of motion. This allows normalisation that eliminates error introduced by low frequency drift in the particle's equilibrium position. Our measurements suggest that eliminating error can resolve viscoelasticity at an additional decade for higher frequencies. These improvements in the signal to noise ratio gives a significant reduction in the measurement time for a given error. Thus the method is more conducive to measuring viscoelasticity in slowly changing microscopic systems, such as a living cell.

The following peer reviewed journal article has been adapted for Chapter 4.

[5] **L. J. Gibson**, S. Zhang, A. B. Stilgoe, T. A. Nieminen, and H. Rubinsztein-Dunlop. Machine learning wall effects of eccentric spheres for convenient computation. *Physical Review E*, 99:043304, April 2019.

Contributor	Statement of contribution	%
L. J. Gibson	Conceived the project	20
	Results analysis and interpretation	90
	Wrote the paper	80
	Theoretical and numerical calculation	100
S. Zhang	Conceived the project	10
	Wrote the paper	10
A. B. Stilgoe	Conceived the project	10
T. A. Nieminen	Conceived the project	30
	Results analysis and interpretation	10
	Wrote the paper	5
H. Rubinsztein-Dunlop	Conceived the project	30
	Wrote the paper	5

I am the primary author of this paper, contributing the strong majority of both, analysis of results and theoretical work. The other authors also gave strong contributions to the original conception of the project as well as other minor contributions to the written work.

Chapter 4

Wall Effects of Eccentric Spheres

In confined systems, such as the inside of a biological cell, the outer boundary or wall can affect the dynamics of internal particles. These so-called wall effects were introduced earlier in section 1.2.2. In many cases of interest both the internal particle and outer wall are approximately spherical. Therefore, quantifying the wall effects from an outer spherical boundary on the motion of an internal eccentric sphere is very useful. However, when the two spheres are not concentric, the problem becomes non-trivial. This chapter, based on a paper submitted to *Physical Review E* [5], presents work improving existing analytical methods to evaluate these wall effects. These results are then used to train a feed-forward artificial neural network allowing the wall effects of an outer spherical boundary on the arbitrary motion of an internal sphere for all experimentally achievable configurations to be conveniently and efficiently determined. Furthermore, some experimental results by Zhang *et al.* [4] are presented in section 4.4 to give an indication of how applicable this theory is in real biological systems.

4.1 Introduction

Quantifying effects of boundaries on the dynamics and behaviour of microscopic entities in biological fluids is a problem intersecting several fields of research including microrheology [3], optical tweezers [79] and microbiology [80, 81]. In most scenarios evaluating these so-called wall effects is non-trivial. In cases where the wall effects have been solved analytically, the given expressions are often difficult or inconvenient to evaluate because of their large size or ill-behaviour. Therefore, this chapter aims to make computing the wall effects of eccentric spheres simple by improving various analytical results and training a neural network model to be able to efficiently replicate the analytical results.

Wall effects of eccentric spheres, where an outer spherical boundary affects the dynamics of an internal centre-offset sphere through hydrodynamic interactions, are important in a variety of applications. For example, the intracellular environments of living cells plays an important role in cellular and sub-cellular processes such as replication and intracellular trafficking [21]. Some microrheological techniques rely on the dynamics of spherical probe particles [2, 40], which could be

used to explore properties of the cytoplasm to help understand cellular mechanisms [1].

As mentioned in section 1.1.2, measuring the dynamics of probe particles is a typical approach to determine mechanical properties of complex fluids [82]. To make such measurements, one must not only detect the probe particles but also track their motion in local space. However, in some experiments which work in confined environments, such as inside the cell, the influences of the boundaries the motion of the probe become non-negligible.

This novel approach for accurate cellular rheology requires calibration factors of the hydrodynamic interaction between the probe and near boundary walls. The wall effects of an infinite plane on the translation and rotation of a sphere are well known [61–64] (see section 1.2.2). In cases of more complex systems, the hindered translational diffusion has been studied extensively for spherical particles moving between two plane walls [83]. Furthermore, cylindrical geometries and linear channels were also studied in a few cases, such as measurements of the drag coefficient of a sphere settling along the axis [84, 85]. To our knowledge, no study has evaluated the collective translational and rotational wall effects so that the drag forces acting on a sphere in arbitrary motion could be easily computed.

4.2 Theory

As outlined previously in section 1.2, the wall effects of an outer sphere on an internal sphere can be quantified theoretically by solving the Stokes equations (1.13). From the fluid velocity and pressure the torque and force acting on the internal sphere can be extracted. Comparing these values with the drag forces acting on a sphere in an open fluid reveals the effects of the outer wall on the rotation and translation of the internal particle.

Analytical methods to evaluate these wall effects have been established quite some time ago by Jeffery [62, 86, 87], Stimson [87], Majumdar [88–90] and O'Neill [89, 90]. Summaries of their methods as well as novel improvements will be presented in section 4.2. In section 4.3 these analytically based methods will be used to generate training data for a neural network model to learn to replicate the analytical results.

4.2.1 Problem Construction

Geometry and Bispherical Coordinates

Before evaluating any equations, a suitable coordinate system needs to be chosen to frame the problem. Typically in the case of eccentric spheres, where the sphere centres are offset, bispherical coordinates are the natural choice as they form an orthogonal coordinate system with eccentric spherical coordinate surfaces centred along the z-axis. The bispherical coordinates $(\varepsilon, \theta, \psi)$ to cylindrical coordinates (r, θ, z) transformation is given by

$$r = \frac{c \sin \psi}{\cosh \varepsilon - \cos \psi}, \qquad z = \frac{c \sinh \varepsilon}{\cosh \varepsilon - \cos \psi}, \tag{4.1}$$

where c is a parameter yet to be determined by the positions and radii of the two eccentric spheres. r, θ and z are the standard cylindrical radial, vertical and azimuthal coordinates respectively. From these transformation equations we find that

$$r^2 + (z - c\coth\varepsilon)^2 = (c\,\mathrm{csch}\,\varepsilon)^2, \tag{4.2}$$

demonstrating how the coordinate ε parametrises the radius and z position of the spherical coordinate surfaces by $c\,\mathrm{csch}\,\varepsilon$ and $c\coth\varepsilon$, respectively. Without loss of generality, the inner and outer spherical boundaries are set to reside at $\varepsilon = \alpha$ and $\varepsilon = \beta$, respectively. Figure 4.1 illustrates this configuration. Positioning the spheres along the positive z-axis requires $0 \leqslant \beta < \alpha$ and so the fluid fills the region $\beta < \varepsilon < \alpha$. When $\beta = 0$ the outer sphere becomes an infinite plane at $z = 0$. Fixing the boundary radii (a and b) and their centre offset (χ) determines c by,

$$c = \frac{\sqrt{(a^2 - b^2 + \chi^2)^2 - 4a^2\chi^2}}{2\chi}. \tag{4.3}$$

In the special case of an infinite plane ($b \to \infty$), this equation reduces to,

$$c = \sqrt{d(2a + d)} \tag{4.4}$$

where $d = b - a - \chi$ is the minimum clearance distance between the two boundaries.

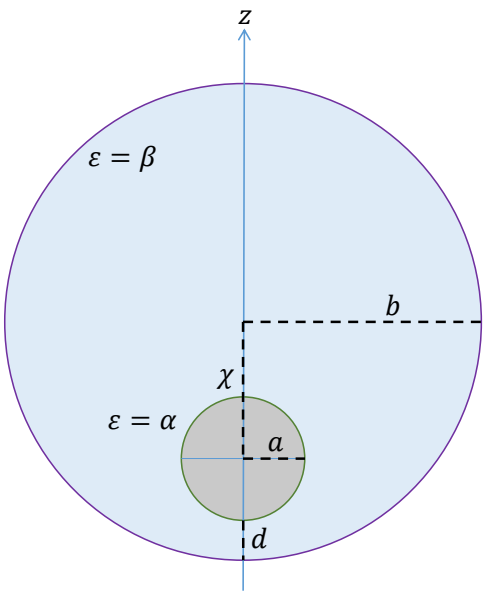

Figure 4.1: Eccentric spheres geometry. The inner sphere, with radius a is offset from the outer spherical boundary by χ along the z-axis (vertical). The minimum clearance distance between boundaries can be related to the radii and vertical offset by $d = b - a - \chi$.

Boundary Conditions

The linearity of the Stokes equations of motion means solutions can be expressed as linear combinations of other solutions. As a result, the problem of modelling arbitrary dynamics of the inner sphere (while

the outer sphere is stationary) can be reduced to only four sub-problems. All kinds of motion from the inner sphere can be expressed as a linear combination of orthogonal rotations and translations. As illustrated in figure 4.2, the symmetry of the spheres allows for four cases: axisymmetric rotation, axisymmetric translation, asymmetric rotation and asymmetric translation. Therefore, the drag forces acting on the inner sphere can always be evaluated as a combination of these four cases.

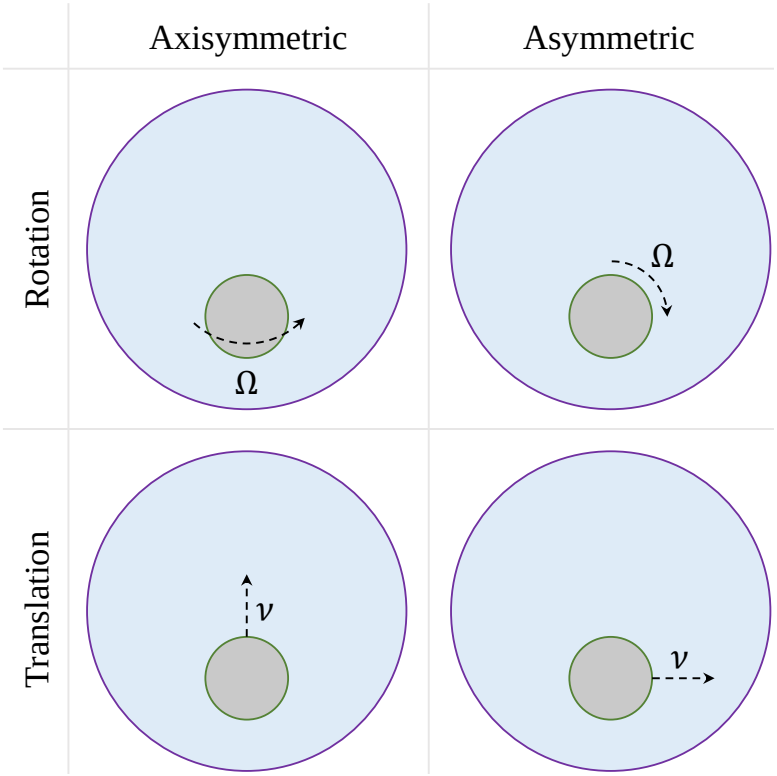

Figure 4.2: The four distinct motions of the inner sphere. The top and bottom rows distinguish rotation and translation. The left and right columns distinguish axisymmetry and asymmetry.

It is assumed that the fluid follows stick boundary conditions whereby the fluid velocity at each boundary matches the corresponding boundary velocity. In all four cases the outer boundary is assumed to be stationary so all velocity components are zero when $\varepsilon = \beta$. The boundary conditions at the inner spherical boundary ($\varepsilon = \alpha$) in cylindrical vector components for axisymmetric and asymmetric rotation respectively are

$$\begin{bmatrix} u \\ v \\ w \end{bmatrix} = \Omega \begin{bmatrix} 0 \\ r \\ 0 \end{bmatrix}, \qquad \begin{bmatrix} u \\ v \\ w \end{bmatrix} = \Omega \begin{bmatrix} (z-z_0)\cos\theta \\ -(z-z_0)\sin\theta \\ -r\cos\theta \end{bmatrix}, \tag{4.5}$$

where Ω is the angular velocity of the inner sphere and $z_0 = c\coth\alpha$. The boundary conditions for axisymmetric and asymmetric translation at the inner sphere are

$$\begin{bmatrix} u \\ v \\ w \end{bmatrix} = V \begin{bmatrix} 0 \\ 0 \\ 1 \end{bmatrix}, \qquad \begin{bmatrix} u \\ v \\ w \end{bmatrix} = V \begin{bmatrix} \cos\theta \\ -\sin\theta \\ 0 \end{bmatrix}, \tag{4.6}$$

where V is the linear velocity of the inner sphere.

Drag Force and Torque

As previously mentioned in section 1.2.1, calculating the drag force and torque acting on the inner sphere involves evaluating the force and torque acting on surface elements of the sphere and then integrating over the whole surface. For a sphere centred on the z axis at z_0, a position vector $\mathbf{r}$ from the centre to the surface can be expressed in cylindrical vector components as

$$\mathbf{r} = \begin{bmatrix} r & 0 & z - z_0 \end{bmatrix}^T. \tag{4.7}$$

Therefore, the surface normal vector $\hat{n}$ (inward with respect to the particle but outward with respect to the fluid) is given by

$$\hat{n} = -\frac{\mathbf{r}}{a}. \tag{4.8}$$

The stress $\mathbf{P}$ acting on a surface element of the particle is the negative dot product of the unit normal vector and the stress tensor. In cylindrical components, the surface force density acting on the particle is

$$\mathbf{P} = -\hat{n} \cdot \sigma = \frac{1}{a} \begin{bmatrix} r\sigma_{rr} + (z - z_0)\sigma_{rz} \\ r\sigma_{r\theta} + (z - z_0)\sigma_{\theta z} \\ r\sigma_{rz} + (z - z_0)\sigma_{zz} \end{bmatrix} \tag{4.9}$$

where σ_{ij} represent the stress tensor components in cylindrical coordinates (see Appendix A).

Therefore, the surface torque density $\mathbf{T}$ acting on the particle is

$$\mathbf{T} = \mathbf{r} \times \mathbf{P} = \begin{bmatrix} -(z - z_0)P_\theta \\ (z - z_0)P_r - rP_z \\ rP_\theta \end{bmatrix} \tag{4.10}$$

where P_r, P_θ and P_z are the cylindrical vector components of $\mathbf{P}$ as shown in equation (4.9).

Evaluating the total force ($\mathbf{F}$) and torque ($\mathbf{G}$) acting on the particle involves integrating the force and torque densities over the whole spherical surface. In bispherical coordinates the surface integrals are

$$\mathbf{F} = \int_0^{2\pi} \int_0^{\pi} \mathbf{P} \frac{c^2 \sin\psi}{(\cosh\alpha - \cos\psi)^2} \, d\psi d\theta \tag{4.11}$$

$$\mathbf{G} = \int_0^{2\pi} \int_0^{\pi} \mathbf{T} \frac{c^2 \sin\psi}{(\cosh\alpha - \cos\psi)^2} \, d\psi d\theta. \tag{4.12}$$

Drag from Arbitrary Motion

As will be explored in subsequent sections, the majority of the force and torque vector components for each kind of motion are zero, and the non-zero components are linear combinations of the particle velocity and rotation components. In general the total force and torque acting on the inner sphere can be described by [60]

$$\mathbf{F} = -\eta(\mathbf{K} \cdot \mathbf{V} + \mathbf{C}^T \cdot \boldsymbol{\Omega}) \tag{4.13}$$

$$\mathbf{G} = -\eta(\mathbf{C} \cdot \mathbf{V} + \mathbf{O} \cdot \boldsymbol{\Omega}) \tag{4.14}$$

where **K** is the translational tensor, **O** is the rotational tensor, and **C** is the coupling tensor which describes the coupling between rotational and translational motions and forces (see section 1.2.1). For eccentric spheres with centres lying on the z axis, these tensors in Cartesian coordinates can be written in terms of dimensionless quantities f_i, g_i, f_i^c and g_i^c:

$$\mathbf{K} = 6\pi a \begin{bmatrix} f_x & 0 & 0 \\ 0 & f_y & 0 \\ 0 & 0 & f_z \end{bmatrix}, \qquad \mathbf{O} = 8\pi a^3 \begin{bmatrix} g_x & 0 & 0 \\ 0 & g_y & 0 \\ 0 & 0 & g_z \end{bmatrix}, \tag{4.15}$$

$$\mathbf{C}^{\mathbf{T}} = 6\pi a^2 \begin{bmatrix} 0 & f_x^c & 0 \\ f_y^c & 0 & 0 \\ 0 & 0 & 0 \end{bmatrix}, \qquad \mathbf{C} = 8\pi a^2 \begin{bmatrix} 0 & g_x^c & 0 \\ g_y^c & 0 & 0 \\ 0 & 0 & 0 \end{bmatrix}. \tag{4.16}$$

When the centres of the eccentric spheres are both positioned on the z axis, then the same asymmetric results can be applied to both the x and y dimensions giving the following relations

$$f_y = f_x, \qquad g_x = g_y, \qquad f_y^c = -f_x^c, \qquad g_x^c = -g_y^c. \tag{4.17}$$

Because of the Lorentz reciprocal theorem, the coupling tensors are related by a transpose [60] so a fifth condition is

$$g_y^c = \frac{3}{4} f_x^c. \tag{4.18}$$

Therefore, for arbitrary translation and rotation in three dimensions the total force and torque vectors can be evaluated from just f_x, f_z, g_y, g_z and f_x^c which will be found from the axisymmetric translation, asymmetric rotation, axisymmetric rotation and asymmetric rotation respectively.

4.2.2 Axisymmetric Rotational Wall Effect

Series Solution

The symmetry of the case where the inner sphere rotates axisymmetrically makes the mathematics comparatively simple. In this case only the rotational fluid velocity component, v, is non-zero and governed by a single equation,

$$\nabla^2 v - \frac{v}{r^2} = 0, \tag{4.19}$$

while $u = w = p = 0$ within the whole domain satisfies both the boundary conditions and equations of motion.

This problem has been previously solved analytically by Jeffery [62] where he used a series solution to solve the equation of motion and evaluate the wall effect. Here we present an outline of a very similar derivation of the wall effect, noting that equation (4.19) has the bispherical series solution [62, 86]

$$v = \sqrt{\cosh\varepsilon - \mu} \sum_{n=1}^{\infty} P_n^1(\mu) \left[A_n \cosh\left(n + \frac{1}{2}\right)\varepsilon + B_n \sinh\left(n + \frac{1}{2}\right)\varepsilon \right], \tag{4.20}$$

where $P_n^1(\mu)$ are associated Legendre functions, $\mu = \cos\psi$, and A_n and B_n are free coefficients.

In this form the total force and torque acting on the particle can be found via the integrals (4.11) and (4.12). The integrals for all vector components vanish except for the z component of the torque (G_z) which is given by the infinite series

$$G_z = 4\pi\sqrt{2}\, c^2\eta \sum_{n=1}^{\infty} n(n+1)(A_n + B_n). \tag{4.21}$$

The dimensionless wall effect g_z is evaluated by dividing this torque by the torque acting on a rotating sphere in a free fluid,

$$g_z = \frac{G_z}{-8\pi\eta\Omega a^3} = -\frac{\sinh^3\alpha}{\Omega c\sqrt{2}} \sum_{n=1}^{\infty} n(n+1)(A_n + B_n). \tag{4.22}$$

Evaluation of Coefficients

Since a general series solution is available, the problem of evaluating the wall effect is reduced to evaluating the series coefficients. The orthogonality of the associated Legendre functions allow the coefficients to be evaluated analytically by enforcing the boundary conditions as outlined in section 4.2.1

$$A_n = 2\sqrt{2}\, c\Omega e^{-(n+\frac{1}{2})\alpha} \frac{\sinh\left(n+\frac{1}{2}\right)\beta}{\sinh(n+\frac{1}{2})(\alpha-\beta)}, \quad B_n = -2\sqrt{2}\, c\Omega e^{-(n+\frac{1}{2})\alpha} \frac{\cosh\left(n+\frac{1}{2}\right)\beta}{\sinh(n+\frac{1}{2})(\alpha-\beta)}. \tag{4.23}$$

Substituting these coefficients into equation (4.22) gives the axisymmetric rotational wall effect in series form

$$g_z = 4\sinh^3\alpha \sum_{n=1}^{\infty} \frac{n(n+1)}{e^{(2n+1)\alpha} - e^{(2n+1)\beta}}. \tag{4.24}$$

Concentric Limit

For high enough number of terms, the series in equation (4.24) converges at a rate of $e^{-2\alpha}$. This means the series converges fastest for large α which occurs when the spheres are close to concentric. In the concentric limit

$$\lim_{\chi\to 0} e^{-\alpha} = \lim_{\chi\to 0} e^{-\beta} = 0, \qquad \lim_{\chi\to 0} e^{\beta-\alpha} = \frac{a}{b} = \lambda. \tag{4.25}$$

Therefore, in the case of concentric spheres all terms in the series vanish except for the first term which gives the well known result

$$\lim_{\chi\to 0} g_z = g_{con} = \frac{1}{1-\lambda^3}. \tag{4.26}$$

Alternative Series Expression

Jeffery [62] also gave an alternative series form of equation (4.24) which converges at a different rate. By expanding the denominator of the summand in equation (4.24) as a geometric series, a double summation can be produced

$$g_z = 4\sinh^3\alpha \sum_{n=1}^{\infty}\sum_{m=0}^{\infty} n(n+1)e^{-(2n+1)(\alpha+m(\alpha-\beta))}. \tag{4.27}$$

Next the summation order is switched and then the sum over n can be simplified into a closed form expression giving the final result as a single (but different) summation

$$g_z = \sum_{m=0}^{\infty} \left(\frac{\sinh \alpha}{\sinh(\alpha + m(\alpha - \beta))} \right)^3. \tag{4.28}$$

The rate of convergence of this second series form is different $e^{-3(\alpha-\beta)}$ which means that in some configurations (such as the infinite plane case with $\beta = 0$) this series converges faster.

Combined Series Form

We have managed to merge these different forms into a new combined sum which converges faster than both

$$g_z = \sum_{m=0}^{M} \left(\frac{\sinh \alpha}{\sinh(\alpha + m(\alpha - \beta))} \right)^3 + 4 \sinh^3 \alpha \sum_{n=1}^{\infty} \frac{n(n+1) e^{-(M+1)(2n+1)(\alpha-\beta)}}{e^{(2n+1)\alpha} - e^{(2n+1)\beta}}. \tag{4.29}$$

The first sum has the same summand as in equation (4.28) but is truncated after the $m = M$ term. The second sum is a modified version of the sum (4.24), except the presence of the additional exponential factor improves the rate of convergence to $e^{-2(M+1)(\alpha-\beta)-2\alpha}$. Essentially, each term present in the first series improves the rate of convergence of the second by a factor of $e^{-2(\alpha-\beta)}$.

Small Clearance Limit

Although Jeffery [62] correctly identified that these axisymmetric rotational wall effects near a plane wall were marginal, he failed to produce any expression for the wall effects in the $d \to 0$ limit. This can be achieved by taking this limit of the summand in equation (4.28) which produces the sum

$$\lim_{d \to 0} g_z = \sum_{m=0}^{\infty} \frac{1}{(m(1-\lambda)+1)^3}. \tag{4.30}$$

The rate of convergence of this sum is quite slow, especially as as λ increases towards 1. Therefore, it might be useful to have approximate closed form expressions for this sum. By taking the Taylor series of the summand in equation (4.30), the series coefficients can be expressed in terms of binomial sums of the Riemann zeta function $\zeta(z)$

$$\lim_{d \to 0} g_z = \sum_{k=0}^{\infty} \lambda^k \frac{(k+1)(k+2)}{2} \sum_{i=0}^{k} \frac{k!}{i!(k-i)!} (-1)^i \zeta(i+3). \tag{4.31}$$

In the infinite plane case ($\lambda = 0$) only the first term remains equalling $\zeta(3) \approx 1.2021$, which agrees with the result given by Cox and Brenner [91]. Interestingly, the increase in drag by the axisymmetric rotational wall effect from an an infinite plane is limited to less than just 20.2%. As will be further explored in later sections, axisymmetric rotation is the only kind of motion where the wall effect does not become singular in the small clearance limit.

A reasonable approximation of the limiting wall effect when $\lambda < 1/3$ can be acheived by taking the first few terms of equation (4.31),

$$g_{\lambda \to 0} = \zeta(3) + 3\lambda[\zeta(3) - \zeta(4)] + 6\lambda^2[\zeta(3) - 2\zeta(4) + \zeta(5)], \tag{4.32}$$

where $\zeta(4) \approx 1.0823$ and $\zeta(5) \approx 1.0369$.

Since the series converges slowest when λ approaches 1, it would seem most useful to find a corresponding Taylor series about $\lambda = 1$. However, applying the same method of expanding the summand in equation (4.30) yields divergent series. Resorting to empirical evaluation, the first few terms seem to be

$$g_{\lambda\to 1} = \frac{1}{2(1-\lambda)} + \frac{1}{2} + \frac{1}{4}(1-\lambda). \tag{4.33}$$

Figure 4.3 compares $g_{\lambda\to 0}$ and $g_{\lambda\to 1}$ showing that their relative errors both tend to zero in their respective limits. If this empirical result is correct then the axisymmetric rotational wall effect is bounded by

$$\frac{1}{1-\lambda^3} \leqslant g_z < g_{\lambda\to 1} < \frac{3}{2}\frac{1}{1-\lambda^3}. \tag{4.34}$$

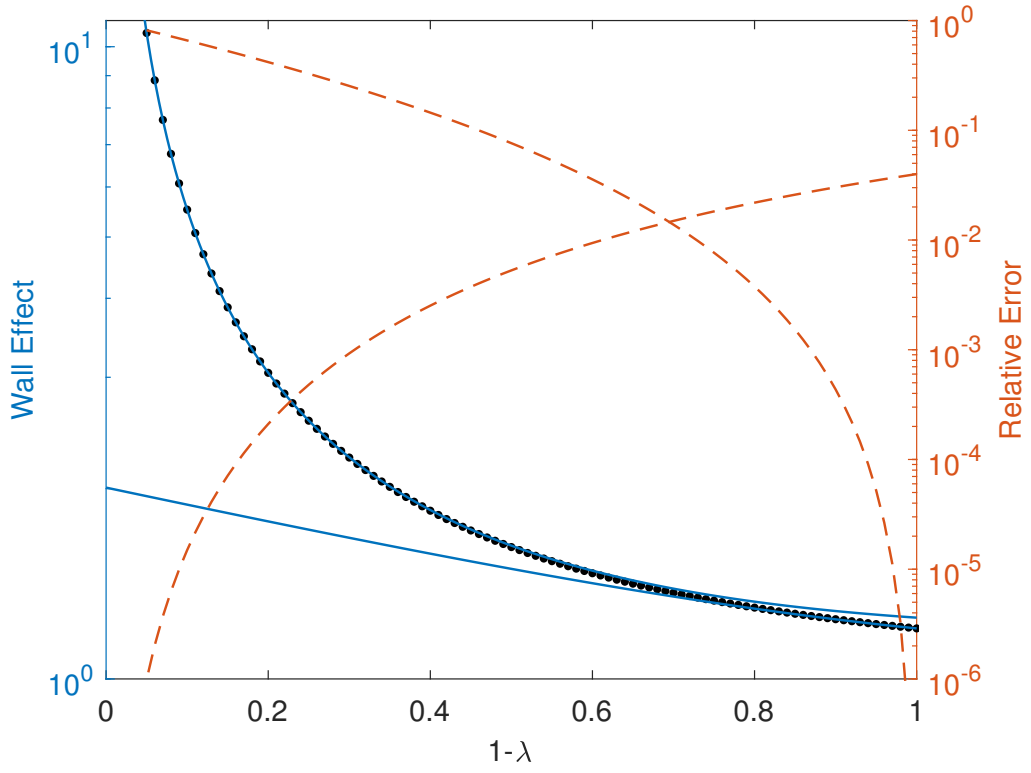

Figure 4.3: A comparison between approximations for the axisymmetric rotational wall effect in the zero clearance limit. The black dots are the true values of the wall effects (calculated using many terms in sum (4.30)) while the solid lines are the $\lambda \to 0$ and $\lambda \to 1$ approximations given by equations (4.32) and (4.33) respectively. The relative errors of these approximations are plotted using the dashed lines and correspond to the right vertical axis.

4.2.3 Axisymmetric Translational Wall Effect

Axisymmetric translational wall effects of different sized spheres moving at the same velocity were first evaluated by Stimson and Jeffery [87]. This section will outline a modified version of their method where only the inner sphere moves along the z axis with velocity v while the outer sphere is stationary.

Stokes' Stream Function

In this case of axisymmetric translation, the vertical and radial velocity components are non-zero while the rotational component is zero. Therefore, Stimson and Jeffery expressed the velocity components in terms of Stokes' stream function Ψ

$$u = \frac{1}{r}\frac{\partial \Psi}{\partial z}, \qquad v = 0, \qquad w = -\frac{1}{r}\frac{\partial \Psi}{\partial r}. \tag{4.35}$$

Noting that all derivatives with respect to θ are zero (because of axisymmetry), they showed from the Stokes equations (1.13) that the stream function must satisfy the linear partial differential equation

$$\Phi^4 \Psi = 0, \tag{4.36}$$

where Φ^2 is the linear differential operator defined by

$$\Phi^2 = r\frac{\partial}{\partial r}\left(\frac{1}{r}\frac{\partial}{\partial r}\right) + \frac{\partial^2}{\partial z^2}, \tag{4.37}$$

thus reducing the problem down to solving a single equation of a single function Ψ.

Series Solution

This equation has a similar series solution in bispherical coordinates to the axisymmetric rotational case shown in section 4.2.2, except there are now four sets of free coefficients A_n, B_n, C_n and D_n (not the same values as before) [86, 87]

$$\Psi = (\cosh\varepsilon - \mu)^{-\frac{1}{2}} \sum_{n=1}^{\infty} (P_{n-1}(\mu) - P_{n+1}(\mu)) \left[A_n \cosh\left(n-\frac{1}{2}\right)\varepsilon + B_n \sinh\left(n-\frac{1}{2}\right)\varepsilon + C_n \cosh\left(n+\frac{3}{2}\right)\varepsilon + D_n \sinh\left(n+\frac{3}{2}\right)\varepsilon\right]. \tag{4.38}$$

Similar to the rotational case, evaluating the integrals given in equations (4.11) and (4.12) for each term in the sum can give the total force and torque acting on the particle. The integrals for all vector components vanish except for the z component of the force (F_z) which is given by the infinite series

$$F_z = \frac{2\pi\eta\sqrt{2}}{c} \sum_{n=1}^{\infty} (2n+1)(A_n + B_n + C_n + D_n). \tag{4.39}$$

The dimensionless wall effect f_z is evaluated by dividing this force by the corresponding force acting on a translating sphere in a free fluid,

$$f_z = \frac{F_z}{-6\pi\eta v a} = -\frac{\sqrt{2}\,\sinh\alpha}{3c^2 v} \sum_{n=1}^{\infty} (2n+1)(A_n + B_n + C_n + D_n). \tag{4.40}$$

Evaluation of Coefficients

The problem of finding the axisymmetric rotational wall effects has now been reduced to evaluating the series coefficients. This is again achieved by enforcing the boundary conditions in equation (4.6).

Since we use different boundary conditions (outer sphere is stationary rather than translating), this is also the point where our calculation differs from Stimson and Jeffery's [87]. The boundary conditions can be expressed in terms of the stream function by

$$\text{at } \varepsilon = \alpha \qquad \frac{\partial \Psi}{\partial z} = 0, \qquad \frac{\partial \Psi}{\partial r} = -r\nu, \tag{4.41}$$

$$\text{at } \varepsilon = \beta \qquad \frac{\partial \Psi}{\partial z} = 0, \qquad \frac{\partial \Psi}{\partial r} = 0. \tag{4.42}$$

Combining the four boundary conditions with the series solution for Ψ given by equation (4.38) and then exploiting the orthogonality of the Legendre polynomials gives a system of simultaneous equations for A_n, B_n, C_n and D_n. For brevity, this system is omitted here but a close version can be seen by equation (26) in [87]. Upon solving the system and substituting back into equation (4.40) yields a rather large expression for the wall effect,

$$f_z = \sinh\alpha \sum_{n=1}^{\infty} \frac{4n(n+1)}{3(2n-1)(2n+3)} \frac{e^{-(2n+1)\beta}(f(\alpha,n) + (4n+2)\sinh 2\alpha) - e^{-(2n+1)\alpha}(f(\beta,n) + (4n+2)\sinh 2\beta)}{4\cosh(2n+1)(\alpha-\beta) - f(\alpha-\beta,n)}, \tag{4.43}$$

where $f(\varepsilon,n) = 4 + (2n+1)^2(\cosh 2\varepsilon - 1)$.

Concentric Limit

Although less obvious from the expression, like the rotational case, all except the first term vanish in the concentric limit. The first term becomes the well known translational wall effect for concentric spheres,

$$\lim_{\chi \to 0} f_z = f_{con} = \frac{4(1-\lambda^5)}{(1-\lambda)^4(4+7\lambda+4\lambda^2)}, \tag{4.44}$$

agreeing with the result found in section 2.4.2.

Small Clearance Limit

Similar to the rotational case, we can try to obtain limiting expressions for the axisymmetric translational wall effect in the small clearance limit. Taking the Taylor series of the summand in equation (4.43) about $d = 0$ suggests $1/d$ dependence for small clearances,

$$\begin{aligned} f_z &= \sum_{n=1}^{\infty} \frac{32n(n+1)}{(2n-1)^2(2n+1)(2n+3)^2} \frac{a}{(1-\lambda)^2 d} + \mathscr{O}(d^0), \\ f_z &= \frac{a}{(1-\lambda)^2 d} + \sum_{n=1}^{\infty} \text{harmonic term} + \mathscr{O}(\sqrt{d}\,). \end{aligned} \tag{4.45}$$

The sum of the $1/d$ term evaluates to a relatively simple closed form. However, the coefficients of the constant term and the following terms of powers of $\sqrt{d}$ form divergent series. Part of the constant term is related to the harmonic series $\sum 1/n$ which suggests the existence of a $\ln d$ singularity. Motivated by the $\sqrt{d}$ powers of later terms, we conjecture that the logarithmic term is proportional to *half* the

coefficient of the harmonic-like series. Therefore, the singular nature of the small clearance limit of axisymmetric translating spheres is conjectured to be

$$\frac{a}{(1-\lambda)^2 d} - \frac{1-7\lambda+\lambda^2}{5(1-\lambda)^3} \ln \frac{d}{a}. \tag{4.46}$$

Note that in the infinite plane case $\lambda = 0$ this agrees with the result given by Cox and Brenner [91]. Figure 4.4 demonstrates the convergence of the axisymmetric translational wall effects after subtracting these conjectured singular terms when $\lambda = 1/4$, 1/5, 1/8 and 0.

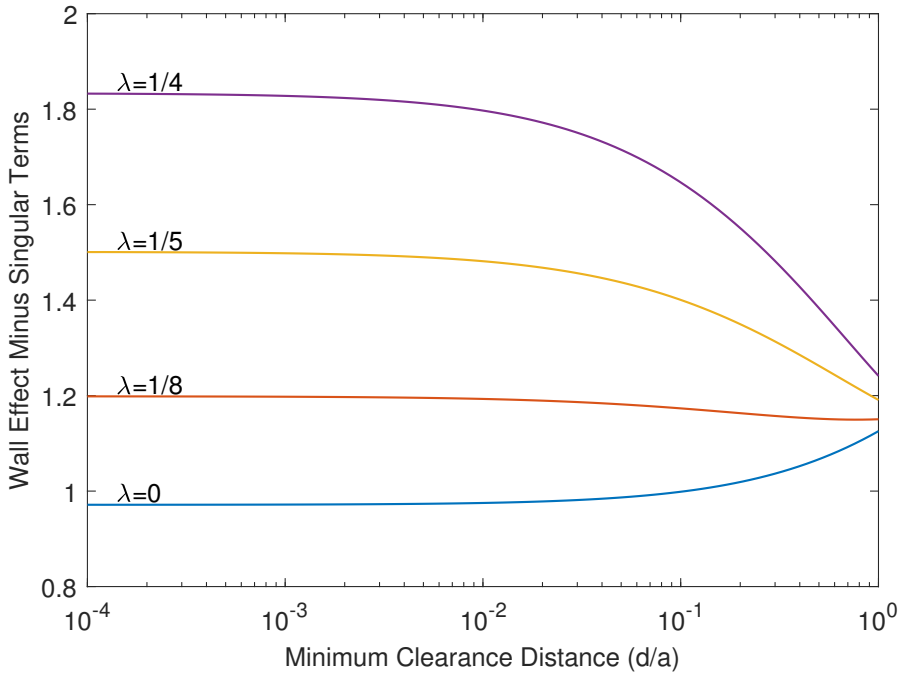

Figure 4.4: Limiting behaviour of axisymmetric translational wall effects. The wall effects (4.43) subtract the conjectured singular terms (4.46) appear to converge towards finite values in the zero clearance limit.

4.2.4 Asymmetric Rotational Wall Effect

The asymmetrical rotational wall effect, where the inner sphere rotates about an axis orthogonal to the line of displacement between the centres of the spheres, was first evaluated by Majumdar [88] and then further refined in collaboration with O'Neill [89]. Similar to the axisymmetric cases, the method here involves finding some series solutions to the equations of motion and then evaluating the coefficients to calculate the wall effects. This section will outline Majumdar and O'Neill's method, and introduce an improved method for evaluating the series coefficients.

Dimensionality Reduced Stokes Equations

Although the rotation of the inner particle is asymmetric, Majumdar was still able to eliminate dependence of the coordinate θ from the Stokes equations in cylindrical coordinates (see Appendix A)

and boundary conditions (4.5) by using the following variable transformation

$$u = 1/2\ \Omega(rQ_1 + cU_2 + cU_0)\cos\theta, \tag{4.47}$$

$$v = 1/2\ \Omega(cU_2 - cU_0)\sin\theta, \tag{4.48}$$

$$w = 1/2\ \Omega(zQ_1 + 2cw_1)\cos\theta, \tag{4.49}$$

$$p = \eta\Omega Q_1\cos\theta, \tag{4.50}$$

where U_0, U_2, w_1 and Q_1 are dimensionless functions independent of θ. The equations of motion reduce to

$$L_0^2 U_0 = L_2^2 U_2 = L_1^2 w_1 = L_1^2 Q_1 = 0, \tag{4.51}$$

where L_m^2 is a class of linear differential operators defined by

$$L_m^2 = \frac{\partial^2}{\partial r^2} + \frac{1}{r}\frac{\partial}{\partial r} - \frac{m^2}{r^2} + \frac{\partial^2}{\partial z^2}, \tag{4.52}$$

and the continuity equation transforms to

$$\left[3 + r\frac{\partial}{\partial r} + z\frac{\partial}{\partial z}\right] Q_1 + c\left[\frac{\partial U_0}{\partial r} + \left(\frac{\partial}{\partial r} + \frac{2}{r}\right) U_2 + 2\frac{\partial w_1}{\partial z}\right] = 0. \tag{4.53}$$

Series Solution

Similar to the axisymmetric cases, the transformed equations of motion (4.51) have series solutions in bispherical coordinates [86, 88, 89]

$$w_1 = (\cosh\varepsilon - \mu)^{1/2} \sum_{n=1}^{\infty} P_n^1(\mu)[A_n \cosh(n+1/2)\varepsilon + B_n \sinh(n+1/2)\varepsilon], \tag{4.54}$$

$$Q_1 = (\cosh\varepsilon - \mu)^{1/2} \sum_{n=1}^{\infty} P_n^1(\mu)[C_n \cosh(n+1/2)\varepsilon + D_n \sinh(n+1/2)\varepsilon], \tag{4.55}$$

$$U_0 = (\cosh\varepsilon - \mu)^{1/2} \sum_{n=0}^{\infty} P_n(\mu)[E_n \cosh(n+1/2)\varepsilon + F_n \sinh(n+1/2)\varepsilon], \tag{4.56}$$

$$U_2 = (\cosh\varepsilon - \mu)^{1/2} \sum_{n=2}^{\infty} P_n^2(\mu)[G_n \cosh(n+1/2)\varepsilon + H_n \sinh(n+1/2)\varepsilon]. \tag{4.57}$$

However, this time there are eight sets of coefficients A_n, B_n, C_n, D_n, E_n, F_n, G_n and H_n.

Using these series solutions, Majumdar and O'Neill [89] managed to relate the wall effects to just the E_n and F_n coefficients by

$$g_y = \frac{\sqrt{2}}{4}\sinh^3\alpha \sum_{n=0}^{\infty} (2n + 1 - \coth\alpha)(E_n + F_n), \tag{4.58}$$

$$f_x^c = \frac{\sqrt{2}}{3}\sinh^2\alpha \sum_{n=0}^{\infty} (E_n + F_n). \tag{4.59}$$

Recursive Coefficient System

The eight sets of coefficients are determined by both the boundary conditions given by equation (4.5) and the continuity equation (4.53). Through these constraints Majumdar [88, 89] and O'Neill [89] were able to express all other coefficients in terms of A_n and B_n, and relate A_n and B_n through two sets of simultaneous recursive equations

$$\mathscr{R}^1 * (A_n, B_n) = i_n, \qquad \mathscr{R}^2 * (A_n, B_n) = j_n \tag{4.60}$$

where $\mathscr{R}^i * (A_n, B_n)$ is defined by

$$\mathscr{R}^i * (A_n, B_n) = a_n^i A_{n-1} + b_n^i B_{n-1} + c_n^i A_n + d_n^i B_n + e_n^i A_{n+1} + f_n^i B_{n+1}. \tag{4.61}$$

For brevity the expressions for $a_n^i - f_n^i$, i_n and j_n are omitted here but are given by Majumdar [88] in equations (39) and (40).

For any given values of α and β, Majumdar and O'Neill [89] solve the system numerically by truncating the system at sufficiently high order and solving the finite system using a Gauss–Seidel method. In the case of eccentric spheres, where one sphere is enclosed by the other, equations (4.60) approach dependence for large n and so the system becomes singular if truncated at too high order. This poses a problem, especially since the most important dominant lower order coefficients are evaluated through backward difference from the point of truncation.

Therefore, for high precision calculations of these coefficients it would seem much better to somehow evaluate A_1 and B_1 and use forward difference to solve subsequent values. In the correspoinding infinite plane problem there is only a single recursive equation which O'Neill and Bhatt [92] and Chaoui [61] solved by transforming A_n into a combination of two other coefficients which are related to A_n by A_1. This allowed them to calculate the transformed coefficients using forward difference and then estimate A_1 by their limiting behaviour.

Motivated by this technique, we transform A_n and B_n into

$$A_n = T_n + A_1 U_n + B_1 V_n, \qquad B_n = W_n + A_1 X_n + B_1 Y_n \tag{4.62}$$

where T_n, U_n, V_n, W_n, X_n and Y_n are new transformed coefficients satisfying

$$T_1 = W_1 = V_1 = X_1 = 0, \qquad U_1 = Y_1 = 1, \tag{4.63}$$

and the following recursive equations

$$\mathscr{R}^1 * (T_n, W_n) = i_n, \qquad \mathscr{R}^1 * (U_n, X_n) = 0, \qquad \mathscr{R}^1 * (V_n, Y_n) = 0, \tag{4.64}$$

$$\mathscr{R}^2 * (T_n, W_n) = j_n, \qquad \mathscr{R}^2 * (U_n, X_n) = 0, \qquad \mathscr{R}^2 * (V_n, Y_n) = 0. \tag{4.65}$$

It is easy to show that this transformation is consistent with the original recursive equations (4.60) except the new coefficients can easily be evaluated using forward differences.

The last step involves evaluating A_1 and B_1, which can be done through the limiting behaviour of the transformed coefficients. In particular, equation (4.62) can be inverted to

$$\begin{aligned} A_1 &= \frac{(W_n - B_n)V_n - (T_n - A_n)Y_n}{U_nY_n - X_nV_n}, \\ B_1 &= \frac{(W_n - B_n)U_n - (T_n - A_n)X_n}{V_nX_n - Y_nU_n}. \end{aligned} \tag{4.66}$$

Assuming the original series solution in equation (4.54) converges, the coefficients A_n and B_n must tend to zero as $n \to \infty$. Therefore, we are motivated to define a sequence of approximate values of A_1 and B_1 as

$$A_1^n = \frac{W_nV_n - T_nY_n}{U_nY_n - X_nV_n}, \qquad B_1^n = \frac{W_nU_n - T_nX_n}{V_nX_n - Y_nU_n}, \tag{4.67}$$

which should satisfy

$$\lim_{n\to\infty} A_1^n = A_1, \qquad \lim_{n\to\infty} B_1^n = B_1, \tag{4.68}$$

if W_n and T_n do not converge to 0. In practice we find that this is the case and that A_1^n and B_1^n converge like

$$A_1^n - A_1^{n-1} \propto B_1^n - B_1^{n-1} \propto ne^{-2\beta n}. \tag{4.69}$$

This limiting behaviour can be extrapolated to infinity to improve the approximation for finite orders

$$\begin{aligned} A_1 &\approx A_1^n + (A_1^n - A_1^{n-1})e^{-2\beta}\frac{1 + n(1 - e^{-2\beta})}{n(1 - e^{-2\beta})^2}, \\ B_1 &\approx B_1^n + (B_1^n - B_1^{n-1})e^{-2\beta}\frac{1 + n(1 - e^{-2\beta})}{n(1 - e^{-2\beta})^2}. \end{aligned} \tag{4.70}$$

Therefore, using equation (4.70) to calculate A_1 and B_1, equation (4.62) can be used to evaluate A_n and B_n.

Small Clearance Limit

Expressions for the singular terms of the asymmetrical wall effects are given by O'Neill and Majumdar [90]

$$g_y = -\frac{2}{5}\frac{1}{1-\lambda}\ln\frac{d}{a} + \ldots, \tag{4.71}$$

$$f_x = -\frac{4}{15}\frac{2 - \lambda + 2\lambda^2}{(1-\lambda)^3}\ln\frac{d}{a} + \ldots, \tag{4.72}$$

$$f_x^c = -\frac{2}{15}\frac{4\lambda - 1}{(1-\lambda)^2}\ln\frac{d}{a} + \ldots. \tag{4.73}$$

4.2.5 Asymmetric Translational Wall Effect

The asymmetric translational wall effects are evaluated almost identically to the preceding asymmetric rotational wall effects with only a few minor differences. The equations of motion are again reduced to

equation (4.51) by applying the same variable transformation as equations (4.47)–(4.50) except with the replacement $\Omega \to v/c$. The same series solutions are utilised except the coefficients' values are different. The dimensionless force is given by

$$f_x = \frac{\sqrt{2}}{3} \sinh \alpha \sum_{n=0}^{\infty} (E_n + F_n). \tag{4.74}$$

The expressions for i_n and j_n are different in the translation case because the boundary conditions are different. However, with the exception of this difference, the coefficients A_n and B_n can be evaluated the same way as in the rotational case.

4.3 Machine Learning

The analytical solutions for the wall effects presented here are all in infinite series form, most of which present quite large expressions which are tedious to practically evaluate on a computer. The convergence of these series depend on d/a and a/b and for highly eccentric configurations can be quite slow, requiring hundreds of terms and high precision computation to be evaluated numerically. Therefore, it is useful to have a well established model that can replicate the wall effects much more efficiently and conveniently. By the universal approximation theorem [93], a finite artificial neural network should be able to model these wall effects arbitrarily well. This section outlines the training and performance of such a model using data evaluated from the series solutions.

4.3.1 Multilayer Perceptron

A relatively simple machine learning model is the multilayer perceptron (MLP), which is a kind of artificial feed forward neural network. In a MLP the initial inputs enter the network as a set of neurons called the input layer. The information then passes through hidden layers of neurons which then connect to the final output layer. This kind of structure precludes any loops in the network. Figure 4.5 illustrates the structure of feed forward networks.

4.3.2 Model

The model should be able to compute the five dimensionless wall effects f_x, f_z, g_y, g_z and f_x^c from d/a and $\lambda = a/b$ over as large a domain as possible. Of greatest importance, is the ability to evaluate the full dependence on the minimum clearance distance (d) for fixed radii $0 < d \leqslant b - a$, as well as the transition behaviour between an infinite plane boundary ($\lambda = 0$) and a finite spherical wall.

Model Representation

In the small clearance limit ($d/a \to 0$) all of the wall effects (except g_z) become singular. Similarly, as the two spheres approach the same radii ($\lambda \to 1$) all five effects also tend to infinity. The singular nature of the wall effects can be directly incorporated into the model since analytical expressions

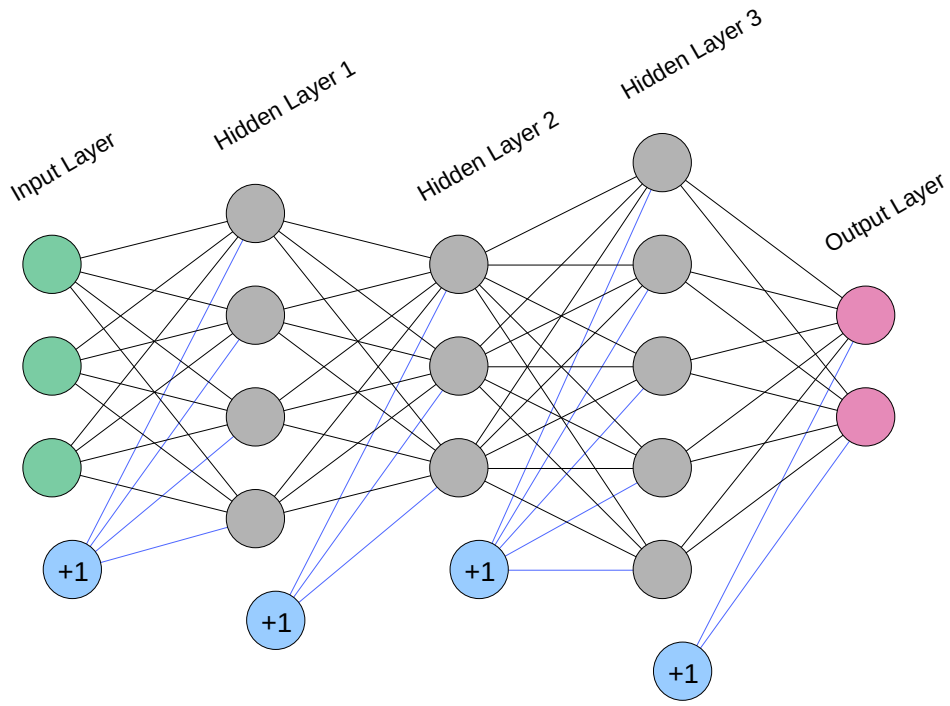

Figure 4.5: An example of an MLP. Three inputs (green) pass through hidden layers (grey) to two outputs (red) at the output layer. Each layer, except the output layer, contains a single bias neurons (blue) which retains a constant value. This example is a deep network because it contains multiple hidden layers and can sometimes identify non-linear trends more easily.

for the singular terms in both limits are known. Therefore, the neural network needs only learn the non-singular behaviour of the wall effects. The model ($\mathscr{W}$) is, therefore, comprised of the network ($\mathscr{N}$) which is then scaled by the concentric wall effects ($\mathscr{C}$), which accounts for the $\lambda \to 1$ singularities, and added to modified low clearance singular terms ($\mathscr{S}$), which accounts for the $d/a \to 0$ singularities,

$$\mathscr{W}(d/a,\lambda) = \mathscr{N}(\mathbf{x}) \circ \mathscr{C} + \frac{\mathscr{S}}{1+(d/a)^2}. \tag{4.75}$$

$\mathscr{W}$ is a vector of the dimensionless wall effects

$$\mathscr{W} = \begin{bmatrix} g_y & f_x^c & f_x & f_z & g_z \end{bmatrix}^T, \tag{4.76}$$

$\mathscr{C}$ represents a vector of the concentric wall effects given by equations (4.26) and (4.44)

$$\mathscr{C} = \begin{bmatrix} g_{con} & f_{con} & f_{con} & f_{con} & g_{con} \end{bmatrix}^T, \tag{4.77}$$

$\circ$ represents the Hadamard product (element-wise multiplication) between $\mathscr{C}$ and $\mathscr{N}(\mathbf{x})$ (which is the neural network output) and $\mathscr{S}$ denotes a vector containing the corresponding singular terms given by equations (4.71), (4.73), (4.72) and (4.46) respectively, and 0 for the corresponding g_z component. In the model this singular part is scaled down by $1+(d/a)^2$ so that the logarithmic terms do not diverge for large d/a. This is especially important for small λ where the domain includes large values of d/a.

Artificial Neural Network

The final network chosen is a fully connected feed forward network with 2 inputs, 5 outputs and 50 nodes in the hidden layer. The network structure should be chosen to balance computation time with performance. We found that the network performance increased with the number hidden units, while remaining mostly invariant with the number of hidden layers. 50 nodes in a single hidden layer seemed to be enough to accurately fit the data while still being able to quickly compute the output. The inputs are normalised between -1 and 1 by

$$\mathbf{x} = \begin{bmatrix} \frac{d/a-1}{d/a+1} & 2\lambda - 1 \end{bmatrix}^T. \tag{4.78}$$

The hidden layer utilises a sigmoidal activation function defined by

$$\sigma(x) = \frac{2}{1+e^{-2x}} - 1, \tag{4.79}$$

while the output layer's activation function is linear.

Mathematically, the network is computed by

$$\mathscr{N}(\mathbf{x}) = B2 + W2 \times \sigma(B1 + W1 \times \mathbf{x}), \tag{4.80}$$

where $B1$ and $B2$ are column vectors containing the biases of each layer, $W1$ and $W2$ are matrices containing the weights of each layer, $\times$ represents matrix multiplication and σ is applied component-wise. For reference, table B.2 tabulates the trained values of these biases and weights to 8 significant figures.

4.3.3 Data Evaluation and Network Training

To train the network, training data was generated from the analytical results. g_z and f_z were calculated using equations (4.29) and (4.43). g_y, f_x^c and f_x were calculated using equations (4.58), (4.59) and (4.74) with coefficients evaluated using section 4.2.4 methods. The truncation condition for each series was when the relative change in the finite sum by adding at least 10% more terms was less than the desired precision (10^{-16}). The series expressions were evaluated using Mathematica software using a precision of 220. For most cases, this precision was much higher than necessary. However, to satisfy the truncation condition when d/a was close to zero required hundreds of terms in the series, and using such a high precision was required when computing the asymmetric wall effects.

The training and validation data formed a random 70% and 30% split over a uniform 101×91 grid of $\frac{d}{b-a} \times \lambda$ over the domain

$$0.001 \leqslant \frac{d}{b-a} \leqslant 0.999, \qquad 0.05 \leqslant \lambda \leqslant 0.95, \tag{4.81}$$

while an additional 2000 random points across the same domain formed the testing data. The network was trained in MATLAB using Levenberg–Marquardt backpropagation (trainlm) until the mean-squared error of the validation data stopped decreasing for 100 epochs.

4.3.4 Model Error

After training the network, the performance of the full model, given by equation (4.75), over the training domain, equation (4.81), can be quantified by the relative error between the model output and the training and validation data.

Training Region Performance

Histograms of the relative errors are plotted in figure 4.6. These demonstrate two sets of behaviours with the model errors. The non-coupling wall effects f_x, f_z, g_y and g_z all exhibit similar relative errors, probably because they are all defined such that they are bounded by $\geqslant 1$. The coupling effect f_x^c, however, tends to zero in the concentric limit and also decreases in magnitude in the $\lambda \to 0$ limit. Therefore, the relative error in f_x^c diverges, even for small absolute errors.

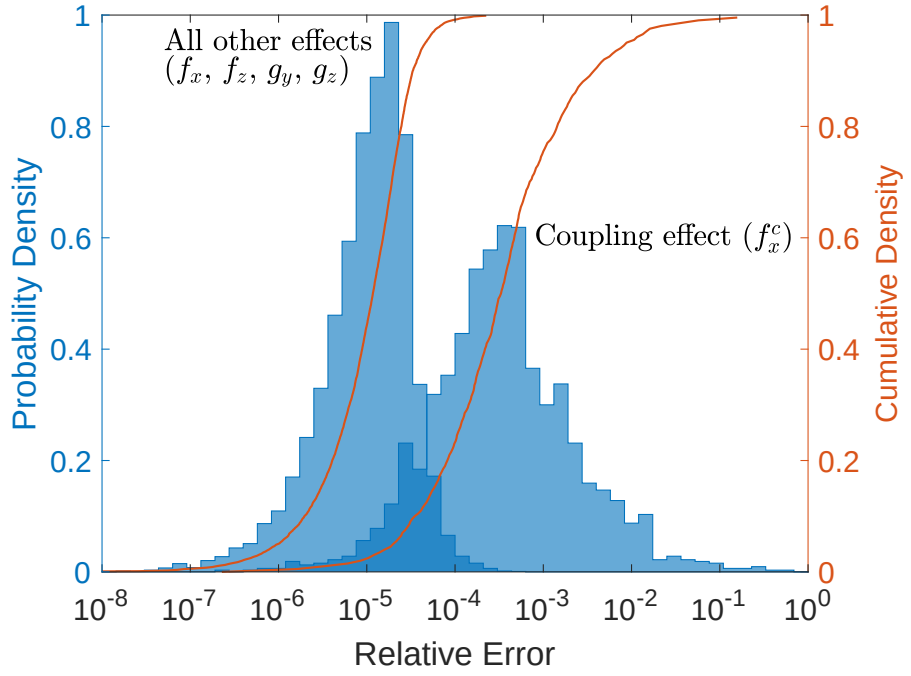

Figure 4.6: Histograms of the relative error between model outputs and testing data. The coupling wall effect f_x^c is kept separate because of its larger relative errors. The solid red lines represent the cumulative densities showing the proportion of points less than the given relative error.

In practice, large relative errors in coupling are less important when the other wall effects are much more significant. Figure 4.7 plots the ratio of the coupling wall effect f_x^c with the corresponding asymmetrical translational wall effect f_x. The ratio tends to zero in the concentric limit and becomes smaller over a larger region as the outer sphere radius grows $\lambda \to 0$. This demonstrates that the regions with higher relative error in the coupling wall effect, are the same regions where any wall effect from asymmetric translation or rotation would dominate.

Separating the coupling wall effect from the rest, the median relative error over the domain of training and validation data is 1.2×10^{-5} and the maximum value is 5.1×10^{-4}. The median relative error of f_x^c is 3.5×10^{-4}.

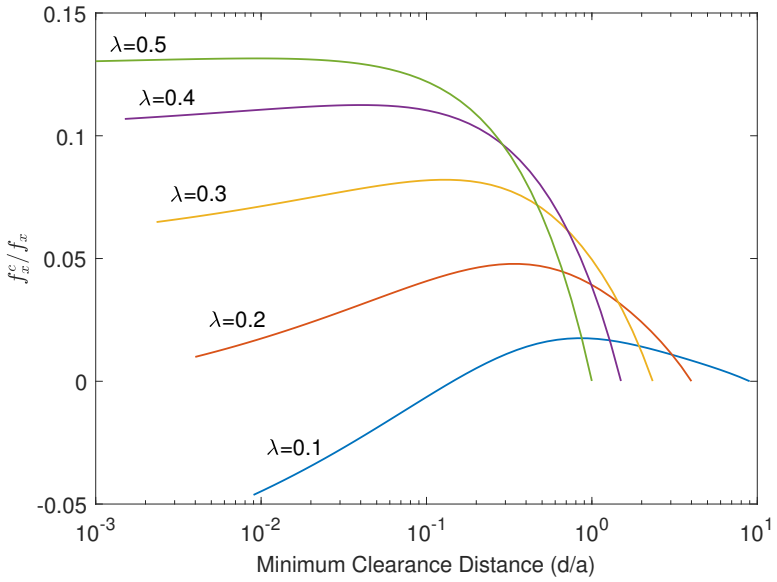

Figure 4.7: The ratio of the asymmetric rotation-translation coupling force and the asymmetric translation is very small. It approaches zero in the concentric limit and decreases as λ decreases.

Within the training domain, the model serves as an efficient system to interpolate between grid points, so it is worth comparing its performance to other interpolation techniques that use a comparable number of parameters. The network contains 405 weights and biases so choosing every tenth point in each dimension of the 101×91 grid gives 110 points for each of the 5 wall effects. This results in a total of 550 parameters, just a little more than the network. The model performs worse when applying linear or cubic interpolations over this grid instead of the network. Figure 4.8 is a quantile–quantile (Q–Q) plot comparing the error distributions of the network performance (as shown in figure 4.6) with corresponding error distributions when applying linear and cubic interpolations. Evidently the network outperforms both forms of interpolation.

Infinite Plan Extrapolation

One of the goals of the model is to be able to model the transition behaviour between the eccentric sphere wall effects and the infinite plane wall effects. To test this, we check the relative error of the model when $\lambda = 0$. The axisymmetric wall effects g_z and f_z could be evaluated using the same expressions but with $\beta = 0$. The method for evaluating the asymmetric series coefficients becomes untenable in the infinite plane limit, so the approximations from Chaoui and Feuillebois [61] for the asymmetric infinite plane wall effects were used instead.

Figure 4.9 plots the relative errors of the model outputs as a function of d/a. Although the network was not trained on infinite plane wall effects, it did successfully reproduce them with a median relative error from non-coupling values of 4.6×10^{-4} and maximum 1.7×10^{-2}, and a median coupling relative error of f_x^c 1.1×10^{-1}. Although the relative error in coupling is comparatively large, this only occurs when the effect tends to zero and is marginal compared to the other wall effects. When $d/a < 0.2$ the coupling effect becomes more significant but the model successfully evaluates it to less than 0.3% error.

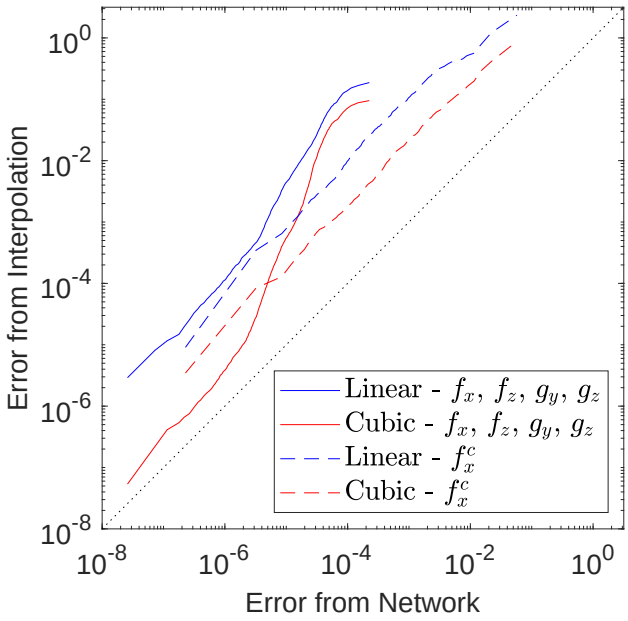

Figure 4.8: A Q–Q plot comparing the performance of the model on the testing data when using the network and when using interpolation. The blue lines represent distributions of errors from linear interpolations over 11×10 grids of $\frac{d}{b-a} \times \lambda$. The red lines are corresponding results from cubic interpolations. The network outperforms the interpolation methods in all cases.

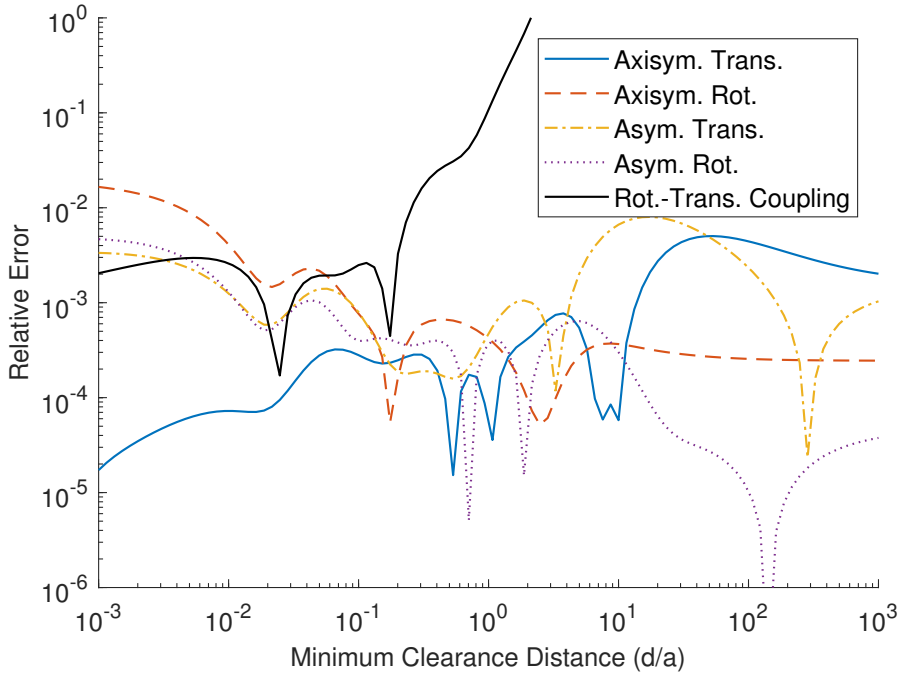

Figure 4.9: The relative error of the model when extrapolating from the training region to calculate infinite plane wall effects ($\lambda = 0$).

4.4 Comparison With Experiment

The cytoplasm of living cells is a crowded yet dynamic environment [94, 95]. So to investigate wall effects and the effectiveness of rotational particle tracking microrheology inside cells, Zhang *et al.* [4] replaced the real cell with artificial unilamellar lipid vesicles, known as liposomes, to serve as a simple model of a cell. The Liposomes were prepared following a protocol described in Yamada *et*

al. [96] that was modified so that the liposomes encapsulated vaterite particles. Zhang *et al.* present direct measurements of constrained rotational motion of optically spun particles inside the liposomes and show how the rotational motion changes close to the membrane. These results provide a good opportunity to establish how applicable the theoretical wall effects of eccentric spheres are in a real optical tweezers experiment.

All measurements were made using the same optical tweezers system as mentioned in chapters 3 and 5. To measure the asymmetrical rotational wall effects of the membrane on the eccentric probe sphere, the optically trapped particles were moved from the center of their respective liposome towards the side of the lipid membrane by moving the motorized stage in 200nm increments. The rotation rate of the particle (Ω) was measured at each position as a function of distance from the liposome membrane using the same laser power. While maintaining the same optical torque, the wall effect is given by the ratio of the angular velocity in a free fluid (Ω_0) to the angular velocity in the presence of the liposome.

Figure 4.10 compares the experimental wall effects of particles with radii of 1.1μm, 0.85μm and 0.6μm with the theoretical asymmetric rotational wall effects output by the network model for $1/4 \leqslant \lambda \leqslant 1/3$. The experimental results clearly demonstrate the existence of wall effects and good agreement with theory within the experimental errors, which are reasonably high due to the non-spherical and slowly changing shape of vesicles, and imaging aberrations. It is possible that the theory over estimates the wall effects when the particle is almost touching the membrane since the membrane can stretch, but for the most part, the theory is more than adequate to constrain the wall effect errors below the others.

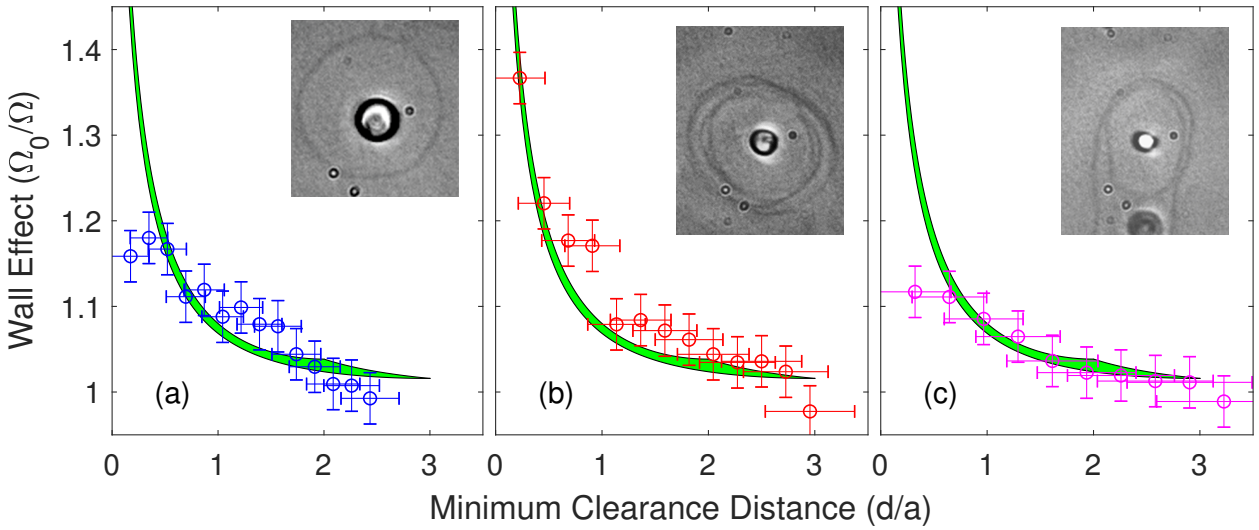

Figure 4.10: Experimental measurements by Zhang *et al.* [4] (circles) of asymmetric rotational wall effects on three separate optically trapped particles inside artificial vesicles. The particles imaged in (a), (b) and (c) have radii of 1.1μm, 0.85μm and 0.6μm respectively. The results are consistent with the theoretical wall effects output by the network for $1/4 \leqslant \lambda \leqslant 1/3$ (shaded green), except possibly when d/a is less than about 0.2.

4.5 Conclusion

Analytical methods for calculating the wall effects of eccentrically positioned spheres have been improved and high precision evaluation of these effects over a discrete domain was able to generate data that could be used to train an artificial neural network to model the dimensionless forces and torques acting on the inner sphere. Within the training domain the model performed excellently with relative errors generally around 0.001% error. The model successfully extrapolated to model the wall effects of an infinite plane on a sphere to less than 2% error but generally around 0.05%. The success of the trained model using a relatively small network means that arbitrary motion of a sphere moving within another sphere can be efficiently modelled using easy-to-implement code. Zhang's *et al.* [4] results are a good example how the model can be applicable in real optical tweezers experiments.

The following publication has been heavily modified and adapted for Chapter 5.

[3] S. Zhang, **L. J. Gibson**, A. B. Stilgoe, T. A. Nieminen, and H. Rubinsztein-Dunlop. Impact of complex surfaces on biomicrorheological measurements using optical tweezers. *Lab on a Chip*, 18:315–322, 2018.

Contributor	Statement of contribution	%
L. J. Gibson	Conceived the project	10
	Performed experiments	10
	Results analysis and interpretation	50
	Wrote the paper	20
	Theoretical and numerical calculation	90
S. Zhang	Conceived the project	10
	Performed experiments	90
	Results analysis and interpretation	50
	Wrote the paper	50
A. B. Stilgoe	Conceived the project	20
	Wrote the paper	10
T. A. Nieminen	Conceived the project	30
	Wrote the paper	10
	Theoretical and numerical calculation	10
H. Rubinsztein-Dunlop	Conceived the project	30
	Wrote the paper	10

Shu Zhang is the primary contributor to the original paper, while I am the secondary. She contributed about half of the written work and performed most of the experimental work. I performed most of the theoretical work and calculations while we have equal shares in the analysis and interpretation. The other authors also gave strong contributions to the original conception of the project as well as other minor contributions to the written work. The version of the paper included in this chapter has been heavily modified to make it fit within the theme of this dissertation and to emphasise the theoretical component. The table above describes the contributions of each author to the original paper. I estimate the following changes to the author contributions for the version included in this chapter.

Contributor	Statement of contribution	%
L. J. Gibson	Results analysis and interpretation	70
	Wrote the paper	60
S. Zhang	Results analysis and interpretation	30
	Wrote the paper	25
A. B. Stilgoe	Wrote the paper	5
T. A. Nieminen	Wrote the paper	5
H. Rubinsztein-Dunlop	Wrote the paper	5

Chapter 5

Wall Effects of Cylinders

Chapter 4 outlined how to calculate wall effects of spherical boundaries and explored their applicability when applying optical tweezers in biological systems where boundaries can be flexible. This chapter, based on the published work of Zhang *et al.* [2], investigates the wall effects of cylinders on the rotation of spheres, as might be more applicable when applying optical tweezers in microfluidic systems where boundaries are solid. Experimental measurements of the drag torque on optically trapped rotating particles moving near three-dimensionally (3D) printed conical and cylindrical walls agree well with theoretical predictions. These results are essential for quantifying how curved walls can affect the torque on particles, and thus enable accurate hydrodynamic measurements and simulations at the micron-scale.

5.1 Introduction

Understanding and controlling the motion of particles at the micrometre scale is crucial to study hydrodynamic processes in cell biology and related microfluidic systems. Optical tweezers is one of most common force spectroscopy techniques that can resolve pN forces and nm displacements with high temporal resolution down to μs. It has been extensively developed and used as an invaluable tool for a variety of fundamental and practical applications in physics, chemistry, and biology. [13,14,35,97] Additionally, torque or force is used as a physical parameter to directly study biological objects such as single DNA molecules, bacteria and sperm due to their torsional properties. [15,98] However, in biological processes, such measurements are frequently performed in confined environments where the influence of boundaries on the motion of the probe becomes non-negligible.

The dynamics of a rigid particle suspended in a fluid are typically dependent upon three key factors: the geometry of the probe particle and surrounding boundaries, external forces or torques applied to the particle and properties of the medium. [30,99] Studying hydrodynamic interactions between the particle and near walls, known as wall effects (see section 1.2.2), is also essential for studying microrheological properties of complex biological systems such as cytoplasm. Hence, to quantify these effects and attain proper measurements, novel detection tools require simultaneous measurement

of force or torque together with valuable calibrations of wall effects on the probe.

Classical microfluidic devices have been used in previous experiments to quantify both translational and rotational wall effects of a plane wall on a sphere [64, 100] (see section 1.2.2). There is ever-expanding literature on wall effects within complex systems where particles are confined in more than one dimension and/or curved walls, in order to model biological entities and microchannels for microfluidic devices. [83–85, 101] However, to date, the wall effects of curved boundaries on a rotating particle have not been clearly established.

In recent years, three-dimensional (3D) printing techniques have opened new opportunities to fabricate complex 3D objects on demand. [102, 103] We 3D printed ultra-high resolution curved and cylindrical microwalls with a structure determined by the shape of the optical trapping beam. We experimentally measured wall effects of a rotating birefringent spherical particle trapped in a fluid near non-planar microwalls by using optical tweezers. Here we will only consider the case of simple Newtonian fluids. Knowing wall effects for a simple Newtonian fluid is an essential baseline to study more complex fluids such as solutions of RNA, DNA and protein etc. If Newtonian wall effects are known then non-Newtonian effects can be recognised and quantified. Overall, these results provide the technical basis of calibrating optical torque for studying the nonequilibrium nature of biological objects in confined geometries.

5.2 Material and Methods

5.2.1 3D-Printed Wall Design

We printed microwalls on a cover slip using a commercially available 3D direct laser writing setup (Nanoscribe GmbH) with resolution down to 150 nm based on two-photon polymerisation (2PP) technology. A scanning electron microscope image of printed walls can be seen in figure 5.1(c). Optical tweezers is usually formed by tightly focusing a beam through a high numerical aperture microscope objective. As such, to identify an appropriate structure for the walls, we consider an inclined wall rather than a perpendicular structure so that the laser distortion by the wall is minimised. The geometry of the wall is illustrated in figure 5.1. The angle of inclination is determined by the numerical aperture (NA) of the microscope objective and set to be 70°. The hollow microwall has a height of 4 μm in the region where the particle is trapped.

5.2.2 Measurement of Wall Effect

After optimising the design and printing procedure, rotating particles were optically manipulated near microwalls. The sample was placed on the stage of the inverted microscope for optical manipulation and observation. The boundary wall mounted on the sample chamber (figure 5.2 inset) was brought close to the particle by translating the stage (Mad City Labs) in XYZ with nanometer precision. The optical trapping system used here has been described in detail elsewhere [2]. In brief, as shown in figure

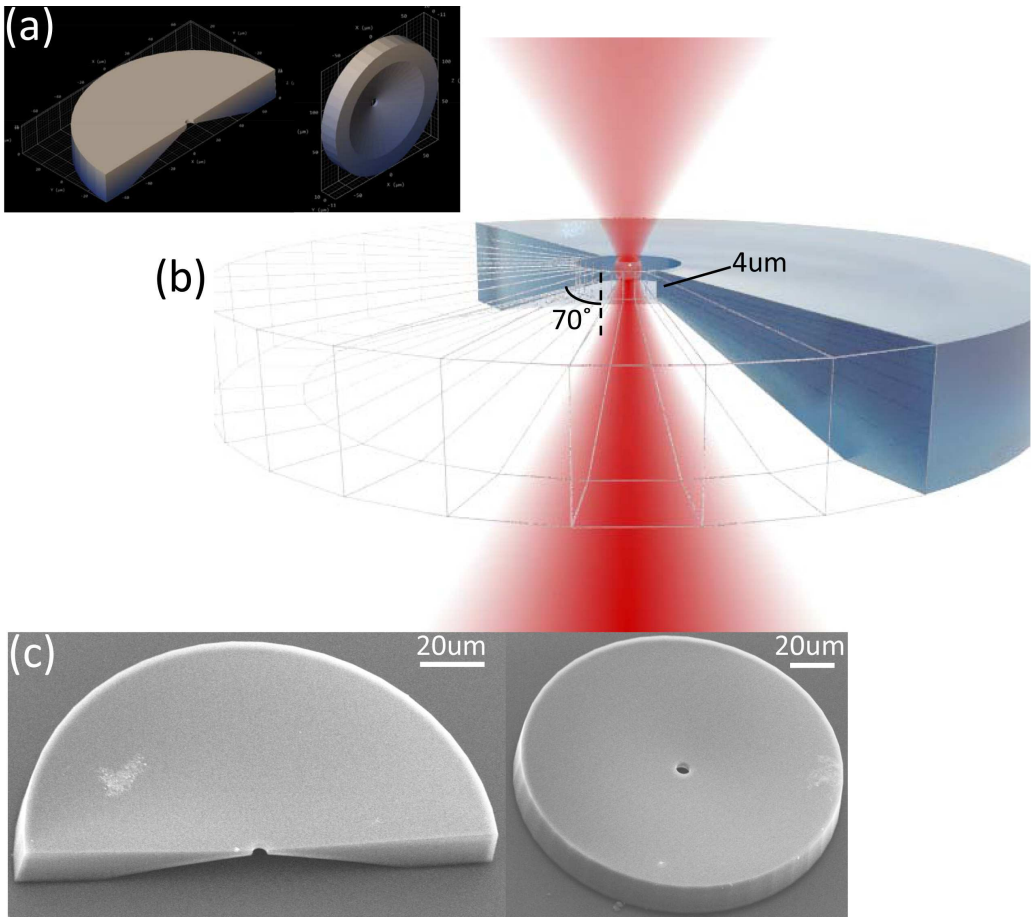

Figure 5.1: Structure of 3D printed finite cylinder. (a), 3D preview of structures of the curved wall and cylindrical wall designed for experiments. (b), In order to minimise the laser distortion by the wall, an inclined structure of the wall was used here. The angle of inclination is 70° and the height of the wall is 4 μm in the middle part. (c), Scanning electron microscope images for a curved wall with diameter of 5 μm and a cylindrical wall with diameter of 7 μm.

5.2, changes to the polarisation of a weak circularly polarised HeNe beam ($\sim$20 μW) passing through the particle and forming a tracking beam allowed precise measurement of the angular displacement.

A quarter-wave plate ($\lambda/4$) was placed in the trapping beam (1064 nm, $\sim$50 mW at the trap) path converting it to circularly polarised light. Thus, the particle is driven by the optical torque at a constant angular velocity Ω when the optical torque is balanced by drag torque from the surrounding fluid. Since the viscous torque is proportional to the angular velocity, the wall effect can be measured by spinning the probe particle with a constant optical torque, and measuring the angular velocity at different positions. The wall effect equals the ratio of the angular velocity far from the wall (Ω_0) to the angular velocity near the wall,

$$W_e = \frac{\Omega_0}{\Omega}. \tag{5.1}$$

Experimentally, rotation rates of the trapped particle could be determined by measuring the polarisation shift of the HeNe laser passing through the probe particle. The voltage difference ΔV between two detectors (D_1 and D_2) relates sinusoidally to twice the particle's angular position (ϕ), $\Delta V \propto \sin 2\phi$ [47].

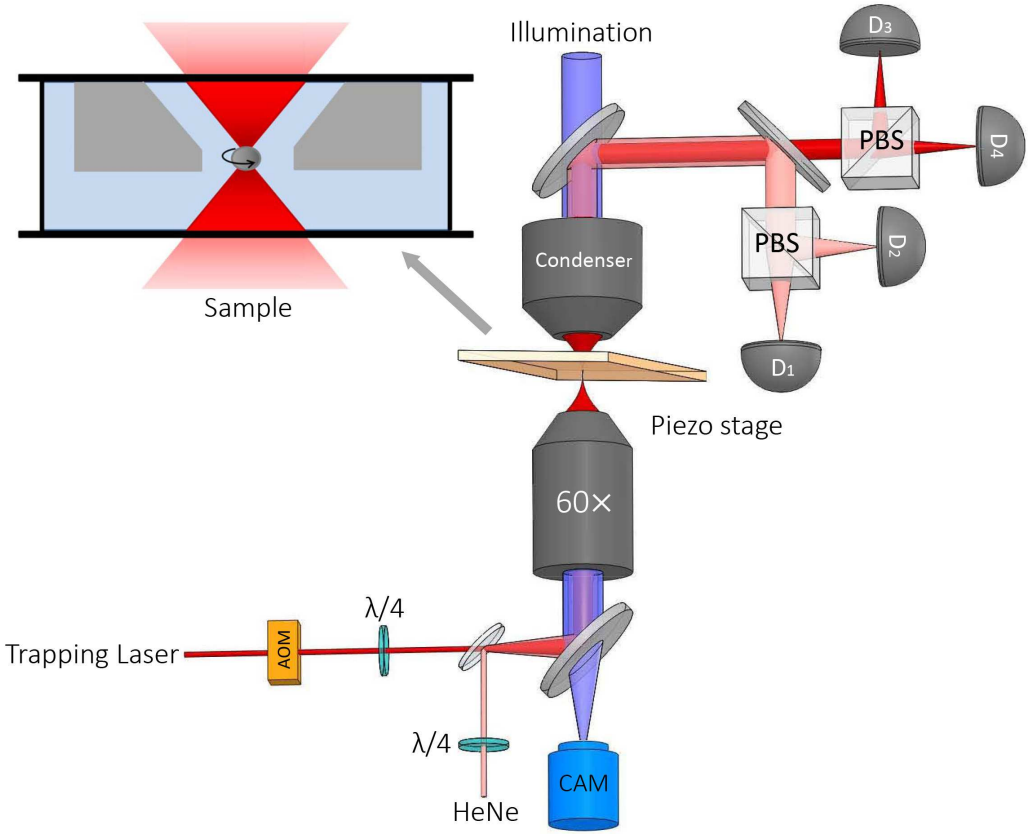

Figure 5.2: Experimental apparatus for measuring wall effects. An acousto-optic modulator (AOM) allows control of the trapping laser intensity. CAM: camera; PBS: polarising beam splitter; D_1–D_4: photodiode detectors. Top inset: schematic representation of the sample chamber with the 3D printed wall.

5.3 Modelling

As introduced in section 1.2, the effects of boundaries on the viscous torque can be calculated theoretically by solving the relevant equations of fluid motion (1.13) and then integrating the viscous torque around the particle from the resulting flow field. The theoretical wall effects of a sphere rotating in an infinite cylinder, a finite cylinder, and a sphere are calculated for comparison.

5.3.1 Infinite Cylinder

Firstly, we consider the problem of a sphere of radius a rotating with angular velocity Ω inside the centre of a stationary infinitely tall cylinder of radius R. In cylindrical coordinates (r,θ,z) and vector components, the stick boundary conditions are,

$$v_r = 0, \qquad v_\theta = \Omega r, \qquad v_z = 0, \qquad \text{when } a^2 = r^2 + z^2, \tag{5.2}$$

$$v_r = 0, \qquad v_\theta = 0, \qquad v_z = 0, \qquad \text{when } r = R \text{ or } |z| \to \infty. \tag{5.3}$$

Similar to the rotating concentric spheres problem (section 1.2.2), $v_r = v_z = p = 0$ satisfies the boundary conditions, and Stokes equations in cylindrical coordinates (appendix A), leaving only a single partial

differential equation (PDE) for $v_\theta(r,z)$,

$$0 = \frac{\partial^2 v_\theta}{\partial r^2} + \frac{1}{r}\frac{\partial v_\theta}{\partial r} + \frac{\partial^2 v_\theta}{\partial z^2} - \frac{v_\theta}{r^2}. \tag{5.4}$$

Brenner and Sonshine's Solution

This problem has been previously attempted by Brenner and Sonshine [104] who found that the PDE and cylindrical boundary condition (5.3) could be satisfied by

$$v_\theta = \frac{2a^3\Omega}{\pi}\sum_{n=0}^{\infty}\int_0^\infty \frac{C_n(ka)^{2n}}{(2n)!}\frac{K_1(kr)I_1(kR) - K_1(kR)I_1(kr)}{I_1(kR)}k\cos kz\,dk, \tag{5.5}$$

where I_1 and K_1 are respectively modified Bessel functions of the first and second kind. C_n are a set of arbitrary coefficients which can be determined by enforcing the remaining boundary condition (5.2). Brenner and Sonshine produced the system of equations indexed by m,

$$C_m - \sum_{n=0}^{\infty} C_n g_{n,m}\lambda^{2(n+m)+3} = \begin{cases} 1 & m = 0 \\ 0 & m \in \mathbb{Z}^+ \end{cases} \tag{5.6}$$

where $\lambda = a/R$, and $g_{n,m}$ are a set of constants defined by[1],

$$g_{n,m} \equiv \frac{2}{\pi(2n)![2(m+1)]!}\int_0^\infty \frac{k^{2(n+m+1)}K_1(k)}{I_1(k)}\,dk. \tag{5.7}$$

They also found that the wall effect is given just by the single coefficient, C_0, which they estimated by solving a truncated approximation of the infinite system. Brenner and Sonshine inverted the truncated system separately for each ratio of spherical and cylindrical radii (λ). We have reproduced Brenner and Sonshine's results more precisely over a larger domain, found more general series solutions to their system, and produced a simple formula to model these results.

Recursive Solution

Algebraically solving truncated versions for finite m can give large closed expressions of successive approximations for the wall effect C_0. However, it is also possible to find unlimited terms to a Taylor series expansion of C_0^{-1} about $\lambda = 0$ through recursion. An expression for C_0^{-1} in terms of C_m/C_0 can be obtained from the $m = 0$ equation in the system (5.6),

$$C_0^{-1} = 1 - g_{0,0}\lambda^3 - \sum_{n=1}^{\infty}\frac{C_n}{C_0}g_{n,0}\lambda^{2n+3}. \tag{5.8}$$

Similarly, by dividing the remainder of the equations by C_0, we can find expressions for C_m/C_0 which are independent of C_0,

$$\frac{C_m}{C_0} = g_{0,m}\lambda^{2m+3} + \sum_{n=1}^{\infty}\frac{C_n}{C_0}g_{n,m}\lambda^{2(n+m)+3}. \tag{5.9}$$

[1] Actually, $g_{n,m}$ is defined slightly differently here compared to the original paper, as to eliminate the need for factors of -1.

Each successive substitution of equation (5.9) back into (5.8) increases the order of the Taylor series,

$$C_0^{-1} = 1 - g_{0,0}\lambda^3 - \sum_{n=1}^{\infty} g_{n,0}\lambda^{2n+3}\left(g_{0,n}\lambda^{2n+3} + \sum_{j=1}^{\infty} g_{j,n}\lambda^{2(n+j)+3}\left(g_{0,j}\lambda^{2j+3} + \sum_{k=1}^{\infty} g_{k,j}\lambda^{2(j+k)+3}(\cdots)\right)\right). \quad (5.10)$$

Approximate Closed Form Model

For practical purposes it would be useful to have a relatively simple closed form expression accurate for all values of λ. If we approximate $C_n/C_0 = 0$ without any back substitution then we recover a simple approximation[2] most accurate when λ is small,

$$W_{\lambda\to 0} = \frac{1}{1 - g_{0,0}\lambda^3}, \quad (5.11)$$

where $g_{0,0} \approx 0.7968241722986522$. This expression becomes inaccurate when $\lambda \to 1$, but through lubrication theory, Brenner and Sonshine also provided an expression for the wall effect in the $\lambda \to 1$ limit,

$$W_{\lambda\to 1} = \frac{\pi}{2^{3/2}}\frac{1}{\sqrt{1-\lambda}}. \quad (5.12)$$

Therefore, we can combine these limiting expressions in a modified sum to produce a relatively simple closed form expression that can accurately quantify the wall effects for any value of λ. The expression for the $\lambda \to 1$ limit is modified by subtracting its Taylor series about $\lambda = 0$ so that its value and first three derivatives are zero at $\lambda = 0$, allowing the $\lambda \to 0$ term to dominate. λ^6, λ^7 and λ^8 terms were included in the numerator of the $\lambda \to 0$ part whose coefficients were obtained via a least squares fit of the model to the exact values. The resulting expression could describe the wall effect for all cylindrical radii with an error less than 0.3%,

$$W_{cyl} = \frac{\pi}{2^{3/2}}\left(\frac{1}{\sqrt{1-\lambda}} - 1 - \frac{\lambda}{2} - \frac{3\lambda^2}{8} - \frac{5\lambda^3}{16}\right) + \frac{1 - 4.481\lambda^6 + 6.747\lambda^7 - 3.07\lambda^8}{1 - g_{0,0}\lambda^3}. \quad (5.13)$$

The excellent agreement between equation (5.13) and the exact values is shown in figure 5.3.

5.3.2 Finite Cylinder

The axisymmetric wall effect of the rotating particle inside the 3D-printed finite cylinder was also calculated theoretically by solving equation (5.4) numerically using a Finite Element Method (FEM) in MATLAB via the Partial Differential Equation Toolbox. The wall effect was obtained by trapezoidal integration of the viscous stress obtained from the resulting flow field about a surface surrounding the sphere. Comparing the wall effects on a particle rotating at the centre of the cylindrical walls with 4 μm in height but with different ratios of cylinder to particles radius (figure 5.4 inset shows the geometry) can verify the numerical accuracy of the method. As shown in figure 5.4, the wall effect of the finite cylinder is only slightly less than those of an infinite cylindrical wall when the particle is placed at the centre.

[2]Interestingly, this approximate expression is equivalent to the rotational wall effect for concentric spheres when $R^3 = g_{0,0}b^3$.

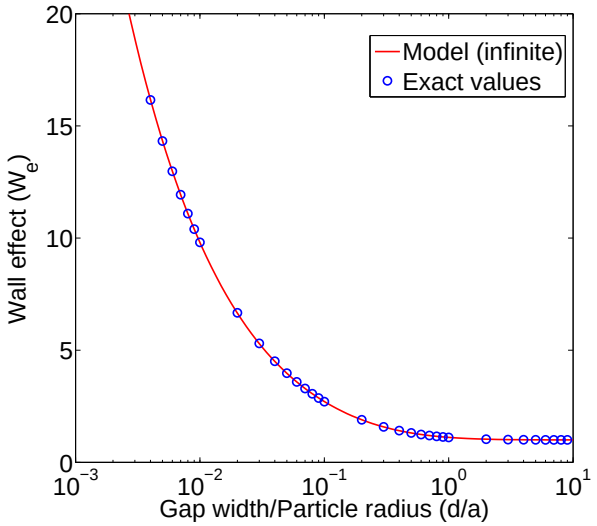

Figure 5.3: Wall effects of an infinite cylinder on an axisymmetrically rotating sphere. Our formula (5.13) for the wall effect of an infinite cylinder on the axisymmetric rotation of an internal sphere agrees with exact values (blue circles) with less than 0.3% error. The gap width can be related to the cylinder radius by $d/a = 1/\lambda - 1$.

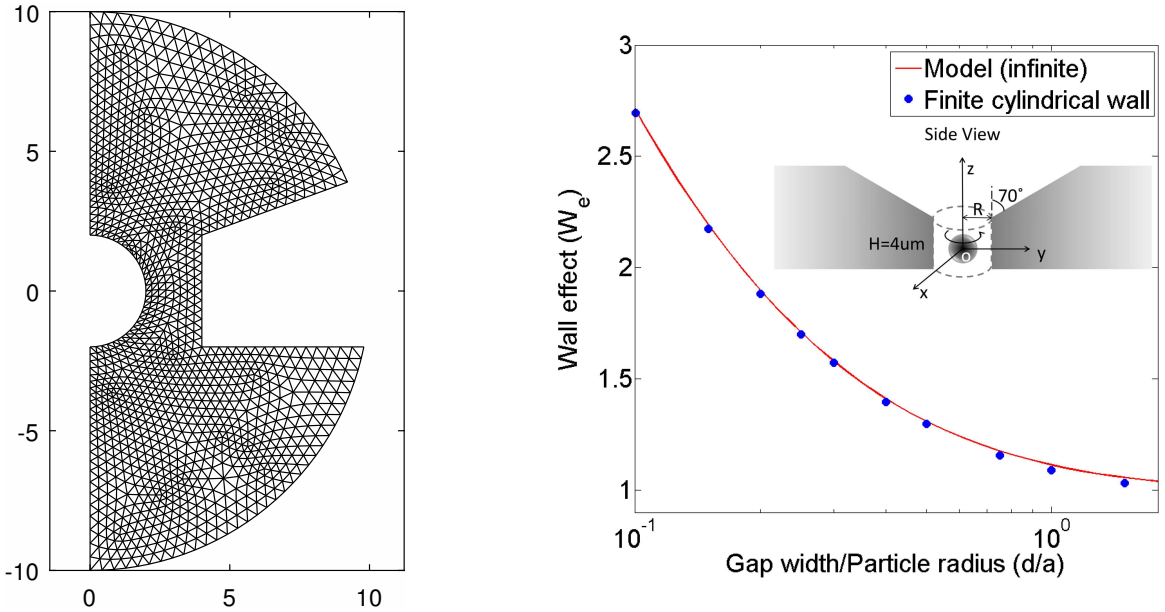

Figure 5.4: Numerical evaluation of wall effects of the finite cylinder when the sphere is centred. The left shows the finite cylinder geometry with an example FEM mesh. The bounds of the mesh are the internal sphere, z axis, finite cylinder, and an outer sphere of radius $10a$. The wall effect of this outer spherical boundary is negligible (0.1%) compared to the other boundaries. The actual meshes used were more fine than displayed here. On the right, numerical values of wall effects of a rotating particle at the center of the finite cylindrical wall (blue circles) are compared with the analytical solution (red line) of wall effects for infinite cylindrical walls using (5.13). Inset: Schematic diagram of the theoretical model system for the inclined wall with height of 4 μm.

5.4 Results

We studied the wall effects on a rotating particle placed inside a cylindrical wall. Inside the finite cylindrical wall (4 μm tall), we investigated the vertical as well as horizontal variation of the wall effects. For vertical measurements, the sphere was positioned along the z axis at differing heights as shown in figure 5.4 inset. While the sphere is rotating about the z axis the flow is axisymmetric. The derivatives of flow velocity at an intermediate boundary between the sphere and cylinder were obtained from the solution described in section 5.3.2, which allowed the wall effects to be calculated. Figure 5.5(a) shows an example of a particle of 2 μm radius rotating about the z axis inside a 5 μm diameter and 4 μm height cylindrical wall. The wall effect decreases when the particle moves along the z axis away from the center of the cylinder, and drops rapidly as the equatorial plane of the particle moves out of the cylindrical wall. This has been experimentally realised using optical tweezers as shown in figure 5.5(b). We find that wall effects of finite cylinders on rotating spheres depend on the vertical position of the particle, and that the distance between the wall and the equator of the particle seems to be particularly important.

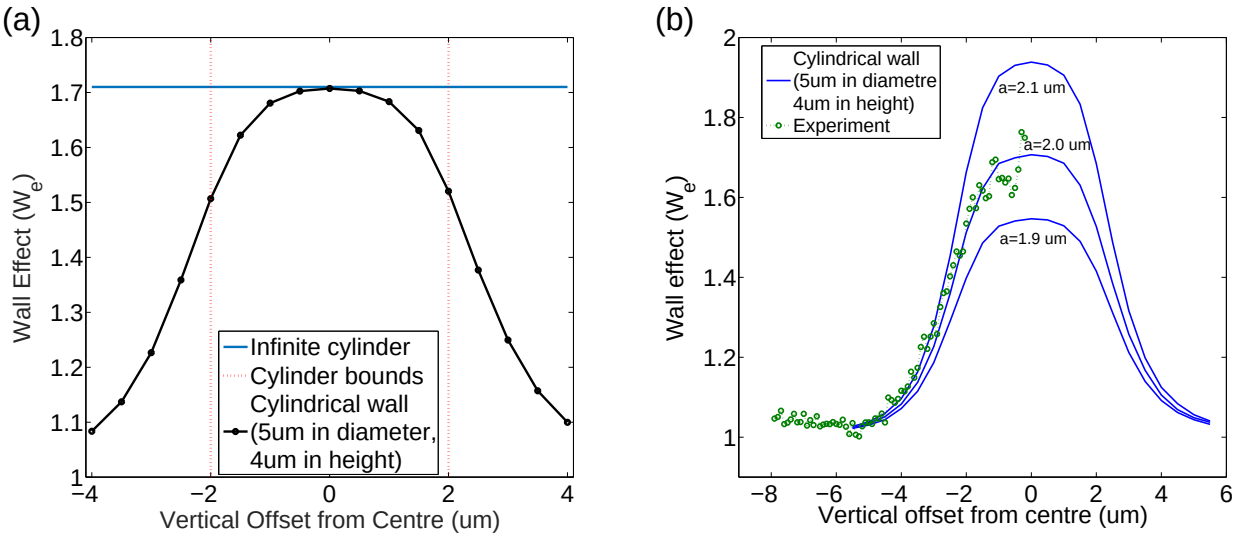

Figure 5.5: Comparison between numerical and measured axisymmetric rotational wall effects. (a) Numerical results for wall effects (black) of a 2 μm rotating particle at the center of a ring wall with 5 μm in diameter and 4 μm in height varies with distance of vertical offset from center. "Infinite cylinder" (blue) represents the value of this particle at center of a infinite cylinder. "Cylinder bounds" (green) shows the region where the equatorial plane of the spherical particle is within the wall of model. (b) Experimental measurements of vertical wall effects on a rotating particle ($\sim$2 μm in radius) inside a cylindrical wall with 5 μm in diameter, 4 μm in height (green circles). The solid lines represent theoretical results of wall effects acting on a sphere with different radii (a=1.9, 2 and 2.1 μm) calculated numerically. The experimental results agree with the theoretical model. The vertical wall effect was accessible only from one side because the structure was mounted on the cover slip (figure 5.2 inset).

Therefore, to further investigate the cylindrical wall effects, we moved the vaterite particle between the centre and the side of the cylindrical wall along a radial direction. Since the position of the equatorial plane seems to be the dominant factor, we expect that the wall effects should be similar to,

but a bit less than, that of an outer spherical boundary on asymmetrically rotating sphere (section 4.2.4). As seen in figure 5.6 (a)–(c), the measured wall effects increased as the trapped particles were brought closer to the side. We compared the wall effects of three different radius ratios R/a ($R/a \sim 2,3,4$) with the theoretical bounds of wall effects for a plane wall and eccentric spherical wall found in chapter 4. Although we do not have exact theoretical predictions for the wall effects from the finite cylinder on the eccentric sphere, the plane wall and eccentric spheres serve as relatively tight bounds that seem to agree well with the experimental results.

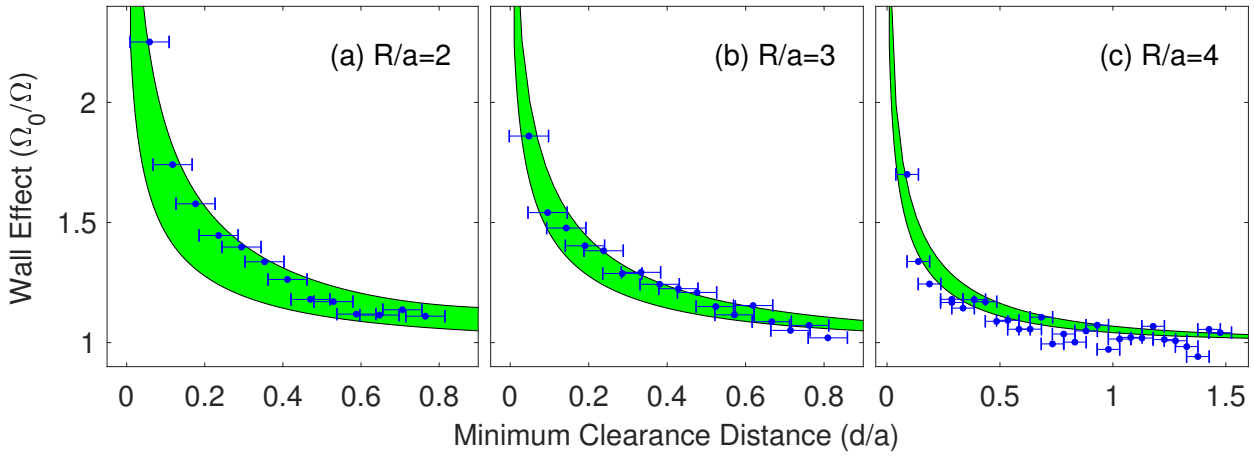

Figure 5.6: (a)–(c), Experimental measurements of wall effects of cylindrical walls on rotating eccentric spheres (blue dots) are compared with theoretical values from chapter 4 of a particle rotating near a plane wall or inside a sphere (shaded green region).

5.5 Conclusions

In this chapter, we have presented a combined theoretical and experimental study of wall effects of cylinders on a rotating particle. Whereas chapter 4 investigated the wall effects of spheres and their applicability in biological systems, here we further developed the theory to be applicable in cylinders and evaluate its performance in a real optical tweezers system containing solid curved walls. Accordingly, we fabricated 3D-printed cylindrical walls and used them in combination with rotational optical tweezers to measure both axisymmetric and asymmetric rotational wall effects on an optically trapped particle. Unlike the measurements near flexible biological boundaries presented in section 4.4, these solid boundaries constrain the error in measurements enough to demonstrate strong agreement with theory. This study of wall effects is relevant to microrheology and optical sensing techniques in microfluidic devices.

Chapter 6

Machine Learning Drag Tensors of Non-Spherical Shapes

Objects within optical tweezers systems (trapped or otherwise) are often not spherical and so it is important to be able to compute the hydrodynamic forces acting on these more general shapes. Numerical methods, such as point matching (section 2.5), can be very slow ($\sim 10^0$s) to calculate fluid flow and hydrodynamic forces. Hence, they are often not applicable in scenarios where drag needs to be evaluated frequently and quickly. This includes simulations where a particle shape changes over time, such as simulating optically trapped biological swimmers. It also includes experimental systems where drag tensors (section 1.2.1) need to be calculated in real-time, such as in a control system. In these kinds of systems fast computation is often more desirable than precise, but slow, computation. Therefore, this chapter aims to develop a model using machine learning which can efficiently estimate the drag tensor of star-shaped objects[1] in a free viscous fluid. The machine learns from many drag tensors of randomly shaped particles calculated using the point matching method. By observing these examples the machine effectively fits a model to the data, allowing it to interpolate and efficiently predict drag tensors of novel unseen particles. This process is broadly outlined by the following flow diagram.

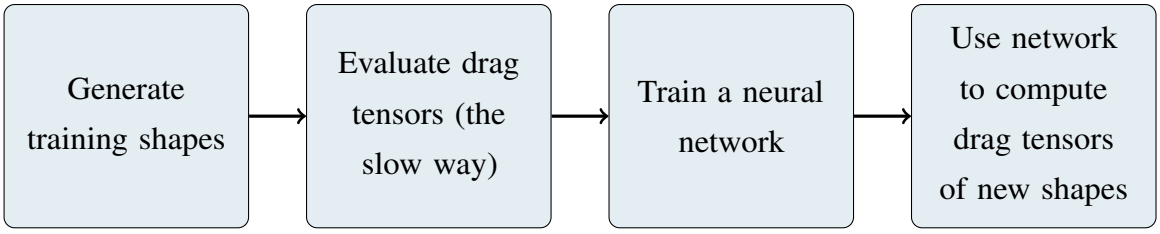

[1] A star shaped object contains an internal origin in which the radial coordinates of the entire surface can be expressed as a function of the polar and azimuth angles.

6.1 Generating Shapes

The machine model used is a multilayer perceptron (MLP), a type of artificial neural network discussed previously in section 4.3. This kind of model requires training data for the network to undergo supervised learning. To obtain training data, the drag tensors of randomly generated star-shaped particles are calculated using the point matching method. This section outlines the process used to generate these particles.

6.1.1 Spherical Harmonics

Star-shaped particles contain an internal point whose radial lines each pass through the surface at exactly one point. Mathematically, this can be expressed using spherical polar coordinates by choosing an origin such that the radial coordinates at the surface can be defined by a function $r(\theta,\phi)$. Therefore, generating random star-shaped particles involves generating random continuous functions on the spherical domain.

One way to accomplish this would be to generate random values of r at different angular coordinates and use some kind of interpolation to fill the particle surface. However, this would likely result in 'spiky' shapes that do not resemble realistic particles and whose drag tensors would be more difficult to compute. Instead, $r(\theta,\phi)$ can be represented using a linear combination of basis functions which cover the whole domain smoothly. The obvious choice is to use spherical harmonics, representing the function by

$$r(\theta,\phi)=\sum_{n=0}^{10}\sum_{m=0}^{n}P_n^m(\cos\theta)[a_{n,m}\cos(m\phi)+b_{n,m}\sin(m\phi)], \tag{6.1}$$

where P_n^m represents normalised associated Legendre functions[2] and coefficients, $a_{n,m}$ and $b_{n,m}$, are the contributions of each spherical harmonic to the total. The series is truncated at order $n=10$ which should be high enough to capture interesting features of the particles.

6.1.2 Generating Coefficients

Generating random shapes of the form given by equation (6.1) involves choosing the contributions of each spherical harmonic. In this case, values for the coefficients $a_{n,m}$ and $b_{n,m}$ are chosen randomly, and then the shapes are filtered based on some criteria. Initially, $a_{n,m}, b_{n,m}\sim\mathcal{N}(0,(n+1)^{-2K})$ so that each coefficient, except for $a_{0,0}=1$, is independently sampled from a zero mean normal distribution[3] with a standard deviation of $(n+1)^{-K}$, where $K\sim\mathcal{N}(2.5,0.5^2)$ is a single constant independently sampled for each particle.

Using 100 approximately evenly spread points on each particle (see section 2.5.1), the maximum and minimum radial coordinates (r_{max} and r_{min}) were estimated so that particles could be filtered

[2] In this chapter the associated Legendre functions are normalised such that $\int_{-1}^{1}P_n^m(\mu)^2\,d\mu=1$. Note that in other chapters P_n^m might instead denote non-normalised associated Legendre functions.

[3] $X\sim\mathcal{N}(\mu,\sigma^2)$ denotes that a random variable X is sampled from a normal distribution with a mean and standard deviation of μ and σ respectively.

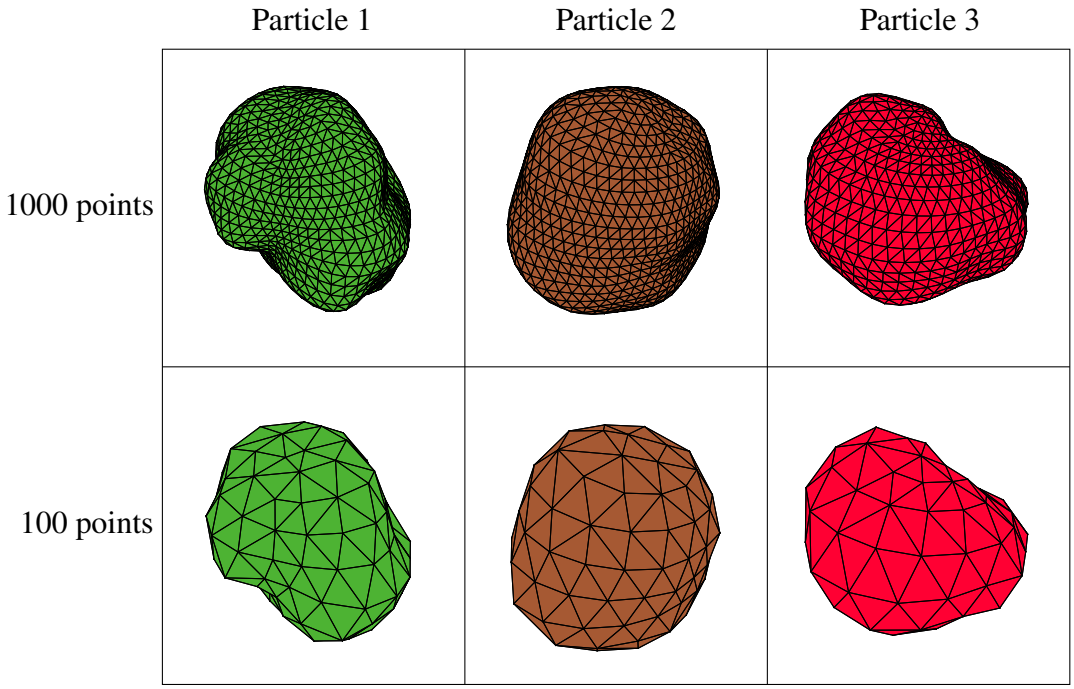

Figure 6.1: Three examples of randomly generated particles distinguished by column. The shapes are represented using points distributed using the methods presented in section 2.5.1. The top row displays these particles at a higher resolution (1000 points) than the bottom row (100 points).

based on their aspect ratio. In particular, particles needed $r_{min} > 0.1$ and $r_{max}/r_{min} < 3$ to ensure they were valid particles and that the numerical results computed by the point matching method would be accurate. Finally, the size of the particles were normalised by scaling their coefficients by the *median r* obtained by sampling 100 points. This removes a degree of freedom without loss of generality. Figure 6.1 illustrates three examples of these randomly generated particles.

6.2 Evaluation of Drag Tensors

The purpose of this machine is to evaluate the viscous drag tensor (see section 1.2.1) of generic star-shaped particles. Together with the viscosity, velocity and angular velocity, this fully characterises the viscous forces and torques acting on the particles in a free fluid. The drag tensors of the training particles need to be computed using existing slower methods.

6.2.1 Applying the Point Matching Method

The simple relationship between the total force and torque acting on a particle and the first order series components of Lamb's series solution (section 2.1) makes the point matching method a good candidate to compute the drag tensors ($\mathscr{D}$) of the randomly generated shapes. The drag tensor relates the drag forces and torques to the particle's geometry (see section 1.2.1 for more details). The method must be applied six times to each particle, one for each column of the drag tensor. These columns correspond to different boundary conditions which can be broken down into Cartesian linear and

angular motion of the particles. The first column corresponds to the force and torques when $v_x = 1$ and $v_y = v_z = \Omega_x = \Omega_y = \Omega_z = 0$. The second column is obtained by setting $v_y = 1$, and the others so forth.

6.2.2 Quantifying Point Matching Error

The MLP is unlikely to outperform the examples it learns from, so the training drag tensors calculated via point matching must be sufficiently accurate. Therefore, it is important to have error metrics to quantify the performance of the point matching method itself. The error ($\Delta\mathscr{D}$) in the drag tensors as evaluated using the point matching ($\mathscr{D}_{PM}$) is quantified in two ways. The first utilises the symmetry of the drag tensor. The antisymmetric component of the drag tensors computed by the point matching method must also be the antisymmetric component of the error matrix since the drag tensor is symmetric.[4]

$$\mathscr{D}_{PM} = \mathscr{D} + \Delta\mathscr{D}, \tag{6.2}$$

$$\frac{1}{2}\left(\mathscr{D}_{PM} - \mathscr{D}_{PM}^T\right) = \frac{1}{2}\left(\mathscr{D} - \mathscr{D}^T\right) + \frac{1}{2}\left(\Delta\mathscr{D} - \Delta\mathscr{D}^T\right), \tag{6.3}$$

$$\frac{1}{2}\left(\mathscr{D}_{PM} - \mathscr{D}_{PM}^T\right) = \frac{1}{2}\left(\Delta\mathscr{D} - \Delta\mathscr{D}^T\right). \tag{6.4}$$

This means that the antisymmetric contribution of the error can be calculated directly from the point matching drag tensor,

$$\Delta\mathscr{D} = \frac{1}{2}\left(\Delta\mathscr{D} + \Delta\mathscr{D}^T\right) + \frac{1}{2}\left(\Delta\mathscr{D} - \Delta\mathscr{D}^T\right), \tag{6.5}$$

$$= \frac{1}{2}\left(\Delta\mathscr{D} + \Delta\mathscr{D}^T\right) + \frac{1}{2}\left(\mathscr{D}_{PM} - \mathscr{D}_{PM}^T\right). \tag{6.6}$$

Therefore, a scalar error estimate ($\Delta\mathscr{D}$) for the point matching drag tensor is found by taking the maximum value of its antisymmetric component.

The second error metric is based on how well the point matching satisfies the boundary conditions. The drag tensor is computed from six different boundary conditions: translation along and rotation about the x, y and z axes. Taking the maximum root mean squared error (RMSE) of the fluid flow at the boundary across all six conditions can give an alternative error estimate. Although this does not give the error of the drag tensor directly, it should be a good indication of numerical performance.

6.2.3 Training an Intermediate Network to Choose Series Order

The point matching method requires Lamb's series solution to be truncated at finite order. This truncation point must be high enough to constrain the drag tensor error, but also low enough to keep the method computationally viable. The conditionality of the system, as well as the inversion time, quickly grow for large orders. Therefore, time and precision constraints limit the option of simply choosing a high order for all shapes.

[4] Any square matrix can be spit into the sum of a symmetric part and an antisymmetric part, $M = \frac{1}{2}\left(M + M^T\right) + \frac{1}{2}\left(M - M^T\right)$.

Moreover, the relationship between series order, particle geometry and drag tensor accuracy is not straightforward. To effectively choose series order while still balancing accuracy, time and precision constraints, an intermediate multilayer perceptron (MLP) was trained to learn this relationship. This intermediate MLP would output a series order, given inputs of the (log) error metrics mentioned in section 6.2.2, and some information about the particle geometry. This intermediate network could then be used to choose appropriate series orders to evaluate the drag tensors of even more shapes that could then be used to train the final network. This processed is outlined by the following flow diagram.

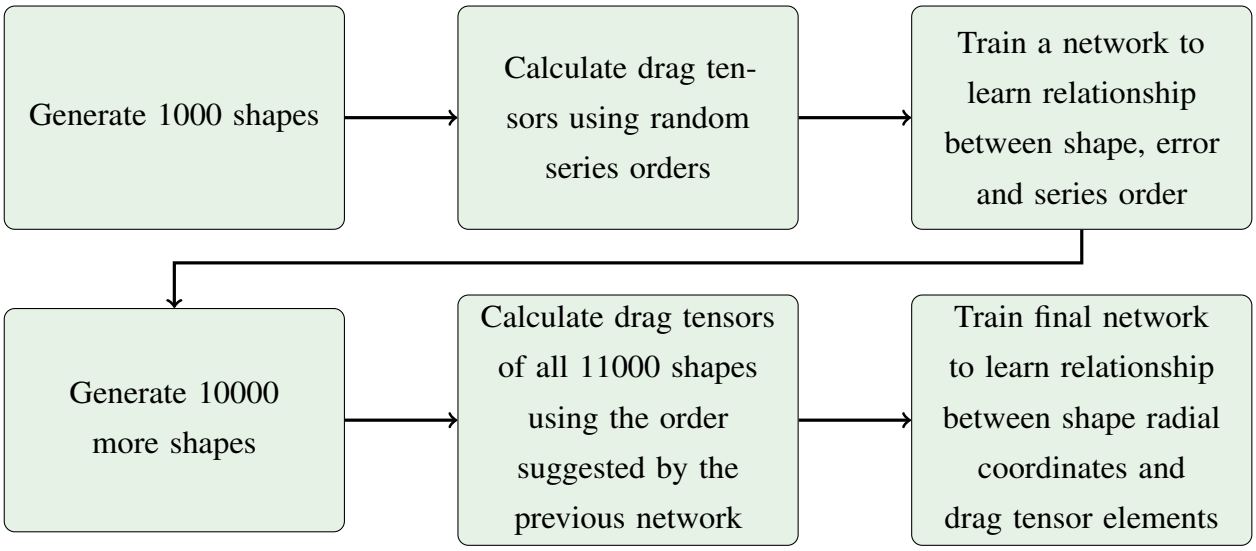

Training data for the intermediate MLP is needed, so 1000 shapes were generated and their drag tensors calculated using a random uniformly distributed series order $3 \leqslant n \leqslant 8$. For simplicity, each particle was represented using only four values: the radial values at the 0, 33.33, 66.67 and 100 percentiles (calculated from 1000 points). The MLP had the aforementioned 6 inputs (2 error metrics and 4 radial values), 1 output and a hidden layer with 10 nodes. Once trained on 700 shapes (validated on the remaining 300) using Levenberg–Marquardt backpropagation in MATLAB, the network could then predict the required series order for each shape that would constrain the drag tensor to the desired error. Figure 6.2 plots the performance of this intermediate network. The network performed reasonably well, predicting the series order within 1 correctly for about 81% of the 300 validation shapes. The ceiling of the network output was taken to produce an integer. This is because higher orders that take a little more time are considered better than lower orders that are too inaccurate.

After training the intermediate MLP, it is possible to re-evaluate the drag tensors of the 1000 particles (and new particles as well) using the point matching series orders predicted by the intermediate network. Ultimately, we desire the point matching drag tensors to be accurate to within about 1%, and at least within 10% error. In the RMSE error metric this corresponds to a value of about 10^{-2} because the boundary conditions of the fluid velocity are valued at about ~ 1. For a sphere of radius 1 the maximum value of the drag tensor is 8π so the desired relative error should be less than $8\pi/100 \approx 10^{-0.6}$. However, to capture the smaller effects of the other tensor elements, and to account for the fact that the antisymmetric error is not the total error, a stronger error target of $10^{-1.5}$, with almost an extra order of magnitude, was used.

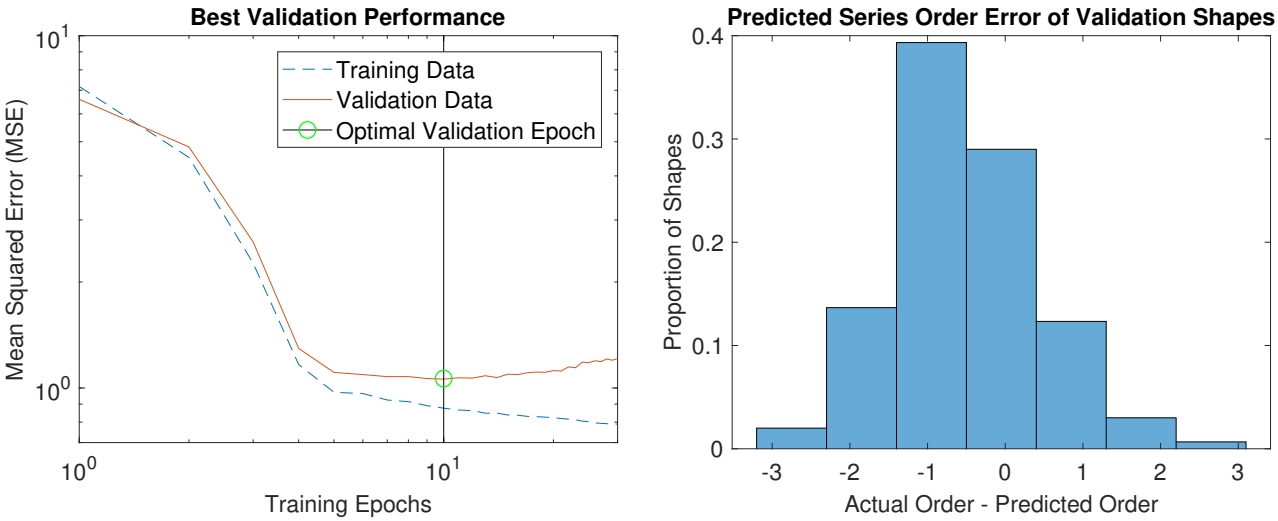

Figure 6.2: Left shows the performance of both the training data (blue dashed) and the validation data (orange) as the intermediate MLP is trained. Right shows a histogram of the error of the predicted order of the 300 validation shapes when calculated by taking the ceiling of the network output. The network over predicts the series order of 55% of the shapes, under predicts 16% and predicts accurately 29%. The predicted series order of about 81% shapes is within 1 of the correct value.

Figure 6.3 examines the error metrics of the 1000 particles and how the errors depend on series order. The positive correlation between the two error metrics is quite clear. As expected, the error of drag tensors is negatively correlated to the randomly chosen series order. However, after recalculating the drag tensors using the intermediate network series orders, the errors are more clustered around the target values and the correlation between series order and error is reversed. This is likely because the higher series orders are actually still too low in many cases. This is particularly apparent where the geometric means of series orders 4–7 are tightly clustered but shapes with orders 8–9 have larger error. Figure 6.4 further illustrates the performance of the intermediate network by plotting histograms of the error metrics of the 300 validation shapes.

6.3 Training and Evaluation of Neural Network

The final model can be trained now that it is possible to create example shapes and drag tensors. Using the intermediate network discussed in the preceding section an additional 10000 shapes were generated and their drag tensors evaluated using the point matching method, giving a total of 11000 shapes. Of these 7000 are used as training data to let the MLP learn the relationship between the particle geometry and the drag tensor. 3000 shapes would be used as validation to avoid over fitting the model to maximise generalisability, and 1000 reserved to test the performance of the final model.

6.3.1 Network Structure

As illustrated in figure 6.5, the final network is a MLP which inputs the radial values of 100 points at angles chosen using the method outlined in section 2.5.1. These inputs undergo min-max normalisation before passing through a single hidden layer containing 30 nodes. The output layer contains 21 nodes

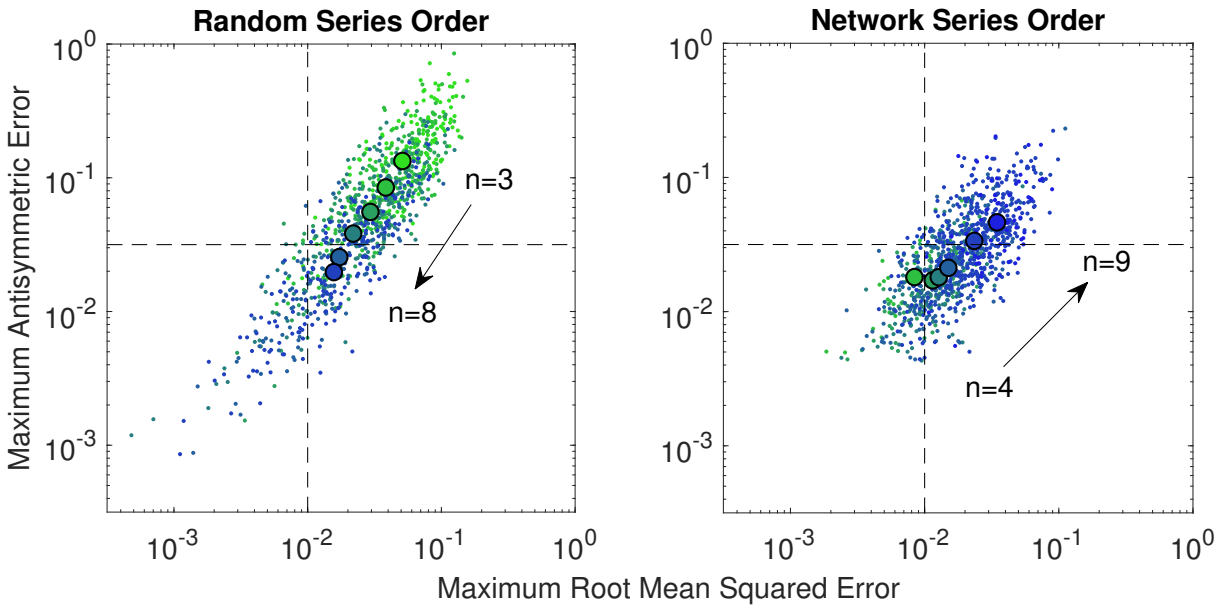

Figure 6.3: A comparison between drag tensor error metrics for different point matching series orders. On the left the series orders of all 1000 points are randomly chosen between 3 and 8. On the right the series orders are chosen using the ceiling of the intermediate network output which targeted errors of $(10^{-2}, 10^{-1.5})$, indicated by the black dashed lines. The small points represent individual shapes, while the large dots indicate the geometric means of shapes grouped by series order. The colours, from green to blue, distinguish series order.

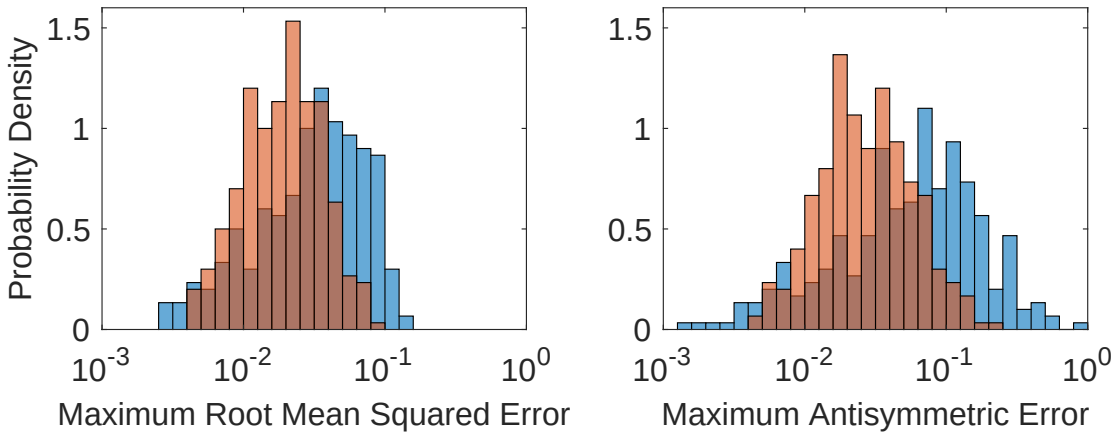

Figure 6.4: Histograms of the root mean squared error (left) and antisymmetric error (right) of the 300 validation shapes. The blue bars correspond to the error distributions when series orders were randomly chosen and the orange bars when the series order was chosen using the intermediate MLP.

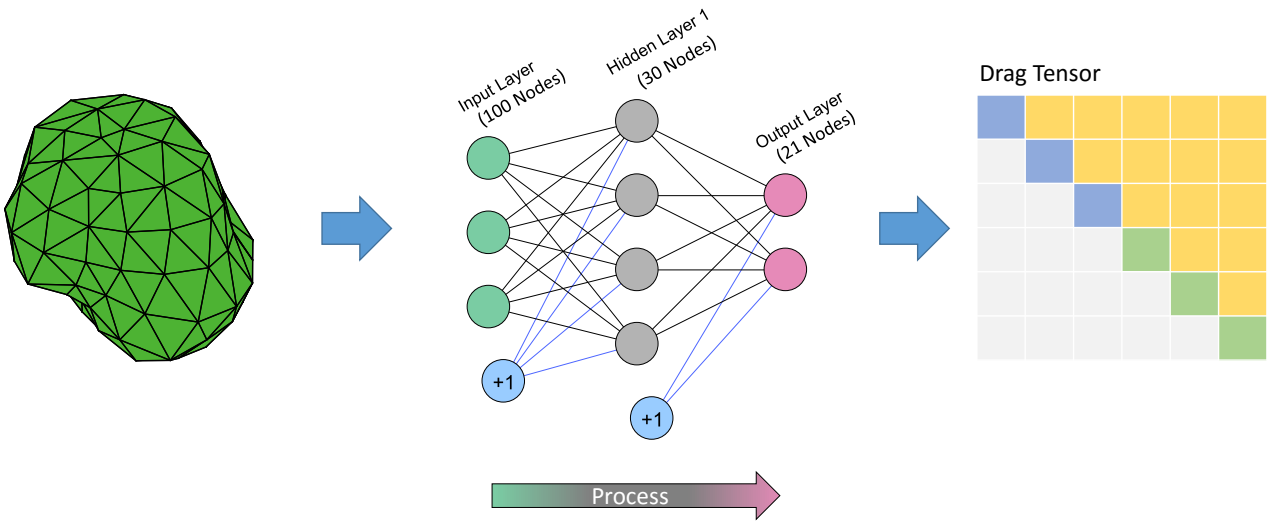

Figure 6.5: Network structure. The network inputs 100 normalised radial coordinates at fixed angular positions and outputs the 21 elements of the drag tensor. 30 nodes in the single hidden layer were enough to compute the final drag tensors with acceptable accuracy.

which correspond to the 21 independent values of the symmetric 6×6 drag tensor. This whole process is about 4 orders of magnitude faster than the point matching method, taking only $\sim 10^{-4}$s to compute the drag tensor of one particle.

The network was trained on 7000 shapes using scaled conjugate gradient backpropagation in MATLAB until the sum squared error of the 3000 validation shapes failed to improve for 1000 epochs.

6.3.2 Network Performance

The performance of the final network can be evaluated by comparing its outputs on the 1000 test shapes not used in the training process with the drag tensors computed via the point matching method. Figure 6.6 plots histograms of these errors. The distribution of relative errors of the diagonal elements is separated from the absolute errors of the off-diagonal elements because for the majority of star shaped particles, the diagonal elements are dominant while the off-diagonal elements are often zero, or close to zero. The network performed quite well on the test shapes achieving relative errors of $\leqslant 10^{-2}$ for 86.7% of diagonal elements and absolute errors of $\leqslant 10^{-1}$ for 77.2% of off-diagonal elements.

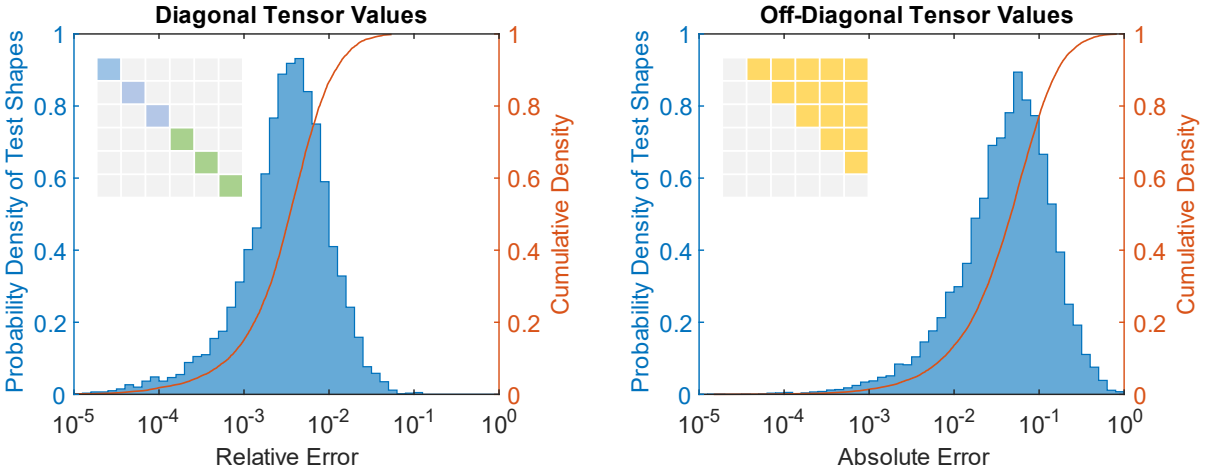

Figure 6.6: Histograms of error between the network and point matching of 1000 test shapes. The left plots the distribution of relative errors of the diagonal elements of the drag tensor, while the right plots the absolute errors of the off-diagonal elements.

6.3.3 Performance on Specific Geometries

The network performs well on the kinds of shapes it was trained on. However, it is also worth testing its performance on some specific shapes that could be relevant to some real simulations or experiments. Figure 6.7 compares the drag tensors of a sphere, cube and pill shape[5] as calculated via point matching and the MLP. Evidently the network performs quite well, with the small exception of the rotation of the pill about its short axis.

The pill is an interesting shape because of its resemblance to E. coli bacteria. By changing the aspect ratio (length/width) of the pill it also allows some of the limitations of the network to be tested. Figure 6.8 plots the performance of the network on pill shapes as a function of their aspect ratio. The network performs well when the aspect ratio is less than 2, the domain where the point matching can provide reliable computation of the drag tensor. However, it is clear that the error increases with aspect ratio, and extrapolating this trend shows that the network probably only gives a rough approximation of the drag tensor by the time the aspect ratio reaches 4, values close to that of E. coli.

[5] A pill shape consists of a central cylinder and two hemispherical caps of the same radii.

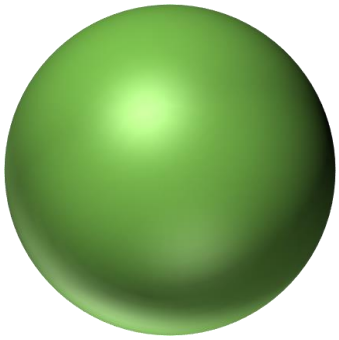

-18.89	0.0057	0.0058	-0.0012	-0.0023	0.00064
	-18.90	0.0020	0.0039	-0.00060	0.0012
		-18.88	-0.00072	0.0014	0.00077
			-25.22	-0.013	-0.0033
				-25.21	-0.0011
					-25.21

-18.85	0	0	0	0	0
	-18.85	0	0	0	0
		-18.85	0	0	0
			-25.13	0	0
				-25.13	0
					-25.13

-19.56	-0.022	0.038	0.00066	0.0057	0.085
	-19.60	0.026	-0.022	-0.0037	0.24
		-19.52	-0.099	-0.28	-0.0024
			-29.22	0.17	0.062
				-29.38	0.21
					-29.28

-20.00	0	0	0	0	0
	-20.00	0	0	0	0
		-20.00	0	0	0
			-29.90	0	0
				-29.90	0
					-29.90

-23.90	-0.028	0.073	-0.0046	0.22	-0.18
	-23.85	0.065	-0.13	0.023	-0.0075
		-21.67	0.22	0.024	-0.013
			-55.99	0.37	0.014
				-56.43	-0.19
					-32.69

-24.16	0	0	0	0	0
	-24.16	0	0	0	0
		-21.47	0	0	0
			-61.43	0	0
				-61.43	0
					-33.47

Figure 6.7: A comparison between drag tensors ($-\mathscr{D}$) output by the network (top matrix of each section) and theoretical values (bottom matrix of each section) for a sphere of radius 1 (top section), a cube with a side length of $4/(\sqrt{2}+1)$ (middle section) and a pill of length $2\sqrt{3}$ and diameter $\sqrt{3}$ (bottom section)

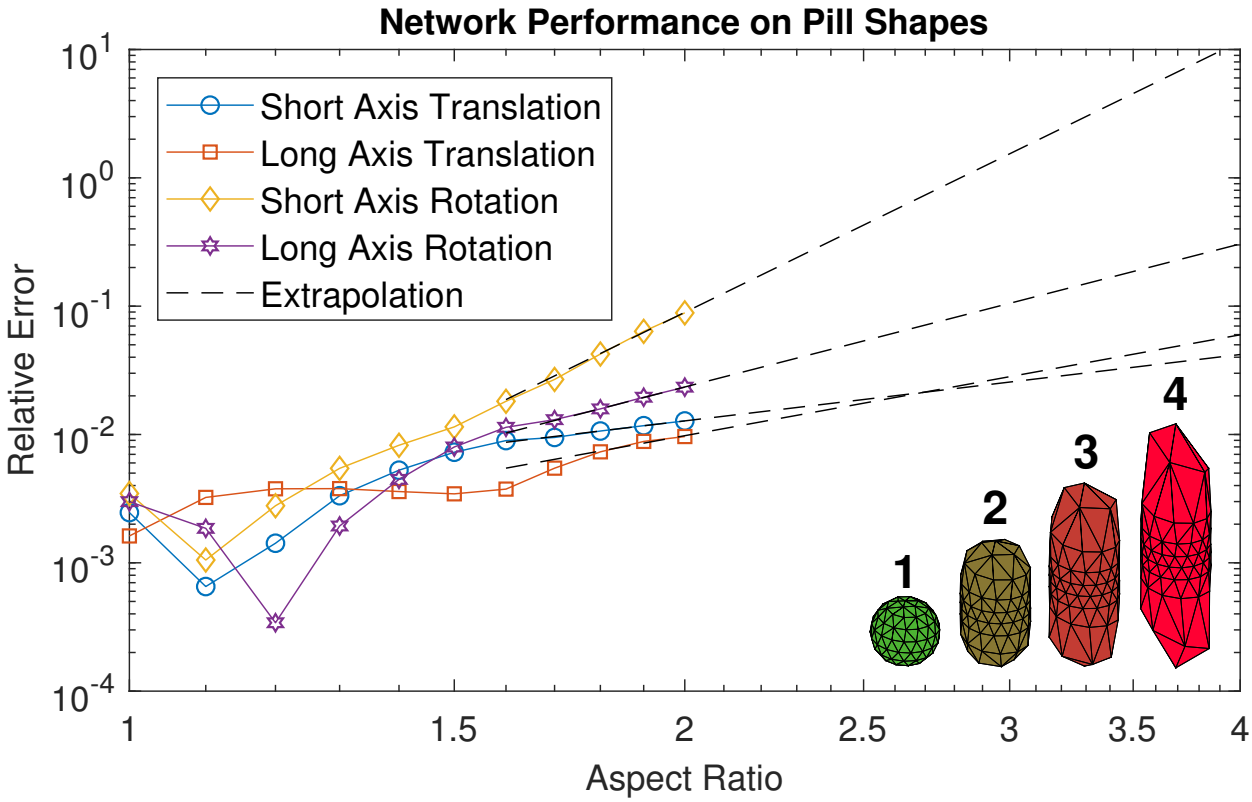

Figure 6.8: Relative errors of the network output compared to the point matching method when calculating the drag tensor of a pill shape. The lines with markers represent errors of the diagonal elements of the drag tensor. Since the pill is rotationally symmetric about its long axis, there are only four independent values: translation about the short (blue circles) and long (red squares) axes, and rotation about the short (yellow diamonds) and long (purple stars) axes. The dashed lines represent extrapolations calculated by linear regression of the final three points of each line on the log scale. The bottom right side of the figure includes examples of point clouds of pill shapes of aspect ratios of 1–4.

6.4 Conclusion

The goal of producing a model that can efficiently compute accurate drag tensors of non-spherical star-shaped particles has been achieved for shapes with aspect ratios less than about 3. Provided that the shape can be represented by 100 radial values at specific angular coordinates, the tensor can be calculated in the order of 10^{-4}s, fast enough for simulations and real-time experimental control. Unfortunately, for aspect ratios higher than 3, such as the shape of an E. coli bacteria, the drag tensor is likely to be inaccurate for some of its components. Despite this, the network can still serve as a useful tool in quickly computing hydrodynamic forces acting on lower aspect ratio shapes found in optical tweezers systems.

Chapter 7

Conclusion

This dissertation investigated hydrodynamic forces in systems which utilise optical tweezers through innovations in optical tweezers microrheology, novel solutions to Stokes equations of fluid dynamics, comparison with experimental results by Shu Zhang *et al.*, and application of machine learning techniques.

Chapter 2 presented a generalised approach to finding general series solutions to the Stokes equations of fluid dynamics. This approach found solutions based on separable harmonic functions, reproducing Lamb's series solution in spherical coordinates, as well as finding series solutions in Cartesian and cylindrical coordinates. Although not presented here, this method should also be able to find solutions in other orthogonal coordinate systems that separate the Laplace equation. Additionally, by point matching the series solution and boundary conditions, these series solutions are also applicable in problems where it is impractical or impossible to obtain the series coefficients analytically. These solutions give a platform for calculating fluid dynamics and hydrodynamic forces in optical tweezers systems that contain viscous fluids.

Chapter 3 explored how hydrodynamic forces in optical tweezers could be used to measure the complex shear modulus. Previous optical tweezers microrheometers have been limited by their several-minute measurement duration, making them unreliable in biological systems that are slowly changing. To solve this problem new theory and analysis was introduced and experimentally verified by Shu Zhang *et al.*. The new analysis methodology improved the signal to noise ratio by applying non-linear driving forces, thereby enabling optical tweezers to perform highly localised measurements of viscoelasticity in sub-minute times. This solves the duration problem that had previously limited particle tracking methods in biological domains, like a living cell.

Chapters 4 and 5 investigated hydrodynamic interactions between trapped spheres near curved boundaries by employing both analytical and numerical methods to solve the Stokes equations for comparison with experimental measurements. The wall effects of an outer spherical boundary on arbitrary motion of an internal sphere were calculated and also used to train an artificial neural network. Comparison with the experimental results of Zhang *et al.* [4] show that the asymmetric rotational wall effects are measurable and within experimental variation when spinning an optically trapped sphere

inside a liposome. This demonstrates that the theoretical methods presented in this dissertation should be able to constrain errors from experimentally realisable wall effects to much less than other sources of variation in real biological systems. Similar theoretical results regarding wall effects of cylinders on a rotating sphere show even better agreement with experimentally measured wall effects by Zhang *et al.* [2] of a solid cylindrical wall on an optically trapped particle. This further validates the approach to quantifying wall effects in systems with solid surfaces, such as inside a microfluidic device.

Finally, chapter 6 explored how machine learning could be utilised to allow efficient computation of hydrodynamic forces acting on non-spherical star-shaped particles. Calculating drag tensors describing this geometry using point matching was relatively slow ($\sim 10^0$s). The drag tensors of many randomly generated particles were used to train an artificial feed-forward neural network to improve the speed ($\sim 10^{-4}$s) at which these drag tensors could be evaluated, making them practical for simulations or real time calculations. Although the network was only accurate for aspect ratios less than 3, in the future it should be possible to train the network on drag tensors of higher aspect ratio shapes, evaluated using point matching in cylindrical coordinates. Even as it stands now, the network can still serve as a useful tool in quickly computing hydrodynamic forces acting on lower aspect ratio shapes found in optical tweezers systems.

By focusing on major sub-problems within the key hydrodynamic forces factors of particle geometry, boundary interactions, and fluid properties, this dissertation has made good developments in theoretical hydrodynamics that are applicable in a very broad range of optical tweezers systems. It has further improved the domain in which optical tweezers can be applied, as well as improved calculation methods that make optical tweezers simulations more efficient and accurate. For example, this includes the ability to use optical tweezers as a microrheometer within biological systems that are slowly changing, or near spherical or cylindrical walls, like perhaps cell walls or blood vessels, or within microfluidic devices. It also allows optical tweezers to make better use of non-spherical particles in both experiments and simulations. This could lead to some innovations, such as circumventing the problem of inserting spherical particles into biological systems by simply using non-spherical particles already present within the system of interest. It also makes simulations involving non-spherical particles feasible, such as when using optical tweezers toolboxes. Some challenges yet to be solved that were not addressed here, are quantifying wall effects of non-spherical or non-cylindrical or flexible boundaries, or wall effects in viscoelastic fluids. Similarly, the hydrodynamic forces of complex fluids on non-spherical particles were not addressed, but still poses an interesting avenue of research.

Bibliography

[1] L. J. Gibson, S. Zhang, A. B. Stilgoe, T. A. Nieminen, and H. Rubinsztein-Dunlop. Active rotational and translational microrheology beyond the linear spring regime. *Physical Review E*, 95:042608, April 2017.

[2] S. Zhang, L. J. Gibson, A. B. Stilgoe, I. A. Favre-Bulle, T. A. Nieminen, and H. Rubinsztein-Dunlop. Ultrasensitive rotating photonic probes for complex biological systems. *Optica*, 4(9):1103–1108, September 2017.

[3] S. Zhang, L. J. Gibson, A. B. Stilgoe, T. A. Nieminen, and H. Rubinsztein-Dunlop. Impact of complex surfaces on biomicrorheological measurements using optical tweezers. *Lab on a Chip*, 18:315–322, January 2018.

[4] S. Zhang, L. J. Gibson, A. B. Stilgoe, T. A. Nieminen, and H. Rubinsztein-Dunlop. Measuring local properties inside a cell-mimicking structure using rotating optical tweezers. *Journal of Biophotonics*, 12(7):e201900022, February 2019.

[5] L. J. Gibson, S. Zhang, A. B. Stilgoe, T. A. Nieminen, and H. Rubinsztein-Dunlop. Machine learning wall effects of eccentric spheres for convenient computation. *Physical Review E*, 99:043304, April 2019.

[6] A. A. Bui, A. B. Stilgoe, I. C. Lenton, L. J. Gibson, A. V. Kashchuk, S. Zhang, H. Rubinsztein-Dunlop, and T. A. Nieminen. Theory and practice of simulation of optical tweezers. *Journal of Quantitative Spectroscopy and Radiative Transfer*, 195:66–75, July 2017.

[7] I. A. Favre-Bulle, S. Zhang, A. V. Kashchuk, I. C. D. Lenton, L. J. Gibson, A. B. Stilgoe, T. A. Nieminen, and H. Rubinsztein-Dunlop. Optical tweezers bring micromachines to biology. *Optics & Photonics News*, 29(4):40–47, April 2018.

[8] Nobel Media AB. Press release: The Nobel Prize in physics 2018. <https://www.nobelprize.org/prizes/physics/2018/press-release/>. Accessed 14 January 2019.

[9] A. Ashkin. Acceleration and trapping of particles by radiation pressure. *Physical Review Letters*, 24:156–159, January 1970.

[10] A. Ashkin and J. M. Dziedzic. Optical levitation by radiation pressure. *Applied Physics Letters*, 19(8):283–285, 1971.

[11] A. Ashkin, J. M. Dziedzic, J. E. Bjorkholm, and S. Chu. Observation of a single-beam gradient force optical trap for dielectric particles. *Optics Letters*, 11(5):288–290, May 1986.

[12] A. Ashkin, J. M. Dziedzic, and T. Yamane. Optical trapping and manipulation of single cells using infrared laser beams. *Nature*, 330(6150):769–771, December 1987.

[13] A. Bahadori, L. B. Oddershede, and P. M. Bendix. Hot-nanoparticle-mediated fusion of selected cells. *Nano Research*, 10(6):2034–2045, June 2017.

[14] A. Jonáš and P. Zemánek. Light at work: The use of optical forces for particle manipulation, sorting, and analysis. *ELECTROPHORESIS*, 29(24):4813–4851, 2008.

[15] K. Norregaard, R. Metzler, C. M. Ritter, K. Berg-Sørensen, and L. B. Oddershede. Manipulation and motion of organelles and single molecules in living cells. *Chemical Reviews*, 117(5):4342–4375, 2017. PMID: 28156096.

[16] D. Weihs, T. G. Mason, and M. A. Teitell. Bio-microrheology: A frontier in microrheology. *Biophysical Journal*, 91:4296–4305, 2006.

[17] D. Robert, T.-H. Nguyen, F. Gallet, and C. Wilhelm. In vivo determination of fluctuating forces during endosome trafficking using a combination of active and passive microrheology. *PLoS ONE*, 5(4):1–9, 04 2010.

[18] P. Kollmannsberger and B. Fabry. Linear and nonlinear rheology of living cells. *Annual Review of Materials Research*, 41(1):75–97, 2011.

[19] S. S. Rogers, T. A. Waigh, and J. R. Lu. Intracellular microrheology of motile amoeba proteus. *Biophysical Journal*, 94(8):3313–3322, 2008.

[20] Y.-Q. Chen, C.-Y. Kuo, M.-T. Wei, K. Wu, P.-T. Su, C.-S. Huang, and A. Chiou. Intracellular viscoelasticity of HeLa cells during cell division studied by video particle-tracking microrheology. *Journal of Biomedical Optics*, 19(1):011008, 2013.

[21] D. Wirtz. Particle-tracking microrheology of living cells: Principles and applications. *Annual Review of Biophysics*, 38(1):301–326, 2009. PMID: 19416071.

[22] J. Mas, A. C. Richardson, S. N. S. Reihani, L. B. Oddershede, and K. Berg-Sørensen. Quantitative determination of optical trapping strength and viscoelastic moduli inside living cells. *Physical Biology*, 10(4):046006, 2013.

[23] I. A. Favre-Bulle, A. B. Stilgoe, H. Rubinsztein-Dunlop, and E. K. Scott. Optical trapping of otoliths drives vestibular behaviours in larval zebrafish. *Nature Communications*, 8(1):630, 2017.

[24] J. Guck, R. Ananthakrishnan, H. Mahmood, T. J. Moon, C. C. Cunningham, and J. Käs. The optical stretcher: A novel laser tool to micromanipulate cells. *Biophysical journal*, 81(2):767–784, August 2001.

[25] M. P. MacDonald, G. C. Spalding, and K. Dholakia. Microfluidic sorting in an optical lattice. *Nature*, 426(6965):421–424, November 2003.

[26] J. Leach, H. Mushfique, R. di Leonardo, M. Padgett, and J. Cooper. An optically driven pump for microfluidics. *Lab on a Chip*, 6:735–739, 2006.

[27] H. Mushfique, J. Leach, H. Yin, R. D. Leonardo, M. J. Padgett, and J. M. Cooper. 3D mapping of microfluidic flow in laboratory-on-a-chip structures using optical tweezers. *Analytical Chemistry*, 80(11):4237–4240, June 2008.

[28] M. Tassieri. *Microrheology with Optical Tweezers : Principles and Applications.* Pan Stanford, 2016.

[29] T. G. Mason and D. A. Weitz. Optical measurements of frequency-dependent linear viscoelastic moduli of complex fluids. *Physical Review Letters*, 74:1250–1253, February 1995.

[30] A. I. Bishop, T. A. Nieminen, N. R. Heckenberg, and H. Rubinsztein-Dunlop. Optical microrheology using rotating laser-trapped particles. *Physical Review Letters*, 92:198104, 2004.

[31] M. Atakhorrami, J. I. Sulkowska, K. M. Addas, G. H. Koenderink, J. X. Tang, A. J. Levine, F. C. MacKintosh, and C. F. Schmidt. Correlated fluctuations of microparticles in viscoelastic solutions: Quantitative measurement of material properties by microrheology in the presence of optical traps. *Physical Review E*, 73:061501, June 2006.

[32] A. Meyer, A. Marshall, B. G. Bush, and E. M. Furst. Laser tweezer microrheology of a colloidal suspension. *Journal of Rheology*, 50(1):77–92, 2006.

[33] R. R. Brau, J. M. Ferrer, H. Lee, C. E. Castro, B. K. Tam, P. B. Tarsa, P. Matsudaira, M. C. Boyce, R. D. Kamm, and M. J. Lang. Passive and active microrheology with optical tweezers. *Journal of Optics A: Pure and Applied Optics*, 9(8):S103, 2007.

[34] B. Lincoln, F. Wottawah, S. Schinkinger, S. Ebert, and J. Guck. High-throughput rheological measurements with an optical stretcher. *Methods in Cell Biology*, 83:397–423, 2007.

[35] A. Yao, M. Tassieri, M. Padgett, and J. Cooper. Microrheology with optical tweezers. *Lab on a Chip*, 9:2568–2575, 2009.

[36] G. Pesce, A. C. De Luca, G. Rusciano, P. A. Netti, S. Fusco, and A. Sasso. Microrheology of complex fluids using optical tweezers: a comparison with macrorheological measurements. *Journal of Optics A: Pure and Applied Optics*, 11(3):034016, 2009.

[37] M. Tassieri, G. M. Gibson, R. M. L. Evans, A. M. Yao, R. Warren, M. J. Padgett, and J. M. Cooper. Measuring storage and loss moduli using optical tweezers: Broadband microrheology. *Physical Review E*, 81:026308, February 2010.

[38] D. Preece, R. Warren, R. M. L. Evans, G. M. Gibson, M. J. Padgett, J. M. Cooper, and M. Tassieri. Optical tweezers: wideband microrheology. *Journal of Optics*, 13(4):044022, 2011.

[39] M. Tassieri, R. M. L. Evans, R. L. Warren, N. J. Bailey, and J. M. Cooper. Microrheology with optical tweezers: data analysis. *New Journal of Physics*, 14(11):115032, November 2012.

[40] J. S. Bennett, L. J. Gibson, R. M. Kelly, E. Brousse, B. Baudisch, D. Preece, T. A. Nieminen, T. Nicholson, N. R. Heckenberg, and H. Rubinsztein-Dunlop. Spatially-resolved rotational microrheology with an optically-trapped sphere. *Scientific Reports*, 3:1759, 2013.

[41] I. C. D. Lenton, A. B. Stilgoe, H. Rubinsztein-Dunlop, and T. A. Nieminen. Visual guide to optical tweezers. *European Journal of Physics*, 38(3):034009, March 2017.

[42] S. Parkin, G. Knöner, W. Singer, T. A. Nieminen, N. R. Heckenberg, and H. Rubinsztein-Dunlop. Optical torque on microscopic objects. In L. Wilson and P. Matsudaira, editors, *Laser Manipulation of Cells and Tissues*, volume 82 of *Methods in Cell Biology*, pages 525–561. Academic Press, 2007.

[43] J. P. Torres and L. Torner, editors. *Twisted Photons: Applications of Light with Orbital Angular Momentum*. Wiley-VCH Verlag, Weinheim, 2011.

[44] D. L. Andrews, editor. *Structured light and its applications: an introduction to phase-structured beams and nanoscale optical forces*. Academic Press, Amsterdam; Boston, 2008.

[45] D. B. Phillips, G. M. Gibson, R. Bowman, M. J. Padgett, S. Hanna, D. M. Carberry, M. J. Miles, and S. H. Simpson. An optically actuated surface scanning probe. *Opt. Express*, 20(28):29679–29693, December 2012.

[46] L. Kelemen, S. Valkai, and P. Ormos. Integrated optical motor. *Appl. Opt.*, 45(12):2777–2780, April 2006.

[47] T. A. Nieminen, N. R. Heckenberg, and H. Rubinsztein-Dunlop. Optical measurement of microscopic torques. *Journal of Modern Optics*, 48:405–413, March 2001.

[48] A. I. Bishop, T. A. Nieminen, N. R. Heckenberg, and H. Rubinsztein-Dunlop. Optical application and measurement of torque on microparticles of isotropic nonabsorbing material. *Physical Review A*, 68:033802, September 2003.

[49] M. W. Berns, W. H. Wright, B. J. Tromberg, G. A. Profeta, J. J. Andrews, and R. J. Walter. Use of a laser-induced optical force trap to study chromosome movement on the mitotic spindle. *Proceedings of the National Academy of Sciences of the United States of America*, 86(12):4539–4543, 1989.

[50] J. Guck, R. Ananthakrishnan, T. J. Moon, C. C. Cunningham, and J. Käs. Optical deformability of soft biological dielectrics. *Physical Review Letters*, 84:5451–5454, June 2000.

[51] A. Y. Malkin and A. I. Isayev. *Rheology: Concepts, Methods, and Applications*. ChemTec Publishing, third edition, 2017.

[52] M. Tassieri. Linear microrheology with optical tweezers of living cells 'is not an option'! *Soft Matter*, 11:5792–5798, 2015.

[53] F. Jünger, F. Kohler, A. Meinel, T. Meyer, R. Nitschke, B. Erhard, and A. Rohrbach. Measuring local viscosities near plasma membranes of living cells with photonic force microscopy. *Biophysical Journal*, 109(5):869–882, 2015.

[54] F. Irgens. *Continuum Mechanics*. Springer Berlin Heidelberg, Berlin, Heidelberg, 2008.

[55] H. Brenner. The Stokes resistance of an arbitrary particle. *Chemical Engineering Science*, 18(1):1–25, 1963.

[56] H. Brenner. The Stokes resistance of an arbitrary particle—II: An extension. *Chemical Engineering Science*, 19(9):599–629, 1964.

[57] H. Brenner. The Stokes resistance of an arbitrary particle—III: Shear fields. *Chemical Engineering Science*, 19(9):631–651, 1964.

[58] H. Brenner. The Stokes resistance of an arbitrary particle—IV: Arbitrary fields of flow. *Chemical Engineering Science*, 19(10):703–727, 1964.

[59] H. Brenner. The Stokes resistance of an arbitrary particle—Part V: Symbolic operator representation of intrinsic resistance. *Chemical Engineering Science*, 21(1):97–109, 1966.

[60] J. Happel and H. Brenner. *Low Reynolds number hydrodynamics with special applications to particulate media*. Mechanics of fluids and transport processes, 1. Springer Netherlands, Dordrecht, 1983.

[61] M. Chaoui and F. Feuillebois. Creeping flow around a sphere in a shear flow close to a wall. *The Quarterly Journal of Mechanics and Applied Mathematics*, 56:381–410, 2003.

[62] G. B. Jeffery. On the steady rotation of a solid of revolution in a viscous fluid. *Proceedings of the London Mathematical Society*, 2(14):327–338, 1915.

[63] W. R. Dean and M. E. O'Neill. A slow motion of viscous liquid caused by the rotation of a solid sphere. *Mathematika*, 10(1):13–24, 1963.

[64] J. Leach, H. Mushfique, S. Keen, R. Di Leonardo, G. Ruocco, J. M. Cooper, and M. J. Padgett. Comparison of Faxén's correction for a microsphere translating or rotating near a surface. *Physical Review E*, 79:026301, February 2009.

[65] J. Bławzdziewicz, V. Cristini, and M. Loewenberg. Stokes flow in the presence of a planar interface covered with incompressible surfactant. *Physics of Fluids*, 11(2):251–258, 1999.

[66] D. Lopez and E. Lauga. Dynamics of swimming bacteria at complex interfaces. *Physics of Fluids*, 26(7):071902, 2014.

[67] H. Lamb. *Hydrodynamics*. Dover Publications, 6th edition, 1945.

[68] O. S. Pak and E. Lauga. Generalized squirming motion of a sphere. *Journal of Engineering Mathematics*, 88(1):1–28, October 2014.

[69] P. Morse and H. Feshbach. *Methods of Theoretical Physics*. Number 1 in International series in pure and applied physics. McGraw-Hill, 1953.

[70] P. Moon and D. E. Spencer. *Field Theory Handbook*. Springer-Verlag, Berlin, 1961.

[71] T. Nieminen, H. Rubinsztein-Dunlop, and N. Heckenberg. Calculation of the T-matrix: general considerations and application of the point-matching method. *Journal of Quantitative Spectroscopy and Radiative Transfer*, 79–80:1019–1029, 2003.

[72] Y. Tseng and D. Wirtz. Mechanics and multiple-particle tracking microheterogeneity of α-actinin-cross-linked actin filament networks. *Biophysical Journal*, 81(3):1643–1656, 2001.

[73] A. Palmer, T. G. Mason, J. Xu, S. C. Kuo, and D. Wirtz. Diffusing wave spectroscopy microrheology of actin filament networks. *Biophysical journal*, 76(2):1063–71, February 1999.

[74] B. R. Dasgupta, S.-Y. Tee, J. C. Crocker, B. J. Frisken, and D. A. Weitz. Microrheology of polyethylene oxide using diffusing wave spectroscopy and single scattering. *Physical Review E*, 65:051505, May 2002.

[75] Y. Tseng, K. M. An, and D. Wirtz. Microheterogeneity controls the rate of gelation of actin filament networks. *Journal of Biological Chemistry*, 277(20):18143–18150, 2002.

[76] H. Lamb. *Hydrodynamics*. University Press, 1895.

[77] P. E. King-Smith, B. A. Fink, R. M. Hill, K. W. Koelling, and J. M. Tiffany. The thickness of the tear film. *Current Eye Research*, 29(4-5):357–368, 2004.

[78] J. Wang, D. Fonn, T. L. Simpson, and L. Jones. Precorneal and pre- and postlens tear film thickness measured indirectly with optical coherence tomography. *IOVS*, 44:2524–2528, 2003.

[79] R. Di Leonardo, S. Keen, F. Ianni, J. Leach, M. J. Padgett, and G. Ruocco. Hydrodynamic interactions in two dimensions. *Physical Review E*, 78:031406, September 2008.

[80] R. Nosrati, A. Driouchi, C. M. Yip, and D. Sinton. Two-dimensional slither swimming of sperm within a micrometre of a surface. *Nature Communications*, 6:8703, November 2015.

[81] D. Papavassiliou and G. P. Alexander. Exact solutions for hydrodynamic interactions of two squirming spheres. *Journal of Fluid Mechanics*, 813:618–646, 2017.

[82] M. Guo, A. J. Ehrlicher, M. H. Jensen, M. Renz, J. R. Moore, R. D. Goldman, J. Lippincott-Schwartz, F. C. Mackintosh, and D. A. Weitz. Probing the stochastic, motor-driven properties of the cytoplasm using force spectrum microscopy. *Cell*, 158(4):822–832, 2014.

[83] B. Lin, J. Yu, and S. A. Rice. Direct measurements of constrained brownian motion of an isolated sphere between two walls. *Physical Review E*, 62:3909–3919, September 2000.

[84] H. B. Eral, J. M. Oh, D. van den Ende, F. Mugele, and M. H. G. Duits. Anisotropic and hindered diffusion of colloidal particles in a closed cylinder. *Langmuir*, 26(22):16722–16729, 2010.

[85] S. L. Dettmer, S. Pagliara, K. Misiunas, and U. F. Keyser. Anisotropic diffusion of spherical particles in closely confining microchannels. *Physical Review E*, 89:062305, June 2014.

[86] G. B. Jeffery. On a form of the solution of Laplace's equation suitable for problems relating to two spheres. *Proceedings of the Royal Society of London. Series A, Containing Papers of a Mathematical and Physical Character*, 87(593):109–120, 1912.

[87] M. Stimson and G. B. Jeffery. The motion of two spheres in a viscous fluid. *Proceedings of the Royal Society of London. Series A, Containing Papers of a Mathematical and Physical Character*, 111(757):110–116, 1926.

[88] S. R. Majumdar. On the slow motion of viscous liquid in space between two eccentric spheres. *Journal of the Physical Society of Japan*, 26(3):827–840, 1969.

[89] M. E. O'Neill and R. Majumdar. Asymmetrical slow viscous fluid motions caused by the translation or rotation of two spheres. Part I: The determination of exact solutions for any values of the ratio of radii and separation parameters. *Zeitschrift für angewandte Mathematik und Physik ZAMP*, 21(2):164–179, March 1970.

[90] M. E. O'Neill and S. R. Majumdar. Asymmetrical slow viscous fluid motions caused by the translation or rotation of two spheres. Part II: Asymptotic forms of the solutions when the minimum clearance between the spheres approaches zero. *Zeitschrift für angewandte Mathematik und Physik ZAMP*, 21(2):180–187, March 1970.

[91] R. G. Cox and H. Brenner. The slow motion of a sphere through a viscous fluid towards a plane surface—ii small gap widths, including inertial effects. *Chemical Engineering Science*, 22(12):1753–1777, 1967.

[92] M. E. O'Neill and B. S. Bhatt. Slow motion of a solid sphere in the presence of a naturally permeable surface. *The Quarterly Journal of Mechanics and Applied Mathematics*, 44(1):91–104, 1991.

[93] G. Cybenko. Approximation by superpositions of a sigmoidal function. *Mathematics of Control, Signals and Systems*, 2(4):303–314, December 1989.

[94] C. Veigel and C. F. Schmidt. Moving into the cell: single-molecule studies of molecular motors in complex environments. *Nature Reviews Molecular Cell Biology*, 12:163–167, February 2011. Review Article.

[95] D. Needleman and Z. Dogic. Active matter at the interface between materials science and cell biology. *Nature Reviews Materials*, 2:17048, July 2017.

[96] A. Yamada, M. Le Berre, K. Yoshikawa, and D. Baigl. Spontaneous generation of giant liposomes from an oil/water interface. *ChemBioChem*, 8(18):2215–2218, 2007.

[97] P. Minzioni, R. Osellame, C. Sada, S. Zhao, F. G. Omenetto, K. B. Gylfason, T. Haraldsson, Y. Zhang, A. Ozcan, A. Wax, F. Mugele, H. Schmidt, G. Testa, R. Bernini, J. Guck, C. Liberale, K. Berg-Sørensen, J. Chen, M. Pollnau, S. Xiong, A.-Q. Liu, C.-C. Shiue, S.-K. Fan, D. Erickson, and D. Sinton. Roadmap for optofluidics. *Journal of Optics*, 19(9):093003, August 2017.

[98] K. C. Neuman and A. Nagy. Single-molecule force spectroscopy: optical tweezers, magnetic tweezers and atomic force microscopy. *Nature Methods*, 5(6):491–505, 2008.

[99] N. J. Hoh and R. N. Zia. The impact of probe size on measurements of diffusion in active microrheology. *Lab on a Chip*, 16:3114–3129, 2016.

[100] M. P. Lee, G. M. Gibson, D. Phillips, M. J. Padgett, and M. Tassieri. Dynamic stereo microscopy for studying particle sedimentation. *Optics Express*, 22(4):4671–4677, February 2014.

[101] B. Cui, H. Diamant, and B. Lin. Screened hydrodynamic interaction in a narrow channel. *Physical Review Letters*, 89:188302, October 2002.

[102] R. L. Truby and J. A. Lewis. Printing soft matter in three dimensions. *Nature*, 540:371–378, 2016.

[103] S. Waheed, J. M. Cabot, N. P. Macdonald, T. Lewis, R. M. Guijt, B. Paull, and M. C. Breadmore. 3D printed microfluidic devices: enablers and barriers. *Lab on a Chip*, 16:1993–2013, 2016.

[104] H. Brenner and R. M. Sonshine. Slow viscous rotation of a sphere in a circular cylinder. *The Quarterly Journal of Mechanics and Applied Mathematics*, 17:55–63, 1964.

[105] L. D. Landau and E. M. Lifshitz. *Fluid Mechanics*, volume 6. Pergamon Press, 2nd edition, 1987.

Appendix A

Stress Tensors and Stokes Equations

For reference, this appendix lists stress tensors and equations of fluid motion in Cartesian, cylindrical and spherical coordinates as outlined by Landau and Lifshitz [105].

A.1 Stress Tensor

The symmetric stress tensor in a Newtonian incompressible viscous fluid is

$$\sigma = -p\mathbf{I} + \eta\left(\nabla\mathbf{v} + \nabla\mathbf{v}^T\right), \tag{A.1}$$

where p is the pressure, η is the dynamic viscosity, $\mathbf{I}$ is the identity tensor and the T superscript denotes transposition.

Stress Tensor in Cartesian Coordinates (x, y, z)

$$\sigma_{xx} = -p + 2\eta\frac{\partial v_x}{\partial x} \qquad \sigma_{xy} = \eta\left(\frac{\partial v_x}{\partial y} + \frac{\partial v_y}{\partial x}\right) \tag{A.2}$$

$$\sigma_{yy} = -p + 2\eta\frac{\partial v_y}{\partial y} \qquad \sigma_{yz} = \eta\left(\frac{\partial v_y}{\partial z} + \frac{\partial v_z}{\partial y}\right) \tag{A.3}$$

$$\sigma_{zz} = -p + 2\eta\frac{\partial v_z}{\partial z} \qquad \sigma_{zx} = \eta\left(\frac{\partial v_z}{\partial x} + \frac{\partial v_x}{\partial z}\right) \tag{A.4}$$

Stress Tensor in Cylindrical Coordinates (r, θ, z)

$$\sigma_{rr} = -p + 2\eta\frac{\partial v_r}{\partial r} \qquad \sigma_{r\theta} = \eta\left(\frac{1}{r}\frac{\partial v_r}{\partial \theta} + \frac{\partial v_\theta}{\partial r} - \frac{v_\theta}{r}\right) \tag{A.5}$$

$$\sigma_{\theta\theta} = -p + 2\eta\left(\frac{1}{r}\frac{\partial v_\theta}{\partial \theta} + \frac{v_\theta}{r}\right) \qquad \sigma_{\theta z} = \eta\left(\frac{\partial v_\theta}{\partial z} + \frac{1}{r}\frac{\partial v_z}{\partial \theta}\right) \tag{A.6}$$

$$\sigma_{zz} = -p + 2\eta\frac{\partial v_z}{\partial z} \qquad \sigma_{zr} = \eta\left(\frac{\partial v_r}{\partial z} + \frac{\partial v_z}{\partial r}\right) \tag{A.7}$$

Stress Tensor in Spherical Coordinates (r,θ,ϕ)

$$\sigma_{rr} = -p + 2\eta\frac{\partial v_r}{\partial r} \qquad \sigma_{r\theta} = \eta\left(\frac{1}{r}\frac{\partial v_r}{\partial \theta} + \frac{\partial v_\theta}{\partial r} - \frac{v_\theta}{r}\right) \tag{A.8}$$

$$\sigma_{\theta\theta} = -p + 2\eta\left(\frac{1}{r}\frac{\partial v_\theta}{\partial \theta} + \frac{v_r}{r}\right) \qquad \sigma_{\theta\phi} = \eta\left(\frac{1}{r\sin\theta}\frac{\partial v_\theta}{\partial \phi} + \frac{1}{r}\frac{\partial v_\phi}{\partial \theta} - \frac{v_\phi\cot\theta}{r}\right) \tag{A.9}$$

$$\sigma_{\phi\phi} = -p + 2\eta\left(\frac{1}{r\sin\theta}\frac{\partial v_\phi}{\partial \phi} + \frac{v_r}{r} + \frac{v_\theta\cot\theta}{r}\right) \qquad \sigma_{\phi r} = \eta\left(\frac{\partial v_\phi}{\partial r} + \frac{1}{r\sin\theta}\frac{\partial v_r}{\partial \phi} - \frac{v_\phi}{r}\right) \tag{A.10}$$

A.2 Equations of Motion

The equations of motion of a Newtonian incompressible viscous fluid undergoing low Reynolds number flow are

$$\nabla^2\mathbf{v} = \frac{1}{\eta}\nabla p, \qquad \nabla\cdot\mathbf{v} = 0, \tag{A.11}$$

where $\mathbf{v}$ is the fluid velocity, p is the pressure and η is the dynamic viscosity.

Equations of Motion in Cartesian Coordinates (x,y,z)

$$\nabla^2 v_x = \frac{1}{\eta}\frac{\partial p}{\partial x} \qquad \nabla^2 v_y = \frac{1}{\eta}\frac{\partial p}{\partial y} \qquad \nabla^2 v_z = \frac{1}{\eta}\frac{\partial p}{\partial z} \tag{A.12}$$

$$\nabla^2 = \frac{\partial^2}{\partial x^2} + \frac{\partial^2}{\partial y^2} + \frac{\partial^2}{\partial z^2} \qquad \frac{\partial v_x}{\partial x} + \frac{\partial v_y}{\partial y} + \frac{\partial v_z}{\partial z} = 0 \tag{A.13}$$

Equations of Motion in Cylindrical Coordinates (r,θ,z)

$$\nabla^2 v_r - \frac{2}{r^2}\frac{\partial v_\theta}{\partial \theta} - \frac{v_r}{r^2} = \frac{1}{\eta}\frac{\partial p}{\partial r} \qquad \nabla^2 v_\theta + \frac{2}{r^2}\frac{\partial v_r}{\partial \theta} - \frac{v_\theta}{r^2} = \frac{1}{\eta r}\frac{\partial p}{\partial \theta} \qquad \nabla^2 v_z = \frac{1}{\eta}\frac{\partial p}{\partial z} \tag{A.14}$$

$$\nabla^2 = \frac{\partial^2}{\partial r^2} + \frac{1}{r}\frac{\partial}{\partial r} + \frac{1}{r^2}\frac{\partial^2}{\partial \theta^2} + \frac{\partial^2}{\partial z^2} \qquad \frac{\partial v_r}{\partial r} + \frac{v_r}{r} + \frac{1}{r}\frac{\partial v_\theta}{\partial \theta} + \frac{\partial v_z}{\partial z} = 0 \tag{A.15}$$

Equations of Motion in Spherical Coordinates (r,θ,ϕ)

$$\nabla^2 v_r - \frac{2}{r^2\sin^2\theta}\frac{\partial(v_\theta\sin\theta)}{\partial\theta} - \frac{2}{r^2\sin\theta}\frac{\partial v_\phi}{\partial\phi} - \frac{2v_r}{r^2} = \frac{1}{\eta}\frac{\partial p}{\partial r} \tag{A.16}$$

$$\nabla^2 v_\theta - \frac{2\cos\theta}{r^2\sin^2\theta}\frac{\partial v_\phi}{\partial\phi} + \frac{2}{r^2}\frac{\partial v_r}{\partial\theta} - \frac{v_\theta}{r^2\sin^2\theta} = \frac{1}{\eta r}\frac{\partial p}{\partial\theta} \tag{A.17}$$

$$\nabla^2 v_\phi + \frac{2}{r^2\sin\theta}\frac{\partial v_r}{\partial\phi} + \frac{2\cos\theta}{r^2\sin^2\theta}\frac{\partial v_\theta}{\partial\phi} - \frac{v_\phi}{r^2\sin^2\theta} = \frac{1}{\eta r\sin\theta}\frac{\partial p}{\partial\phi} \tag{A.18}$$

$$\nabla^2 = \frac{1}{r^2}\frac{\partial}{\partial r}\left(r^2\frac{\partial}{\partial r}\right) + \frac{1}{r^2\sin\theta}\frac{\partial}{\partial\theta}\left(\sin\theta\frac{\partial}{\partial\theta}\right) + \frac{1}{r^2\sin^2\theta}\frac{\partial^2}{\partial\phi^2} \tag{A.19}$$

$$\frac{1}{r^2}\frac{\partial(r^2 v_r)}{\partial r} + \frac{1}{r\sin\theta}\frac{\partial(v_\theta\sin\theta)}{\partial\theta} + \frac{1}{r\sin\theta}\frac{\partial v_\phi}{\partial\phi} = 0 \tag{A.20}$$

Appendix B

Tables

B.1 Chapter 3 List of Variable Transformations

Table B.1: List of Variable Transformations.

$T(\phi)$, where $\beta > 0$	$\Psi(\phi)$	Optimal ϕ_0
$\frac{1}{\beta}\sin\beta\phi$	$\frac{2}{\beta}\tan\left(\frac{\beta}{2}\phi\right)$	$\frac{\pi}{2\beta} \leq \phi < \frac{\pi}{\beta}$
$\frac{1}{\beta}\tan\beta\phi$	$\frac{1}{\beta}\sin\beta\phi$	$\phi_0 = \frac{\pi}{2\beta}$
$\frac{1}{\beta}\sinh\beta\phi$	$\frac{2}{\beta}\tanh\left(\frac{\beta}{2}\phi\right)$	$\phi_0 \gg 0$
$\frac{1}{\beta}\tanh\beta\phi$	$\frac{1}{\beta}\sinh(\beta\phi)$	$\phi_0 \gg 0$
$\phi + \beta\phi^3$	$\frac{\phi}{\sqrt{1+\beta\phi^2}}$	$\phi_0 \gg 0$
$\phi - \beta\phi^3$	$\frac{\phi}{\sqrt{1-\beta\phi^2}}$	$\frac{1}{\sqrt{3\beta}} \leq \phi < \frac{1}{\sqrt{\beta}}$
$\frac{\phi+\beta\phi^3}{1+3\beta\phi^2}$	$\phi + \beta\phi^3$	$\phi_0 \gg 0$
$\frac{\phi-\beta\phi^3}{1-3\beta\phi^2}$	$\phi - \beta\phi^3$	$\phi_0 = \frac{1}{\sqrt{3\beta}}$
$\phi e^{-\beta\phi^2}$	$\frac{\text{sign}(\phi)}{\sqrt{\beta}}\exp\left[\frac{1}{2}\left(\text{Ei}\left(\beta\phi^2\right) - \gamma\right)\right]$	$\phi \geq \frac{1}{\sqrt{2\beta}}$
$\frac{\phi}{1-2\beta\phi^2}$	$\phi e^{-\beta\phi^2}$	$\phi = \frac{1}{\sqrt{2\beta}}$
$\text{Ei}(z)$ is the exponential integral function and $\gamma \approx 0.5772$ is Euler's constant.		

B.2 Chapter 4 Network Biases and Weights

$B1$	$W1$		$W2^T$				
4.8113394	-2.9231488	-0.19127825	-6.3213834	-18.123169	-12.355483	32.938574	-1.9663136
4.5643461	-10.860592	-9.8976544	-19.759477	-10.955627	-15.427646	19.596163	-6.892128
-4.5063286	2.5794291	-0.57787839	-1.6816723	-5.2511235	-3.2960726	8.1682192	-0.56582731
5.211532	-0.89619242	3.3242802	-0.12901484	-0.58020697	-0.33093263	0.41179354	-0.065380236
2.6380771	-3.3084402	-4.3683345	-4.8869387	0.68458723	-0.082493243	-1.8959001	-0.79845435
12.991963	-11.787911	-24.2786	14.790883	-4.810932	-0.11552022	4.1409808	1.0302539
10.440263	-21.973296	-30.476054	14.07486	-6.5362532	-0.206136	-0.59875748	0.80570816
-1.9661939	-0.93824277	-0.74110631	1.8272341	-15.152262	-4.4719601	16.482887	11.625042
1.6562525	-0.508093	1.0002596	-2.7220653	-2.7714042	-2.9031277	10.906282	-0.87789713
1.5871351	-0.59273394	0.8478989	3.630631	3.2871044	2.5964378	-13.685592	1.0218652
-18.154178	-5.5214697	10.740687	0.40812945	-17.993253	0.042159326	9.2202538	-7.3656119
-101.1157	-87.529199	12.362803	-3.5990025	-2.83695	0.050704842	4.1705861	2.2782291
0.1394124	-1.4397034	0.18357732	-0.79059739	-1.1726016	1.682904	-5.5206363	0.11718537
-0.34850942	-0.62701717	-0.58818834	-0.95215953	0.66840542	-1.8153526	4.9081699	-0.63673305
4.1411886	-10.308195	-9.1576609	7.1192099	3.3686357	6.4683209	-15.307482	2.4936587
-0.079175964	1.2190827	0.083425231	4.999372	4.0872406	0.94409221	-2.6496287	0.22328977
0.11709931	0.46571726	-0.34610801	-4.5114092	0.29811614	3.1590265	12.937801	-1.3904952
3.1701055	-0.23574607	-3.4757205	0.73913844	-0.39776158	0.022167735	0.28666821	0.035013077
-12.493281	13.457111	24.860202	45.88042	-14.284513	-0.3590089	12.601054	3.5595016
0.13945188	-1.5153369	0.13135781	1.3255305	1.3980774	-1.1914806	3.7415379	-0.091354023
-5.509932	5.1259729	9.4554294	12.578025	-2.4511914	-0.18342767	4.6062157	1.712977
0.2407358	-1.2733534	-0.058980096	3.9380972	3.7897635	0.66840072	-0.51027143	0.077155285
1.6609392	0.36350978	-1.3092586	1.12103	-0.63803385	0.36837789	1.1595936	0.29330014
-1.8788659	-1.9290912	0.41248143	0.69266209	0.30858376	-0.11972862	-1.0364245	-0.3576897
-0.38260522	-0.14451115	0.18892011	-9.1871081	-7.8246746	24.299862	16.922558	3.0753937
-4.2833535	9.6026275	11.297067	-2.5293361	2.0056763	0.15567844	4.5601494	-0.42652554
-3.3792586	-2.4819184	0.48181726	9.3875976	6.5688575	-0.041558872	-12.566227	-5.9786109
6.7632512	-2.9390105	-8.3092822	29.295549	-8.6337375	-0.26950606	9.5683882	2.9499413
-3.3592869	-2.0614463	0.3742545	-26.594558	-19.56772	-0.72779693	34.762897	18.847575
0.35806924	-1.7091651	-1.1349919	-0.1240636	-0.10956647	-0.14858281	0.41901725	-0.091429445
-2.5564898	-1.4286332	1.3590837	-0.21646259	-0.49888707	0.014728244	0.55719107	-0.10686906
2.4520402	-2.4781979	-2.801879	0.59375222	-1.28546	0.93238021	-6.480926	-1.2092875
20.383505	19.792641	0.5185137	3.8065898	3.8804101	0.083159283	-5.8080313	-4.6632913
0.16392206	0.05736511	-0.49034398	2.4749204	-2.8603028	8.9343512	-11.453807	3.3752432
20.773334	20.332416	0.30276654	3.3112701	3.3967786	0.1242549	-5.1968768	-3.9310157
-7.175313	-6.8201546	-0.62906033	2.0843824	-5.2005432	-2.7183036	-1.2745542	1.1503635
20.862433	19.184505	-1.5202991	-3.1956922	-2.480192	0.010624945	3.7007527	2.4594603
7.0845249	4.7165266	0.43219732	-4.2952773	-7.5974342	-2.0037384	3.1573676	8.7907618
-64.328546	-63.523828	0.78741103	-15.494941	-12.659212	-0.8366425	19.738609	13.672629
6.4134444	1.8267049	-2.8176156	4.91351	20.662964	-0.37330178	-10.477384	9.327477
65.93701	65.223835	-0.90004386	-3.6397098	-2.9529805	-0.18886984	4.5887706	3.207476
40.204736	34.813309	-5.4050049	0.29920049	0.21557488	-0.0010200251	-0.32442703	-0.17976199
20.600209	20.081596	0.41455639	-7.0566527	-7.2266401	-0.20823667	10.978269	8.5102877
-20.482695	-18.717276	1.6166552	-3.3415423	-2.57432	0.015813208	3.8363283	2.520433
123.3774	122.07677	-1.52729	-9.3685206	-7.4665641	-0.63593297	11.553057	8.1066735
-1.9329479	-0.95373	-0.70341813	-2.3953775	16.121793	4.464689	-14.534989	-12.312116
-120.01857	-118.69376	1.4582815	-14.384763	-11.541028	-0.93543663	17.901586	12.503635
65.216127	63.648383	-0.75097661	-52.091821	-42.607982	-2.8920707	66.532393	45.908741
195.54734	191.51908	-2.1452241	33.022971	27.52403	1.5653954	-43.14771	-29.453425
7.1837566	6.8299258	0.63479725	2.1302686	-5.0604977	-2.6742399	-1.2721418	1.0067911

Table B.2: Network biases and weights given to 8 significant figures. B2=[-5.6955277, -19.715168, 25.929231, 40.363108, -3.5442271]^T.